

Dynamics and Steady-states of Thin Film Droplets on Homogeneous and Heterogeneous Substrates

by

Weifan Liu

Department of Mathematics
Duke University

Date: _____

Approved:

Thomas P. Witelski, Supervisor

Alexander A. Kiselev

Jianfeng Lu

James H. Nolen

Dissertation submitted in partial fulfillment of the requirements for the degree of
Doctor of Philosophy in the Department of Mathematics
in the Graduate School of Duke University
2019

ABSTRACT

Dynamics and Steady-states of Thin Film Droplets on Homogeneous and Heterogeneous Substrates

by

Weifan Liu

Department of Mathematics
Duke University

Date: _____

Approved:

Thomas P. Witelski, Supervisor

Alexander A. Kiselev

Jianfeng Lu

James H. Nolen

An abstract of a dissertation submitted in partial fulfillment of the requirements for
the degree of Doctor of Philosophy in the Department of Mathematics
in the Graduate School of Duke University
2019

Copyright © 2019 by Weifan Liu
All rights reserved except the rights granted by the
Creative Commons Attribution-Noncommercial Licence

Abstract

In this dissertation, we study the dynamics and steady-states of thin liquid films on solid substrates using lubrication equations. Steady-states and bifurcation of thin films on chemically patterned substrates have been previously studied for thin films on infinite domains with periodic boundary conditions. Inspired by previous work, we study the steady-state thin film on a chemically heterogeneous 1-D domain of finite length, subject to no-flux boundary conditions. Based on the structure of the bifurcation diagram, we classify the 1-D steady-state solutions that could exist on such substrates into six different branches and develop asymptotic approximation of steady-states on each branch. We show that using perturbation expansions, the leading order solutions provide a good prediction of steady-state thin film on a stepwise-patterned substrate. We also show that all of the analysis in 1-D can be easily extended to axisymmetric solutions in 2-D, which leads to qualitatively the same results.

Subject to long-wave instability, thin films break up and form droplets. In presence of small fluxes, these droplets move and exchange mass. In 2002, Glasner and Witelski proposed a simplified model that predicts the pressure and position evolution of droplets in 1-D on homogeneous substrates when fluxes are small. While the model is capable of giving accurate prediction of the dynamics of droplets in presence of small fluxes, the model becomes less accurate as fluxes increase. We present a refined model that computes the pressure and position of a single droplet

on a finite domain. Through numerical simulations, we show that the refined model captures single-droplet dynamics with higher accuracy than the previous model.

Contents

| | |
|---|-------------|
| Abstract | iv |
| List of Figures | ix |
| Acknowledgements | xiii |
| 1 Introduction | 1 |
| 1.1 Thin films on homogeneous substrates | 2 |
| 1.2 Thin films on heterogeneous substrates | 4 |
| 1.3 Plan of the dissertation | 7 |
| 2 Lubrication equation | 9 |
| 2.1 Derivation | 9 |
| 2.2 Disjoining pressure | 13 |
| 2.3 Summary | 14 |
| 3 Steady-states and bifurcations | 16 |
| 3.1 Steady-state solutions in 1-D | 18 |
| 3.1.1 Large homoclinic droplets | 20 |
| 3.1.2 Small homoclinic droplets | 24 |
| 3.2 Steady-state axisymmetric solutions | 28 |
| 3.3 Stability and bifurcation | 32 |
| 3.3.1 Bifurcation of 1-D solutions | 32 |
| 3.3.2 Bifurcation of axisymmetric solutions | 42 |

| | | |
|----------|--|------------|
| 3.4 | Summary | 53 |
| 4 | Thin films on heterogeneous substrates | 56 |
| 4.1 | Introduction of chemical heterogeneity into substrates | 58 |
| 4.2 | Classification of branches of bifurcation diagram in 1-D | 64 |
| 4.2.1 | Small-thickness films | 66 |
| 4.2.2 | Large-thickness films | 74 |
| 4.2.3 | Small-width droplets | 79 |
| 4.2.4 | Pinned droplets | 89 |
| 4.2.5 | Large-width droplets | 96 |
| 4.2.6 | Large confined droplets | 103 |
| 4.3 | Stability of steady-state solutions | 109 |
| 4.4 | Leak and spillover in the limit of large A_2 | 114 |
| 4.5 | Axisymmetric solution | 119 |
| 4.5.1 | Small-thickness films | 120 |
| 4.5.2 | Large-thickness films | 122 |
| 4.5.3 | Small-radii droplets | 125 |
| 4.5.4 | Pinned droplets | 127 |
| 4.5.5 | Large-radii droplets | 129 |
| 4.5.6 | Large confined droplets | 131 |
| 4.5.7 | Numerical simulation results | 132 |
| 4.6 | Summary | 132 |
| 5 | Dynamics of thin film droplets | 135 |
| 5.1 | Review of the finite-dimensional ODE approximation | 136 |
| 5.2 | Refined model | 143 |
| 5.3 | Summary | 147 |

| | | |
|----------|--|------------|
| 6 | Conclusions | 149 |
| 6.1 | Steady-states of thin films in 1-D | 150 |
| 6.2 | Dynamics of thin films in 1-D | 151 |
| 6.3 | Future directions | 152 |
| 6.3.1 | Thin films on two-dimensional surfaces | 152 |
| 6.3.2 | Dynamics of thin films on heterogeneous substrates | 155 |
| | Bibliography | 160 |
| | Biography | 167 |

List of Figures

| | | |
|------|--|----|
| 2.1 | Schematic diagram of thin films on a 1-D surface | 10 |
| 2.2 | Disjoining pressure and potential | 14 |
| 3.1 | Phase plane trajectories and their corresponding profiles | 20 |
| 3.2 | Classification of a large homoclinic droplet into three regions | 22 |
| 3.3 | Exact $R(h)$ compared with the approximation $\tilde{R}(h)$ | 26 |
| 3.4 | Comparison of the approximate small-droplet solution to the numerical solution | 27 |
| 3.5 | Width of large and small droplets calculated using numerical integration and different asymptotic approximations | 29 |
| 3.6 | Eigenvalues computed numerically and analytically | 35 |
| 3.7 | Comparison of full PDE with its linearization for short time | 36 |
| 3.8 | Bifurcation diagrams for large-mass droplets on $[0, L]$ for $L = 2.5$ | 37 |
| 3.9 | Bifurcation diagrams for small-mass droplets on $[0, L]$ for $L = 2.5$ | 39 |
| 3.10 | Bifurcation diagram for m vs. h_{\max}, h_{\min} for $L = 2.5$ | 40 |
| 3.11 | Eigenvalues of steady-state droplets with fixed pressure on an increasing domain | 40 |
| 3.12 | Eigenvalues of steady-state solutions computed for a continuous range of pressure for $L = 1.5$ and $L = 2.5$ | 42 |
| 3.13 | Bifurcation diagram for m vs. h_{\min}, h_{\max} computed for $L = 1.5$ and $L = 2.5$ | 43 |
| 3.14 | Concavity of the bifurcation curve for axisymmetric solutions at the two primary bifurcation points | 52 |

| | | |
|------|---|----|
| 3.15 | Bifurcation diagram for $h(0), h(L)$ vs. m for $L = 1.4$ and $L = 3$. . . | 53 |
| 3.16 | Local structure of the bifurcation diagram for $h(0), h(L)$ vs. m for $L = 1.4$ and $L = 3$ | 54 |
| 4.1 | Bifurcation diagram for m vs. h_{\min}, h_{\max} for steady-state solutions on a homogeneous and a piecewise-patterned heterogeneous substrate . . | 59 |
| 4.2 | Asymmetry of solutions centered at $x = 0$ and $x = L$ due to the spatial dependence of $A(x)$ | 61 |
| 4.3 | Maximum film mass m_{\max} and $m_{\max} - m_{\min}$ of the inner loop structure for increasing A_2 | 61 |
| 4.4 | Definition of m_{\max} for the outer loop structure | 62 |
| 4.5 | Inner loop of the bifurcation diagram m vs. h_{\max} for steady-state solutions on a piecewise-patterned substrate with increasing A_2 . . . | 63 |
| 4.6 | Bifurcation diagram for p vs. h_{\max} for steady-states on a homogeneous and a piecewise-patterned heterogeneous substrate | 65 |
| 4.7 | Examples of profiles of steady-state solutions on branch 1 for $\bar{p} > 0$ and $\bar{p} < 0$ | 66 |
| 4.8 | Comparison of the numerical solution with the asymptotic predictions of $h(0)$ and $h(L)$ on branch 1 | 72 |
| 4.9 | Profile of two solutions on branch 1 with mass slightly above and below ϵL , computed numerically and asymptotically in two regions | 73 |
| 4.10 | Bifurcation diagram for m vs. h_{\max}, h_{\min} for branch 1 computed numerically and asymptotically | 73 |
| 4.11 | Example of a steady-state solution on branch 6 | 75 |
| 4.12 | The numerical solution of a profile on branch 6 compared with its asymptotic prediction | 77 |
| 4.13 | Bifurcation diagram for p vs. h_{\max} computed numerically and using different asymptotic approximations | 78 |
| 4.14 | Example of a steady-state solution on branch 2 | 79 |
| 4.15 | Phase plane trajectory of a solution on branch 2 | 81 |
| 4.16 | Numerical solution of a branch 2 profile compared with its asymptotic prediction in the droplet core region and near the interface $x = s$. . . | 86 |

| | | |
|------|--|-----|
| 4.17 | Numerical calculation of the bifurcation diagram for p vs. h_{\max} for branch 2 and its asymptotic approximation | 89 |
| 4.18 | An example of a pinned droplet on branch 3 | 90 |
| 4.19 | Comparison of $h(s)$ calculated numerically and asymptotically in the limit of small ϵ | 92 |
| 4.20 | Numerical solution of $h(s) - \epsilon$ compared with its asymptotic prediction in the limit of large A_2 in log scale | 93 |
| 4.21 | Bifurcation diagram for p vs. h_{\max} computed numerically and asymptotically for branch 3 | 96 |
| 4.22 | Example of a solution on branch 4 | 97 |
| 4.23 | Phase plane trajectory of a solution on branch 4 | 99 |
| 4.24 | Bifurcation diagram for p vs. h_{\max} computed numerically and asymptotically for branch 4 | 103 |
| 4.25 | Example of a steady-state solution on branch 5 | 104 |
| 4.26 | Bifurcation diagram for p vs. h_{\max} and p vs. h_{\min} for branch 5 in the limit of small ϵ | 107 |
| 4.27 | Bifurcation diagram for p vs. h_{\max} and p vs. h_{\min} for branch 5 in the limit of large A_2 | 109 |
| 4.28 | Normalized unstable eigenfunction and full PDE simulation compared with its linearization in semi-log scale | 111 |
| 4.29 | The two different stable equilibrium solutions attained by applying initial perturbation of opposite sign | 112 |
| 4.30 | Four distinct steady-states on the inner loop, all with mass $m = 0.6$ | 113 |
| 4.31 | Two distinct steady-states on the inner loop with mass $m = 1.13$ | 114 |
| 4.32 | Illustration of the measure of fluid leakage | 115 |
| 4.33 | Mass of leakage computed numerically and asymptotically for a solution on branch 2 in log scale | 117 |
| 4.34 | Mass of leakage computed numerically and asymptotically for a solution on branch 3 in log scale | 119 |

| | | |
|------|---|-----|
| 4.35 | Bifurcation diagram for m vs. p computed numerically and asymptotically for branch 1 of axisymmetric solutions | 122 |
| 4.36 | Bifurcation diagram for m vs. p computed numerically and asymptotically for branch 6 of axisymmetric solutions | 125 |
| 4.37 | Bifurcation diagram for $h(0) = h_{\max}$ vs. p of axisymmetric solutions zoomed into a range of small p and large p respectively | 133 |
| 5.1 | Pressure evolution in mass loss mode and its corresponding droplet profile | 139 |
| 5.2 | Pressure and position evolution in translation mode and its corresponding droplet profile | 141 |
| 5.3 | Pressure of a single droplet in mass loss mode given by the full PDE and the reduced ODE model in presence of increased fluxes | 141 |
| 5.4 | Pressure and position in translation mode given by the full PDE and the reduced ODE model in presence of increased fluxes | 142 |
| 5.5 | Pressure evolution in mass change mode, computed by the full PDE, the original ODE model and the refined model | 146 |
| 5.6 | Pressure and position evolution in translation mode, computed by the full PDE, the original ODE model and the refined model | 148 |
| 6.1 | Example of an equilibrium droplet on a square domain | 154 |
| 6.2 | Evolution of thin film over time on chemically homogeneous and heterogeneous substrates | 158 |

Acknowledgements

I would like to thank many people who have supported me throughout my graduate studies. First, I would like to thank my advisor Thomas Witelski for his continued patience, support and guidance on my research. The knowledge, mentorship and skill set I have learned from him will be invaluable assets for my future career.

I would also like to thank Alexander Kiselev, Jianfeng Lu and James Nolen for agreeing to be on my dissertation committee and Jian-Guo Liu for serving on my prelim committee. I am also grateful to Anita Layton for being my mentor and offering me great advice during the first year of my graduate school. My sincere thanks goes to Emily Braley, Sarah Schott and Tori Akin for their excellent advice and continued support on my teaching endeavors.

Moreover, I am thankful to my friend Ran Huo for her support and company throughout my graduate studies; Hangjie Ji for insightful discussions on my research and generous help and assistance during my transition to graduate school; Yang Su, Yu Pan, Rome Luo, Sarah Patterson, Erika Ordog, Orsola Capovilla-Searle, Dena Zhu and many more friends at Duke who have made my graduate life memorable.

Finally, I would like to express my deepest gratitude to my parents for their unconditional love, support and encouragement. This dissertation would not have been possible without them.

1

Introduction

Thin liquid films on solid substrates are often seen in nature and technology, for example, as tear film on the eye, lubricating coating and functional layers in microfluidic devices [66]. Microfluidics refers to systems that manipulate small amounts of fluids, using channels with dimensions at scale of micrometers [69]. Microfluidics has found many applications in cell biology and chemical synthesis [47, 69]. In biology, microfluidic system is used to manipulate cells, such as separation of motile and non-motile cells, observing and growing cells. Compared to conventional tissue culture dish methods, analysis of stem cells can be done in a much more systematic way using microfluidics devices [74]. The development of practical microanalytical systems has also advanced the technology in the analysis of biological samples such as blood, faeces and soil [69]. In chemistry, microfluidic devices have been recently used as a powerful tool for process intensification because of their low fabrication costs, safe operation, and capability of integrating multiple basic steps onto one chip [47].

Thin liquid films on solid surfaces experience liquid-solid intermolecular forces, which are forces that mediate interaction between liquid film and its supporting solid substrate. Early studies showed that the consideration of interactions between two

surfaces approaching each other is equivalent to the consideration of the disjoining pressure, which is a pressure due to attractive molecular forces and dependent on film thickness [10]. At the surface of the liquid film, the liquid molecules do not have neighboring molecules in all directions to provide a balanced net force. Unbalanced forces cause the liquid-gas interface to behave like a stretched membrane under surface tension [73]. In scenarios where thin films flow on inclined planes, gravity is dominant, causing changes in the shape of the free surface and dynamics of the fluid front. These forces could all drive the motion of liquid films, leading to complex patterns and phenomena such as formation of droplets, rupture and viscous fingers, which have attracted great research interests.

Films are considered to be thin if their thickness is much smaller than the length in the direction of their flow. With the small aspect ratio of thin films, the Navier-Stokes equation describing the motion of an incompressible Newtonian liquid film can be approximated by a single nonlinear partial differential equation (PDE). The simplified PDE, which is also known as a lubrication equation, describes the evolution of the free surface over time. Once the solution to the free surface is known, the velocity, pressure and energy of the fluid film can all be computed from the film thickness. This approximation, which has provided a means for understanding thin film flows, has been shown to be robust and capable of producing results that agree with experiments in previous studies [44]. This chapter briefly reviews the literature of lubrication theory applied to different physical contexts and concludes with the plan of the dissertation.

1.1 Thin films on homogeneous substrates

It has been shown that under the influence of surface tension, film droplets are spherical in shape so that the surface area exposed is minimized given a fixed volume [17].

However, classical solutions given by spherical shapes are inadequate in capturing the profiles of thin films in all physics phenomena [49]. The equilibrium shape of a liquid droplet resting on a horizontal solid surface is determined by a combination of surface tension and other external forces. A droplet forms an angle with the surface at the intersection of the liquid-solid interface. This angle, which is also known as the contact angle, is characteristic of a property of a solid surface. This property is often referred to as wettability and determines the tendency of a fluid to spread on a solid surface. The wetting property of the supporting solid substrates is typically modeled and incorporated into the framework of lubrication theory through disjoining pressure. This property of the solid substrates plays a key role in determining the equilibrium shape of a liquid droplet and has attracted increasing research attention due to its wide application in oil recovery, liquid coating and inkjet printing [8, 23, 59, 64, 73, 75]. As a consequence, more thorough analysis and modeling are needed to deepen the understanding of the influence of wettability on thin films.

Understanding the equilibrium of thin films is particularly important for understanding features of thin films such as contact angle, pressure, and position of the droplets [49]. The steady-states of thin films have been previously studied through the approach of numerical methods, asymptotic approximations and ellipsoidal droplet modeling [26, 27, 48, 49]. The different forms of disjoining pressure considered directly affects the complexity of the steady-state formulation and computations. Profiles of steady-state solutions under the action of different forms of intermolecular potentials have been investigated and described [7, 26, 27]. In one study, Glasner and Witelski considered the steady-state thin film parameterized by uniform pressure on an infinite domain. Through asymptotic matching, they showed that at leading order, large film droplets could be well approximated by parabolas [26]. In another study, Bertozzi et al. performed similar analysis and computa-

tions for steady-state thin films on finite domains. Asymptotic analysis on both the bifurcation structure and solution profile of such thin films were presented [7].

The presence of intermolecular interaction between the film and solid substrate can also cause instabilities that lead to the formation of droplets. This process is also known as dewetting. In the late stages of dewetting, droplets evolve slowly by means of translation and mass change [25]. The decrease in the total number of droplets as a result of the droplet movement and mass change is known as coarsening. One technique to study the coarsening dynamics is through Coarsening Dynamical System (CDS) [68]. The characterization of coarsening process using CDS allows for an understanding of both the associated scaling laws and statistical properties of the coarsening behavior [16]. In 2002, by introducing a slow time scale and employing solvability conditions given by Fredholm alternative, Glasner and Witelski derived a finite dimensional system of ODEs from the full evolution equation of thin films in 1-D that is capable of predicting the coarsening dynamics of droplets. The reduced ODE system is similar to that derived from Cahn-Hilliard equation, which describes the evolution of the position of kinks [2, 4]. Glasner and Witelski demonstrated the success of their ODE approximation in giving good predictions of large droplets behavior in presence of small imposed fluxes at the boundary of large finite domains [26].

1.2 Thin films on heterogeneous substrates

Much theoretical understanding of thin films has been limited to films on homogeneous substrates. However, most of the naturally occurring surfaces are chemically heterogeneous due to contamination, cavities, etc. Tailored chemically heterogeneous substrates are also increasingly used for the engineering of micropatterns of thin films [76]. Liquid flow on chemically patterned substrate has been studied extensively due

to its various applications in microfluidics that require accurate dispensing and distribution of liquids on solid surfaces. One example of such applications is in the design of the chemical patterns of the nozzle plate in inkjet print heads [9, 42]. Inkjet technology makes use of tiny ink drops to recreate digital image. Due to its non-contacting nature, it can be used to print on various media. It is also widely used to print electronics. Several types of important components have been fabricated by inkjet printing technique [39]. Designing suitable chemical patterns to control the motion of the ink and quantifying the characteristics of wetting layer on the nozzle plate are critical to improving the printing quality and resolution [9, 42]. Another application can be found in microcontact printing where a stamp is used to transfer the material onto a substrate to create a desired pattern. The pattern is generated through contact between the stamp and the surface [20]. Understanding the shape of liquids at equilibrium on chemically patterned substrate is essential to optimizing the printing process [20]. Chemically patterned substrates also have applications in electronic industry. Wang et al. developed a dewetting process for fabricating polymer field effect transistors where conducting polymer is used as electrodes [67]. A patterned substrate with a hydrophobic stripe in the middle is used to separate a liquid droplet into two parts where the two dewetted parts are used as the source and drain electrodes. Controlling the chemical patterning is crucial for fabricating film transistors with short-channel that has length at micro/nanometer scale [67].

Previously, Kargupta et al. [35, 36, 37] studied the instability and pattern formation in thin film on chemically heterogeneous substrates with a stepwise pattern. On such substrates, they identified a mode of surface instability caused by the spatial gradient of intermolecular force across the solid substrate. By performing a linear stability analysis of the thin film equation, they computed the characteristic time scale for the growth of instability and verified that the time scale is inversely pro-

portional to the potential difference caused by heterogeneity. They showed that the introduction of heterogeneity could destabilize spinodally stable films and reduce the time of rupture for thicker films [35, 37]. Lenz and Lipowsky investigated the morphologies of different equilibrium states of liquids on a surface that consists of hydrophilic domains in a hydrophobic matrix. By minimizing the interfacial free energy subject to constant liquid volume, they found that the different morphologies are determined by the liquid volume and the area fraction of the hydrophilic domains. They also identified the transition among three different regimes using liquid volume as a parameter [45]. On a chemically heterogeneous substrate, the contact angle may no longer be described by Young's equation. Kooij et al. showed that on a stripe-patterned surface, the contact angle formed can be well approximated in terms of the width ratio of the two different stripes using Cassie's law [42]. Kaspar et al. explored the effect of alternating hydrophobic and hydrophilic area of a rectangular micro-arrayed surface on the overall confinement and spillover of water droplets. They derived the contact angle as an arctan function of droplet height, using the assumption of a spherical cap geometry and a coefficient that accounts for the properties of the confining surface [38].

In the framework of lubrication approximation, Thiele et al. [66] studied the effect of a smoothly patterned substrate on stationary droplet profiles using wettability as a control parameter. Their work considered heterogeneous substrate modeled by a small-amplitude sinusoidal modulation. By varying the amplitude and periodicity of the chemical pattern, they identified the parameter range where the pinning mechanism emerges from coarsening. Kao et al. [34] also studied the effect of introducing a small sinusoidal wettability contrast on the steady-state thin film with and without rupture. In addition, Kao et al. [34] also considered substrates with small-amplitude square-wave patterning. Imperfect bifurcation was observed in solutions on hetero-

geneous substrates. By using weakly nonlinear analysis, they derived predictions for steady-state profile, stability and rupture time of thin films on square-wave patterned substrates in the limit of small wettability contrast. By using both experiments and numerical simulations, Brasjen and Kondic [11, 41] studied the dynamics of fluid fronts of films on chemically patterned heterogeneous substrate.

1.3 Plan of the dissertation

This dissertation focuses on the mathematical models of dynamics and steady-states of thin liquid films on chemically homogeneous and heterogeneous substrates. The plan of this dissertation is shown as follows.

- In Chapter 2, we show the derivation of the lubrication equation from the Navier-Stokes equation, which describes the flow of thin liquid film of viscous fluid. In particular, we consider the lubrication approximation for thin films driven by intermolecular forces and surface tension.
- In Chapter 3, we present the formulation and asymptotic analysis of 1-D and axisymmetric steady-state solutions on chemically homogeneous substrates. We review previous analysis on large homoclinic droplets and derive a new analytical approximation for small homoclinic droplets in 1-D. We also examine and discuss the stability and bifurcation of both 1-D and axisymmetric solutions on finite homogeneous substrates.
- In Chapter 4, we study the 1-D steady-state solutions of thin films on chemically heterogeneous substrates. We consider the thin film flow on stepwise patterned substrates of finite length. Based on the structure of the bifurcation diagram, we classify all the steady-state solutions that could exist on such substrates into six different categories, which correspond to the six different branches of

the bifurcation curve. For each branch, we derive the asymptotic prediction of the steady-state profile and study the asymptotic behavior of the solution in the limit of large heterogeneity contrast. We show that the analysis for 1-D solutions can be easily extended to axisymmetric solutions.

- In Chapter 5, we first review and examine the reduced finite-dimensional ODE model proposed by Glasner and Witelski, which predicts the dynamics of droplets on large finite domains. Through numerical simulations, we illustrate the limitation of the model in presence of increased fluxes. By modifying the asymptotic expansion used in the original ODE model, we propose a refined model that predicts the single-droplet behavior on finite domains subject to fluxes. We show the refined model produces predictions that improve the accuracy of the previous model.
- In Chapter 6, we conclude the dissertation with a summary and discuss future directions of research that could arise from our current studies, including the steady-states and dynamics of thin films on two-dimensional surfaces, efficient computational methods for solving thin films on two-dimensional domains and the dewetting and coarsening process of thin films on chemically heterogeneous substrates.

2

Lubrication equation

2.1 Derivation

We follow the approach of O'Brien et al. [52] and Oron et al. [55], which exploits the small aspect ratio and the method of asymptotic expansion to show the derivation of the lubrication approximation. The Navier-Stokes equation describing incompressible Newtonian flow in two dimensions is given by

$$\rho(u_t + uu_x + wu_z) = -p_x + \mu(u_{xx} + u_{zz}) - \phi_x \quad (2.1a)$$

$$\rho(w_t + uw_x + ww_z) = -p_z + \mu(w_{xx} + w_{zz}) - \phi_z \quad (2.1b)$$

$$u_x + w_z = 0 \quad (2.1c)$$

where $\mathbf{u} = (u, w)$ is the velocity vector, p is the pressure, ρ is the density, μ is the viscosity and ϕ represents the potential of other body forces. A schematic diagram illustrating a layer of a thin film resting on a flat horizontal solid surface is shown in Figure 2.1.

We nondimensionalize the system by writing $x = L\tilde{x}$, $z = H\tilde{z}$, $u = U\tilde{u}$, $w = W\tilde{w}$, $t = \frac{L}{U}\tilde{t}$, $p = P\tilde{p}$ and $\phi = \Phi\tilde{\phi}$. Assume $\frac{H}{L} = \epsilon \ll 1$. The incompressibility condition (2.1c) gives $W = \epsilon U$. To balance $-p_x$ and μu_{zz} on the right hand side of (2.1a), let

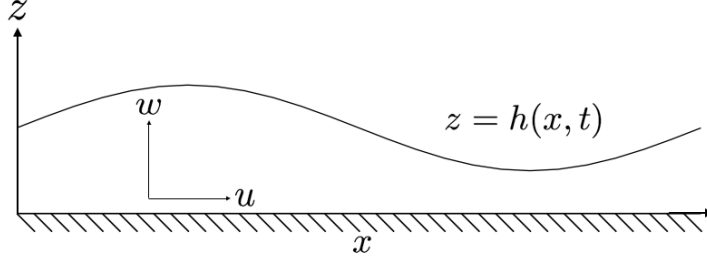


FIGURE 2.1: Schematic diagram of thin films on a flat horizontal solid surface

$P = \frac{\mu U}{\epsilon^2 L}$. The scaled equations become

$$\epsilon^2 Re(\tilde{u}_{\tilde{t}} + \tilde{u}\tilde{u}_{\tilde{x}} + \tilde{w}\tilde{u}_{\tilde{z}}) = -\tilde{p}_{\tilde{x}} + \mu(\epsilon^2 \tilde{u}_{\tilde{x}\tilde{x}} + \tilde{u}_{\tilde{z}\tilde{z}}) - \tilde{\phi}_{\tilde{x}} \quad (2.2a)$$

$$\epsilon^4 Re(\tilde{w}_{\tilde{t}} + \tilde{u}\tilde{w}_{\tilde{x}} + \tilde{w}\tilde{w}_{\tilde{z}}) = -\tilde{p}_{\tilde{z}} + \mu(\epsilon^4 \tilde{w}_{\tilde{x}\tilde{x}} + \epsilon^2 \tilde{w}_{\tilde{z}\tilde{z}}) - \tilde{\phi}_{\tilde{z}} \quad (2.2b)$$

$$\tilde{u}_{\tilde{x}} + \tilde{w}_{\tilde{z}} = 0 \quad (2.2c)$$

where $Re = \frac{\rho LU}{\mu}$. Here, we assume $Re = O(1)$ and consider thin film driven by surface tension, so surface tension dominates. Let σ represent surface tension and T denote the stress tensor. Since for Newtonian fluids, $T_{ij} = -p\delta_{ij} + \mu(\frac{\partial u_i}{\partial x_j} + \frac{\partial u_j}{\partial x_i})$, we nondimensionalize T using the scale of P , i.e.

$$\mathbf{T} = \tilde{\mathbf{T}} \frac{\mu U}{\epsilon^2 L} \quad (2.3)$$

In non-dimensional form, we have

$$\tilde{T}_{11} = -\tilde{p} + 2\epsilon^2 \tilde{u}_{\tilde{x}} \quad (2.4a)$$

$$\tilde{T}_{12} = \tilde{T}_{21} = \epsilon \tilde{u}_{\tilde{z}} + \epsilon^3 \tilde{w}_{\tilde{x}} \quad (2.4b)$$

$$\tilde{T}_{22} = -\tilde{p} + 2\epsilon^2 \tilde{w}_{\tilde{z}} \quad (2.4c)$$

This shows to leading order, $\tilde{T}_{ij} = -\tilde{p}\delta_{ij} + O(\epsilon)$, regardless of the scale of U . Let $\tilde{h}(\tilde{x}, \tilde{t})$ be the nondimensionalized free surface. The normal stress balance at the surface is given by

$$\mathbf{n} \cdot \mathbf{T} \cdot \mathbf{n} = \sigma(\nabla \cdot \mathbf{n}) \quad (2.5)$$

At the free surface $z = \tilde{h}(\tilde{x}, \tilde{t})$, the normal vector is given by $\mathbf{n} = (-\epsilon\tilde{h}_{\tilde{x}}, 1)(1 + \epsilon^2\tilde{h}_{\tilde{x}}^2)^{-\frac{1}{2}}$. To leading order, the jump in normal stress across the interface must balance the curvature force. This leads to the velocity scale $U = \frac{\sigma\epsilon^3}{\mu}$. It follows that the normal stress balance condition then yields

$$\tilde{p} = -\tilde{h}_{\tilde{x}\tilde{x}} \quad (2.6)$$

The surface tension σ is a constant. The shear stress on the surface is zero due to the stress balance in the tangential direction, given by

$$\mathbf{n} \cdot \mathbf{T} \cdot \mathbf{t} = \nabla \sigma \cdot \mathbf{t} \quad (2.7)$$

For convenience, we now remove \sim in the variables in (2.2a)-(2.2c) to denote the non-dimensional form of (2.1a)-(2.1c). Ignoring terms of higher order, (2.2a)-(2.2b) become

$$u_{zz} = p_x + \phi_x \quad (2.8a)$$

$$0 = p_z + \phi_z \quad (2.8b)$$

Integrating (2.8b) with respect to z , we obtain

$$p + \phi = \bar{p}(x) \quad (2.9)$$

where $\bar{p}(x)$ denotes the variable of integration. Using (2.6) at $z = h(x, t)$, we get

$$p = -\phi - h_{xx} + \phi \Big|_{z=h} \quad (2.10)$$

The supporting solid substrates exert intermolecular forces on thin films. This intermolecular interaction is described by disjoining pressure, which is the excess pressure required to evaporate liquid molecules due to the presence of solid-liquid intermolecular forces [33]. Classic theory predicts that the disjoining pressure is a function of

film thickness h so $\phi = \phi(h)$ [31]. It is obtained by a pairwise summation of interactions among molecules of the thin films and the substrates [62]. This implies $\phi_x = 0$ and p_x is independent of z . Now we integrate (2.8a) in the z direction and apply the shear stress condition $u_z(h) = 0$. Since p_x is independent of z , we have

$$p_x(h - z) = -u_z \quad (2.11)$$

Next, we integrate (2.11) in the z direction again and apply the no-slip boundary condition $u(0) = 0$. This gives

$$u = p_x \left(\frac{1}{2} z^2 - hz \right) \quad (2.12)$$

If we use the no-slip boundary condition $w(0) = 0$ to rewrite the incompressibility condition (2.2c) as

$$w = w(0) - \int_0^h u_x dz = - \int_0^h u_x dz \quad (2.13)$$

then by combining (2.13) with the kinematic boundary condition $h_t + uh_x = w$, we have

$$\frac{\partial h}{\partial t} = \frac{1}{3} \frac{\partial}{\partial x} \left(h^3 \frac{\partial p}{\partial x} \right) \quad (2.14)$$

where $p = -\phi - h_{xx} + \phi \Big|_{z=h}$. In the problem of our interest, we primarily consider external force given by the intermolecular interaction between fluid film and solid substrate, which is described by disjoining pressure. Here we denote the disjoining pressure by $\Pi(h)$ so the pressure p is given by

$$p = \Pi(h) - h_{xx} \quad (2.15)$$

The form of the disjoining pressure $\Pi(h)$ is discussed in more detail in Section 2.2.

2.2 Disjoining pressure

The disjoining pressure $\Pi(h)$ describes the interaction between the liquid film and the supporting solid substrate. As the distance between two interfaces decreases, the two interfaces experience increasingly repulsive intermolecular force. In this study, we consider a disjoining pressure of the form

$$\Pi(h) = A\epsilon^{-1} \left(\frac{\epsilon}{h}\right)^n \left[1 - \left(\frac{\epsilon}{h}\right)^{m-n}\right] \quad (2.16)$$

Specifically, we consider $(n, m) = (3, 4)$, which is a 3-4 power law potential used in [26, 53, 54]. For $(n, m) = (3, 4)$, the disjoining pressure can also be conveniently written as

$$\Pi(h) = A \left(\frac{\epsilon^2}{h^3} - \frac{\epsilon^3}{h^4} \right) \quad (2.17)$$

The constant A is called Hamaker constant, which measures the strength of intermolecular interaction between the thin liquid film and solid substrate. It determines the equilibrium contact angle of the droplets formed on the substrates. It is made spatially dependent to model striped chemical patterning of solid substrates in Chapter 4. $\epsilon > 0$ is a small positive parameter that sets the scale of the minimum film thickness. Note that this ϵ is not the same ϵ introduced in the nondimensionalization of the Navier-Stokes equation described in Section 2.1.

The interaction between two interfaces can also be discussed in terms of the energy potential $U(h)$ where $\frac{dU}{dh} = \Pi(h)$. A sketch of the disjoining pressure given by (2.17) with parameters $A = 1$ and $\epsilon = 0.1$ and its corresponding potential is shown in Figure 2.2. Note that $\Pi(\epsilon) = 0$ and $\Pi(h)$ attains a maximum at $h = \frac{4}{3}\epsilon$. The potential $U(h)$ has a global minimum at $h = \epsilon$.

The dewetting of thin films is the process of destabilization of films that leads to the formation of connected droplets. Two main dewetting processes have been

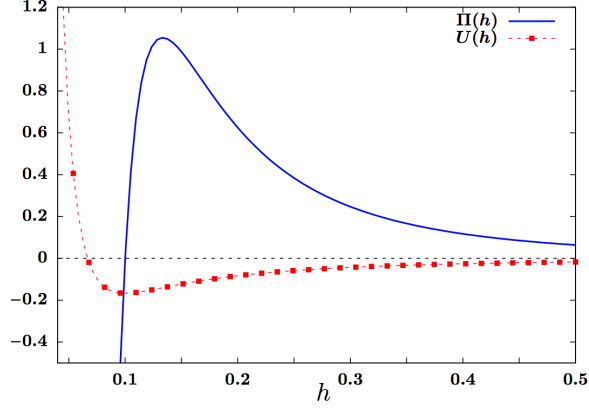


FIGURE 2.2: Disjoining pressure of the form (2.17) and its corresponding potential, with $A = 1$ and $\epsilon = 0.1$.

identified, i.e. nucleation of holes and the amplification of perturbations at the free surface. The latter is a consequence of destabilizing intermolecular force and is also known as spinodal dewetting. The dynamics and instability of thin films are controlled by both surface tension and intermolecular force [28]. It has been shown that unstable modes exist for $U''(h) < 0$ [32]. The inclusion of intermolecular force in lubrication approximation is important for capturing dewetting mechanisms observed in experiments.

2.3 Summary

In this chapter, we presented the derivation of lubrication equation that describes the motion of thin liquid films driven by surface tension and intermolecular force on 1-D solid surfaces. More specifically, we discussed the form of the disjoining pressure of our consideration and its potential influence on the overall dynamics of thin liquid films. Previous studies have shown that if the disjoining pressure only models the attractive force without the repulsive force, i.e. $\Pi(h) = \frac{A}{h^3}$, then rupture of thin films can occur when solutions cease to exist in finite time, i.e. when film thickness $h(x, t) \rightarrow 0$ for some x [15, 18, 22, 34, 46, 58, 70]. However, if we assume

disjoining pressure of the form (2.16) which includes both attractive and repulsive forces, then for $\epsilon > 0$, the lubrication equation (2.14) has solutions that exist for all time [7]. Lubrication equation has been an effective approach for the investigation of the evolution and pattern formation of thin liquid films under the action of different forms of intermolecular forces [25, 26, 53, 54, 57, 62]. The growth of instabilities caused by intermolecular forces eventually results in the formation of quasi-stable array of droplets separated by ultra-thin films. A more detailed description of the mechanisms of the evolution is discussed in Chapter 5.

3

Steady-states and bifurcations

In this chapter, we study the steady-state solutions of the evolution equation of thin films on $[-L, L]$ given by (2.14), which, after rescaling, is given below.

$$\frac{\partial h}{\partial t} = \frac{\partial}{\partial x} \left(h^3 \frac{\partial p}{\partial x} \right) \quad (3.1)$$

where

$$p = \Pi(h) - \frac{\partial^2 h}{\partial x^2} \quad (3.2)$$

It is convenient to write (3.1) as

$$\frac{\partial h}{\partial t} = \frac{\partial J}{\partial x} \quad (3.3)$$

where J is the flux given by

$$J = h^3 \frac{\partial p}{\partial x} \quad (3.4)$$

The energy associated with (3.1) is given by

$$E(h) = \int_{-L}^L U(h) + \frac{1}{2} h_x^2 \, dx \quad (3.5)$$

The mass of the fluid film on $[-L, L]$ is given by

$$m = \int_{-L}^L h(x, t) \, dx \quad (3.6)$$

If we consider (3.1) subject to no-flux boundary conditions, i.e.

$$J(\pm L) = 0, \quad \frac{\partial h}{\partial x}(\pm L) = 0 \quad (3.7)$$

then $\frac{dm}{dt} = 0$ and the total fluid mass is conserved in time. The condition $\frac{\partial h}{\partial x}(\pm L) = 0$ means that the vertical wall at the boundary is non-wetting and that there is no meniscus formed at the boundary. Moreover, this condition allows for an even extension of the solution to obtain a periodic array of droplets. If we use product rule to expand the flux J , we have

$$J = h^3 \left(\Pi'(h) \frac{\partial h}{\partial x} - \frac{\partial^3 h}{\partial x^3} \right) \quad (3.8)$$

It follows that the boundary condition (3.7) then reduces to

$$\frac{\partial h}{\partial x}(\pm L) = 0, \quad \frac{\partial^3 h}{\partial x^3}(\pm L) = 0 \quad (3.9)$$

Subject to no-flux boundary conditions, the rate of energy dissipation is given by

$$\frac{dE}{dt} = - \int_{-L}^L h^3 p_x^2 \, dx \leq 0 \quad (3.10)$$

In Section 3.1, we present the nontrivial steady-state solutions subject to no-flux boundary conditions, which are governed by a second order ODE and parametrized by uniform pressure $p \equiv \bar{p}$. We briefly review the phase plane analysis of the steady-state ODE and illustrate the existence of a homoclinic orbit in the phase plane that encloses all of the periodic solutions. To provide an analytical description of

the steady-state profiles, we first review the asymptotic approximations previously derived for homoclinic droplets in the limit of large mass. Then we develop a new approximation for homoclinic droplets in the limit of small mass by introducing an approximate steady-state equation through a minimization approach.

In Section 3.3, we study the stability of steady-states on finite domains through linear stability analysis. By investigating the bifurcation diagram of steady-states on finite domains, we illustrate the stability change of steady-states as pressure \bar{p} and period L cross critical values. We show through numerical computations of bifurcation diagrams that in the limit of small mass and $p \rightarrow p_{\max}$, the stability of the periodic steady-states has a dependence on L . For a small droplet with \bar{p} near p_{\max} , there exists a critical period L^* , at which the droplet changes from being stable to unstable. We also show that as the period L increases, the bifurcation diagram goes through a structural change near the bifurcation point where small-mass droplet bifurcates from flat film.

3.1 Steady-state solutions in 1-D

To study the steady-states of (3.1), let $\frac{\partial h}{\partial t} = 0$. Subject to no-flux boundary conditions $J(\pm L) = 0$, we have $J = h^3 \frac{\partial p}{\partial x} \equiv 0$. It follows that $\frac{\partial p}{\partial x} \equiv 0$ and consequently $p \equiv \bar{p}$ uniformly for some constant \bar{p} on $[-L, L]$. Hence, the steady-states of (3.1) subject to no-flux boundary conditions have uniform constant pressure $p \equiv \bar{p}$ and are governed by

$$\frac{d^2 h}{dx^2} = \Pi(h) - \bar{p} \quad (3.11)$$

The solutions $h(x; \bar{p})$ are a class of solutions parametrized by uniform pressure $p \equiv \bar{p}$. Let h_c be the local maximum of $\Pi(h)$ so $\Pi'(h_c) = 0$. Considering a disjoining pressure

$\Pi(h)$ of the form (2.17), i.e.

$$\Pi(h) = A \left(\frac{\epsilon^2}{h^3} - \frac{\epsilon^3}{h^4} \right) \quad (3.12)$$

with Hamaker constant $A = 1$, we have $h_c = \frac{4}{3}\epsilon$. $p_{\max} = \Pi\left(\frac{4}{3}\epsilon\right) = \frac{27}{256\epsilon}$ is the maximum of the pressure for all nontrivial steady-state solutions.

To do a phase plane analysis for the steady-state solutions, we rewrite the second order ODE (3.11) as a system of first order ODEs, given by

$$\begin{cases} h' = y \\ y' = \Pi(h) - \bar{p} \end{cases} \quad (3.13)$$

$\Pi(h) = \bar{p}$ has two roots for $0 < \bar{p} < p_{\max}$, with one root smaller than $h_c = \frac{4}{3}\epsilon$ and the other root larger than $h_c = \frac{4}{3}\epsilon$. Denote the smaller root by h_{\min} and the larger root by h_{cen} . The Jacobian of the system (3.13) is given by

$$\mathcal{J} = \begin{bmatrix} 0 & 1 \\ \Pi'(h) & 0 \end{bmatrix} \quad (3.14)$$

The eigenvalues of the Jacobian are given by $\lambda^2 = \Pi'(h)$. At $h = h_{\min}$, $\lambda^2 = \Pi'(h_{\min}) > 0$ so $\lambda = \pm\sqrt{\Pi'(h_{\min})}$ and h_{\min} is a saddle point. At $h = h_{\text{cen}}$, $\lambda^2 = \Pi'(h_{\text{cen}}) < 0$ so h_{cen} is a center. There is a homoclinic orbit that passes through the saddle point $(h_{\min}, 0)$ in the phase plane h vs. h_x . Note that h_{\min} is the minimum film thickness of the homoclinic solution. This homoclinic orbit encloses all of the periodic solutions that orbit around the center $(h_{\text{cen}}, 0)$. Figure 3.1 (a) illustrates the phase plane trajectory of the homoclinic orbit where $h_x \rightarrow 0$ as $h \rightarrow h_{\min}$ (solid black curve), a periodic solution bounded inside the homoclinic orbit (red dotted curve), and a solution that lies entirely outside of the homoclinic orbit with $h_x \rightarrow \pm\infty$ as

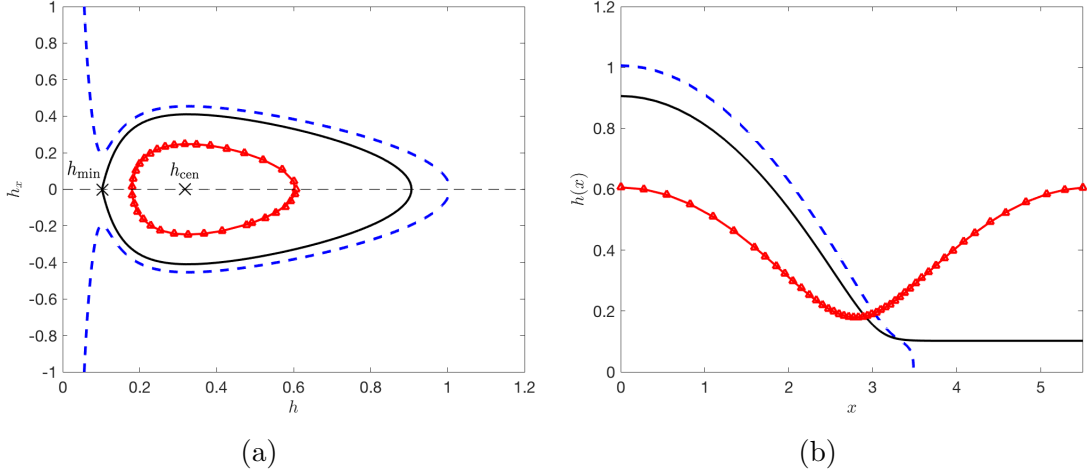


FIGURE 3.1: (a) Phase plane trajectory of the homoclinic orbit (solid black curve), a periodic solution (red dotted curve) and a solution that lies outside of the homoclinic orbit (dashed blue curve). (b) Profile of the three solutions corresponding to the three trajectories shown in (a), with parameter values $\bar{p} = 0.2$, $\epsilon = 0.1$.

$h \rightarrow 0$ (dashed blue curve). Note that if a steady-state lies outside of the homoclinic orbit, then $h_x \rightarrow \infty$ as $h \rightarrow 0^+$. This type of steady-state solutions will not be attained from the time-dependent PDE [7]. As a result, we will focus primarily on the periodic steady-state and homoclinic steady-state solutions. Figure 3.1 (b) shows the three droplet profiles that correspond to the three different trajectories plotted in Figure 3.1 (a).

3.1.1 Large homoclinic droplets

Multiplying both sides of (3.11) by $\frac{dh}{dx}$ and integrating, we can write (3.11) as a first order ODE given by

$$\frac{1}{2} \left(\frac{dh}{dx} \right)^2 = U(h) - \bar{p}h + C \quad (3.15)$$

where $U(h)$ is the potential such that $\frac{dU}{dh} = \Pi(h)$ and C is some constant. Corresponding to the disjoining pressure given by (3.12), $U(h)$ is given by

$$U(h) = -\frac{1}{2} \frac{\epsilon^2}{h^2} + \frac{1}{3} \frac{\epsilon^3}{h^3} \quad (3.16)$$

Now we determine the constant C for the homoclinic solution. In the phase plane, we know $h \rightarrow h_{\min}$ as $h_x \rightarrow 0$. This suggests (3.15) for the homoclinic solution is given by

$$\frac{1}{2} \left(\frac{dh}{dx} \right)^2 = R(h) \quad (3.17)$$

where

$$R(h) = U(h) - \bar{p}h - U(h_{\min}) + \bar{p}h_{\min} \quad (3.18)$$

Let h_{\max} denote the maximum film thickness of the homoclinic solution. At the maximum of the film droplet, $h_x = 0$, so we can compute h_{\max} by solving $R(h_{\max}) = 0$.

Asymptotic analysis for large droplets has been previously studied [7, 25, 26]. A droplet is considered large if $h_{\max} \gg \epsilon$ and consequently droplet width and droplet mass are also large compared to ϵ . This also means the droplet pressure is small. Specifically, analysis has been performed for large-mass droplets in the limit $\epsilon \rightarrow 0$ [26]. The structure of a large-mass droplet has been classified into three different regimes, (i) droplet core, (ii) contact line and (iii) ultra-thin film [26], as illustrated in Figure 3.2. The droplet core is a region where the majority of the fluid film concentrates and $h = O(1)$. The ultra-thin film region is a region where the solution is characterized by a uniform and flat film with $h \sim \epsilon$. The contact line region is an intermediate region that connects the droplet core and ultra-thin film where the matching between the two regions occurs.

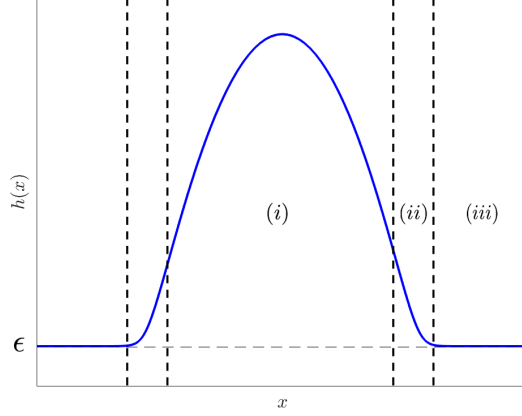


FIGURE 3.2: Classification of a large homoclinic droplet into three regions.

For large-mass droplets, inside the droplet core, $h_{\max} = O(1)$. As $\epsilon \rightarrow 0$, $\Pi(h) = O(\epsilon^2) \ll \bar{p}$. At $O(1)$, (3.11) can be described by

$$\frac{d^2 h}{dx^2} \sim -\bar{p} \quad (3.19)$$

The profile of a large droplet for $0 < x \ll w$, where w is a measure for the droplet width to be discussed shortly, can thus be described by the parabola

$$h(x) \sim -\frac{1}{2}\bar{p}x^2 + h_{\max} \quad (3.20)$$

For a large droplet, in the limit $\epsilon \rightarrow 0$, an effective width estimate can be computed using (3.20) by solving $h(w) \sim 0$, which gives

$$h_{\max} \sim \frac{1}{2}\bar{p}w^2 \quad (3.21)$$

Homoclinic solution exists on the infinite domain $(-\infty, \infty)$. Outside of $(-w, w)$, $h(x) - h_{\min}$ is exponentially small.

In the ultra-thin film region, $h(x) \sim \epsilon$ so $h_{\min} = \epsilon$. To find an asymptotic prediction of h_{\min} , we seek solution $\Pi(h_{\min}) = \bar{p}$ for h_{\min} near ϵ . Writing out the

Taylor expansion of $\Pi(h)$ near $h = h_{\min}$, we have

$$\Pi(\epsilon) + \Pi'(\epsilon)(h_{\min} - \epsilon) \sim \bar{p} \quad (3.22)$$

Hence, to next order, h_{\min} is given by

$$h_{\min} \sim \epsilon + \frac{\epsilon^2}{\bar{p}} \quad (3.23)$$

By (3.23) and $U(h)$ given in (3.16), we know $U(h_{\min}) = O(1)$ and $ph_{\min} = O(\epsilon)$.

Hence, at $O(1)$, the equation $R(h_{\max}) = 0$ is given by

$$\bar{p}h_{\max} \sim -U(h_{\min}) \sim -U(\epsilon) \quad (3.24)$$

which yields

$$h_{\max} \sim -\frac{U(\epsilon)}{\bar{p}} = \frac{1}{6\bar{p}} \quad (3.25)$$

Equating (3.25) and (3.21) yields an estimate for width, given by

$$w \sim \frac{1}{\sqrt{3\bar{p}}} \quad (3.26)$$

Besides the droplet width, Glasner and Witelski have also derived the equilibrium contact angle formed by the droplet in the limit of small ϵ [26]. To derive the contact angle, they focused on the solution in the contact line region. To match the droplet core and ultra-thin film region, they rescaled the solution by writing $h(x) = \epsilon H(Z)$ for $Z = \frac{w-x}{\epsilon}$. At $O(1)$, the steady-state equation (3.17)-(3.18) can then be written in terms of $H(Z)$ as

$$\frac{1}{2} \left(\frac{dH}{dZ} \right)^2 = U(\epsilon H) - U(\epsilon) \quad (3.27)$$

As $Z \rightarrow -\infty$, solution extends to the ultra-thin film region where $H(Z) \rightarrow 1$ and $H'(Z) \rightarrow 0$. As $Z \rightarrow \infty$, the solution extends to the droplet core region where

$H \rightarrow O\left(\frac{1}{\epsilon}\right)$ and thus $U(\epsilon H) \ll 1$, yielding

$$\frac{1}{2} \left(\frac{dH}{dZ} \right)^2 = -U(\epsilon) \quad (3.28)$$

Hence,

$$\left. \frac{dh}{dx} \right|_w = -\sqrt{-2U(\epsilon)} = -\frac{1}{\sqrt{3}} \quad (3.29)$$

The contact angle θ is thus $\frac{1}{\sqrt{3}}$, which suggests that the equilibrium contact angle of the homoclinic droplet is independent of the droplet pressure \bar{p} .

3.1.2 Small homoclinic droplets

The analysis presented in Section 3.1.1 is valid for large drops where $h_{\max} = O(1)$. As the droplet pressure \bar{p} increases and approaches p_{\max} , h_{\max} decreases and h_{\min} increases. The assumption $\Pi(h) \ll 1$ is no longer valid. The profile of the small droplets can no longer be described by a parabola. Analytical solutions of small droplets for disjoining pressure $\Pi(h)$ of power law $(n, m) = (2, 3)$ and $(n, m) = (3, 4)$ have been previously studied [27, 49]. For $(n, m) = (2, 3)$, Gomba et al. presented an analytical solution of small droplets using arctanh function. However, the solution $h(x; \bar{p})$ was expressed implicitly [27]. Intyre et al. later derived an asymptotic expression for small steady-state droplets for disjoining pressure of the form $(n, m) = (3, 4)$. The solution was given in an implicit form and expressed in terms of elliptic integrals. In this section, we study the profile of droplets in the limit of small mass and present a new analytical description of these small droplets using an explicit hyperbolic trigonometric function. The new solution is attained by introducing and solving an approximate steady-state equation. This new approximation can be conveniently used to describe small homoclinic droplet profiles.

In the limit $\bar{p} \rightarrow p_{\max}$, $h_{\max}(\bar{p}) - h_{\min}(\bar{p}) = O(\epsilon)$. If we consider the Taylor series expansion of $R(h)$ at $h = h_{\min}$, then for h near h_{\min} , we have

$$R(h) = \frac{1}{2}\Pi'(h_{\min})(h - h_{\min})^2 + O(|h - h_{\min}|^3) \quad (3.30)$$

Similarly, using a Taylor series expansion for $R(h)$ at $h = h_{\max}$, for h near h_{\max} , we have

$$R(h) = \Pi(h_{\max})(h - h_{\max}) + O(|h - h_{\max}|^2) \quad (3.31)$$

In the limit $\bar{p} \rightarrow p_{\max}$, $h_{\min}(\bar{p}) < h(x) < h_{\max}(\bar{p})$. Suggested by (3.30)-(3.31), we consider an approximation of $R(h)$, given by $\tilde{R}(h)$ of the form

$$\tilde{R}(h) = a^2(h - h_{\min})^2(h_{\max} - h) \quad (3.32)$$

for some constant a . We choose $a > 0$ so that $\|\sqrt{R(h)} - \sqrt{\tilde{R}(h)}\|_2$ is minimized, which yields

$$a = \frac{\int_{h_{\min}}^{h_{\max}} \sqrt{R(h)}(h - h_{\min})\sqrt{h_{\max} - h}dh}{\int_{h_{\min}}^{h_{\max}} (h - h_{\min})^2(h_{\max} - h)dh} \quad (3.33)$$

Figure 3.3 shows a comparison of the exact $R(h)$ and its approximated version $\tilde{R}(h)$ for $\bar{p} = 1.03$. To obtain an approximate description of droplets in the limit of small mass, we solve the approximate steady-state equation

$$\frac{dh}{dx} = -\sqrt{2\tilde{R}(h)} \quad (3.34a)$$

$$h(0) = h_{\max} \quad (3.34b)$$

The solution to (3.34a) subject to the condition (3.34b) is given by

$$\tilde{h}(x; \bar{p}) = (h_{\max} - h_{\min})\text{sech}^2\left(\sqrt{\frac{h_{\max} - h_{\min}}{2}}ax\right) + h_{\min} \quad (3.35)$$

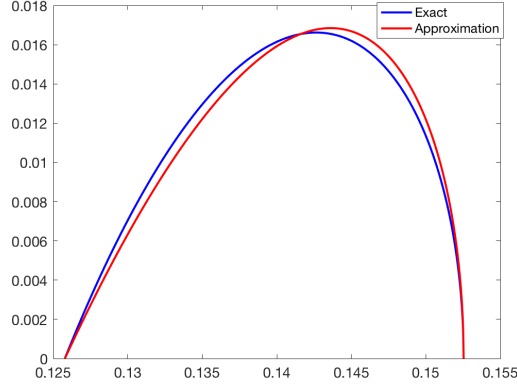


FIGURE 3.3: Exact $R(h)$ compared with its approximate version $\tilde{R}(h)$ for $\bar{p} = 1.03$

where h_{\min} still denotes the minimum film thickness of the homoclinic droplet. The approximate solution (3.35) captures the property that the solution exists on an infinite domain with a long tail that extends to $\pm\infty$ and $h(x; \bar{p}) \rightarrow h_{\min}$ as $x \rightarrow \pm\infty$. Figure 3.4 shows a comparison between the numerically solved steady-state homoclinic solution for $\bar{p} = 1.03$ and the solution to the approximate equation (3.34a), given by (3.35). The solid blue curve represents the numerical solution. The dashed red curve represents the approximate solution. The numerical simulation results suggest that (3.35) produces a good prediction of the droplet profile in the limit $p \rightarrow p_{\max}$.

As can be observed from the solution computed both numerically and using (3.35), droplets in the small mass limit are characterized by longer tails, compared to large parabolic droplets. The width estimate for large droplets, given by (3.26), will no longer be accurate for small droplets. To measure the width of small droplets more effectively, we need a new width measure. By (3.17), we know for a full droplet on $[-L, L]$, the droplet attains a maximum at $x = 0$ and is decreasing on $[0, L]$.

$$\frac{dh}{dx} = -\sqrt{2R(h)} \quad (3.36)$$

Rearranging terms and integrating from h_{cen} to h_{\max} , we obtain the distance incre-

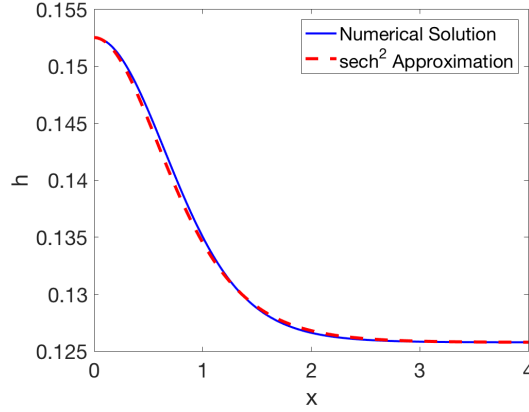


FIGURE 3.4: Numerical solution of the droplet profile compared with the analytical solution to the approximate steady-state equation (3.34a) for $\bar{p} = 1.03$. The approximate solution is given by (3.35).

ment in x for $h(x)$ to decrease from h_{\max} to h_{cen} . We denote this distance by w_1 .

Integration yields

$$w_1 = \int_{h_{\text{cen}}}^{h_{\max}} \frac{1}{\sqrt{2R(h)}} dh \quad (3.37)$$

Note that where $h(x) = h_{\text{cen}}$, $h(x)$ has an inflection point. To estimate the distance in x for $h(x)$ to decay from h_{cen} to h_{\min} , we use the tangent line of $h(x)$ at $x = w_1$. The slope of the tangent line is given by $h'(w_1) = -\sqrt{2R(h_{\text{cen}})}$. The estimate of w_2 , the distance in x for $h(x)$ to decay from h_{cen} to h_{\min} computed using the tangent line at $x = w_1$ is thus given by

$$w_2 = \frac{h_{\text{cen}} - h_{\min}}{\sqrt{2R(h_{\text{cen}})}} \quad (3.38)$$

We measure the width w of small droplets by $w = w_1 + w_2$, i.e.

$$w(p) = \int_{h_{\text{cen}}}^{h_{\max}} \frac{1}{\sqrt{2R(h)}} dh + \frac{h_{\text{cen}} - h_{\min}}{\sqrt{2R(h_{\text{cen}})}} \quad (3.39)$$

Substituting $\tilde{R}(h)$ for $R(h)$ in $w(p)$ gives

$$w \sim \frac{\sqrt{2}}{a\sqrt{h_{\max} - h_{\min}}} \text{arctanh} \left(\sqrt{1 - \frac{h_{\text{cen}} - h_{\min}}{h_{\max} - h_{\min}}} \right) + \frac{h_{\text{cen}} - h_{\min}}{\sqrt{2R(h_{\text{cen}})}} \quad (3.40)$$

Homoclinic solutions have a tail that extends to $\pm\infty$. Numerically, we could estimate the width of the droplet by introducing a small cut-off parameter δ and integrating (3.36) from $h_{\min} + \delta$ to h_{\max} , i.e.

$$w = \int_{h_{\min} + \delta}^{h_{\max}} \frac{1}{\sqrt{2R(h)}} dh \quad (3.41)$$

Figure 3.5 (a) shows the droplet width vs. droplet pressure computed for large droplets. The solid blue curve denotes the width estimate calculated by (3.41) for $\delta = 10^{-3}$, $\epsilon = 0.1$. The dotted black curve denotes the width estimate given by (3.26). Figure 3.5 (b) shows the droplet width vs. droplet pressure computed for small droplets. The solid blue curve denotes the width calculated using (3.41) for $\delta = 10^{-3}$, $\epsilon = 0.1$. The cross-dotted curve denotes the width estimate calculated by (3.40). The square-dotted curve denotes the estimate given by (3.26). Since small droplets are characterized by longer tails, the width approximation given by (3.26) underestimates the true width of small droplets. The numerical simulation results suggest that as $\bar{p} \rightarrow p_{\max}$, (3.40) produces a better width estimate for small droplets.

3.2 Steady-state axisymmetric solutions

If we assume the film on a 2-D domain to be axisymmetric around a point, the thickness of the axisymmetric film $h(r, t)$ on $r \in [0, L]$, subject to no-flux boundary conditions, is described by

$$\frac{\partial h}{\partial t} = \frac{1}{r} \frac{\partial}{\partial r} (rq), \quad q = h^3 \frac{\partial}{\partial r} \left(\Pi(h) - \frac{1}{r} \frac{\partial}{\partial r} \left(r \frac{\partial h}{\partial r} \right) \right) \quad (3.42a)$$

$$\frac{\partial h}{\partial r} (0) = \frac{\partial h}{\partial r} (L) = 0, \quad \lim_{r \rightarrow 0^+} rq(r) = q(L) = 0 \quad (3.42b)$$

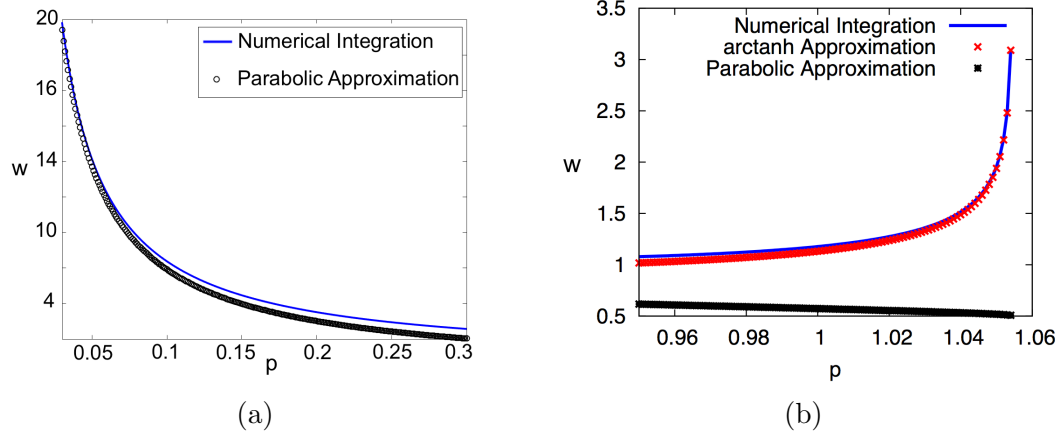


FIGURE 3.5: (a) Droplet width vs. p plotted for large droplets. The solid blue curve denotes the width estimate calculated by (3.41) for $\delta = 10^{-3}$, $\epsilon = 0.1$. The dotted black curve denotes the width estimate given by (3.26). (b) Droplet width vs. p plotted for small droplets. The solid blue curve denotes the width calculated using (3.41) for $\delta = 10^{-3}$, $\epsilon = 0.1$. The cross-dotted curve denotes the width estimate calculated by (3.40). The square-dotted curve denotes the estimate given by (3.26).

Note that $q(r)$ has a singularity at $r = 0$, so the condition $\frac{\partial h}{\partial r}(0) = 0$ is required to ensure regularity of the solution at $r = 0$. The steady-states for this problem can still be parametrized by uniform pressure $p \equiv \bar{p}$. It follows from (3.42a)-(3.42b) that the steady-states for axisymmetric solution are described by

$$\frac{1}{r} \frac{d}{dr} \left(r \frac{dh}{dr} \right) = \Pi(h) - \bar{p} \quad (3.43)$$

Using product rule to expand the derivative and multiplying both sides of (3.43) by r , we have

$$r h'' + h' - r \Pi(h) + \bar{p} r = 0 \quad (3.44a)$$

$$h'(0) = h'(L) = 0 \quad (3.44b)$$

The mass of the axisymmetric solutions $h(r; \bar{p})$ is given by $m = 2\pi \int_0^L h(r; \bar{p}) r dr$.

For simplicity, we omit the factor of 2π in the rest of our studies on axisymmetric

solutions so m is given by

$$m = \int_0^L h(r; \bar{p}) r dr \quad (3.45)$$

In this section, we present asymptotic analysis for steady-state axisymmetric solutions governed by (3.44a)-(3.44b) for $\Pi(h)$ of the form (2.17) in the limit $\epsilon \rightarrow 0$. Note that the ODE given by (3.44a) is no longer autonomous as in the 1-D scenario. For each given \bar{p} , there exists a droplet-type solution with its center and maximum film thickness at $r = 0$ as well as a ring-type solution with its maximum film thickness at $r = L$. In this section, we focus on the former, i.e. the droplet-type solution which is monotonically decreasing on $[0, L]$.

Assume the Hamaker constant $A = 1$. In the limit $\epsilon \rightarrow 0$, in the droplet core, $h = O(1)$ so $\Pi(h) = O(\epsilon^2) \ll 1$. At $O(1)$, (3.44a) can be approximated by

$$r h'' + h' + \bar{p} r = 0 \quad (3.46)$$

The general solution to the ODE (3.46) has the form

$$h(r) = C_1 \ln(r) + C_2 - \frac{1}{4} \bar{p} r^2 \quad (3.47)$$

where C_1 and C_2 are some constants. Applying the boundary conditions $h'(0) = 0$ and $h(0) = h_{\max}$, we have

$$h(r) \sim -\frac{1}{4} \bar{p} r^2 + h_{\max} \quad (3.48)$$

which suggests that in the limit $\epsilon \rightarrow 0$, the leading order profile of a large axisymmetric droplet can still be approximated by a parabola, but with a modified coefficient. Let w denote the width of the droplet, which is the edge of support of the droplet. Then an estimate of w could be obtained accordingly by setting $h(w) \sim 0$, which yields

$$h_{\max} \sim \frac{1}{4} \bar{p} w^2 \quad (3.49)$$

Similar to 1-D steady-state solutions, by multiplying both sides of (3.46) by h' and integrating, we could rewrite (3.46) as a first order ODE given by

$$\frac{1}{2}h'(r)^2 - U(h) + \bar{p}h + U(h_{\max}) - \bar{p}h_{\max} = - \int_0^r \frac{h'(z)^2}{z} dz \quad (3.50)$$

where we used the boundary conditions $h(0) = h_{\max}$, $h'(0) = 0$. Note that the integral $\int_0^r \frac{h'(z)^2}{z} dz$ is not singular for $z \rightarrow 0$ because in the droplet core, $\frac{h'(r)^2}{r} \sim \frac{1}{4}\bar{p}^2 r$. Next, we apply the boundary conditions $h(L) = h_{\min}$, $h'(L) = 0$ to (3.50), yielding

$$-U(h_{\min}) + \bar{p}h_{\min} + U(h_{\max}) - \bar{p}h_{\max} = - \int_0^L \frac{h'(r)^2}{r} dr \quad (3.51)$$

at $r = L$. In the droplet core, $h_{\max} = O(1)$. In the outer region, for $r \gg w$, $h'(r) \sim 0$ and $h''(r) \sim 0$. It follows that $\int_0^L \frac{h'(r)^2}{r} dr \sim \int_0^w \frac{h'(r)^2}{r} dr$. By (3.44a), in the outer region, $\Pi(h_{\min}) = \bar{p}$ at leading order, so $h_{\min} \sim \epsilon$. Hence, as $\epsilon \rightarrow 0$, at $O(1)$, (3.51) is given by

$$-U(\epsilon) - \bar{p}h_{\max} = - \int_0^w \frac{h'(r)^2}{r} dr \quad (3.52)$$

Substituting the leading order asymptotic prediction of the droplet core given by (3.48) and (3.49) into (3.52), we obtain the leading order asymptotic prediction for h_{\max} and w in the limit $\epsilon \rightarrow 0$, which is given by

$$h_{\max} \sim -\frac{2U(\epsilon)}{\bar{p}}, \quad (3.53a)$$

$$w \sim \frac{2}{\sqrt{3\bar{p}}}. \quad (3.53b)$$

To derive the equilibrium contact angle of axisymmetric droplets in the limit $\epsilon \rightarrow 0$, we use a similar argument as illustrated in (3.27)-(3.29) for 1-D solutions. In the contact line region, we rescale the solution by writing $h(r) = \epsilon H(Z)$ for $Z = \frac{w-r}{\epsilon}$ so at leading order, (3.50) reduces to

$$\frac{1}{2}H'(Z)^2 = U(\epsilon H) + \frac{1}{2}\bar{p}h_{\max} = U(\epsilon H) - U(\epsilon) \quad (3.54)$$

As $Z \rightarrow -\infty$, $H \rightarrow 1$ and $H'(Z) \rightarrow 0$. As $Z \rightarrow \infty$, $U(\epsilon H)$ is negligible, so we have

$$H'(Z) = \frac{1}{\sqrt{3}} \quad (3.55)$$

which shows that the equilibrium contact angle of the axisymmetric droplets is the same as that of the 1-D droplets.

3.3 Stability and bifurcation

3.3.1 Bifurcation of 1-D solutions

In this section, we study the bifurcation of 1-D steady-state solutions on $x \in [0, L]$ by investigating the stability of various steady-states that could exist on $[0, L]$. Specifically, we focus on droplet-type solutions that are monotonically decreasing on $[0, L]$. Each of these solutions is also the right half of a full droplet with period $2L$ that can be extended periodically outside of $[-L, L]$. To determine the stability of these steady-state droplets, we use linear stability analysis. We write $h(x, t) = \bar{h}(x, \bar{p}) + \sigma h_1(x, t)$ for $\sigma \ll 1$ to represent a solution slightly perturbed from the steady-state $\bar{h}(x, \bar{p})$. Substituting $h(x, t) = \bar{h}(x, \bar{p}) + \sigma h_1(x, t)$ into the evolution equation subject to no-flux boundary conditions and neglecting terms of $O(\sigma^2)$, we obtain a linear PDE problem for $h_1(x, t)$ given by

$$\frac{\partial h_1}{\partial t} = \mathcal{L}h_1 \quad (3.56a)$$

$$h_{1x}(0) = h_{1x}(L) = 0, \quad h_{1xxx}(0) = h_{1xxx}(L) = 0 \quad (3.56b)$$

where \mathcal{L} is a linear operator defined by

$$\mathcal{L}g = \frac{\partial}{\partial x} \left(\bar{h}^3 \frac{\partial}{\partial x} \left(\Pi'(\bar{h})g - \frac{\partial^2 g}{\partial x^2} \right) \right) \quad (3.57)$$

The adjoint of \mathcal{L} is given by

$$\mathcal{L}^*g = \left(\Pi'(\bar{h}) - \frac{\partial^2}{\partial x^2} \right) \left(\frac{\partial}{\partial x} \left(\bar{h}^3 \frac{\partial g}{\partial x} \right) \right) \quad (3.58)$$

Using separation of variables, we could write the solution $h_1(x, t)$ as

$$h_1(x, t) = \sum_n c_n e^{\lambda_n t} f_n(x) \quad (3.59)$$

where λ_n is the eigenvalue of the fourth order differential operator \mathcal{L} , $f_n(x)$ is the corresponding eigenfunction and $c_n = \int_0^L h_1(x, 0) q_n(x) dx$ for q_n such that $\mathcal{L}^* q_n = \overline{\lambda_n} q_n$.

Analyzing the stability of various steady-state solutions amounts to solving the eigenvalue problem $\mathcal{L}f = \lambda f$. First, we start by analyzing the stability of flat film solutions $\bar{h}(x) \equiv \bar{h}$. In this case, the eigenvalue problem $\mathcal{L}f = \lambda f$ reduces to a fourth order linear constant coefficient ODE given by

$$\Pi'(\bar{h})f_{xx} - f_{xxxx} = \tilde{\lambda}f \quad (3.60)$$

$$f_x(0) = f_x(L) = 0, \quad f_{xxx}(0) = f_{xxx}(L) = 0 \quad (3.61)$$

where $\tilde{\lambda} = \frac{\lambda}{\bar{h}^3}$. Substituting $f(x) = \cos\left(\frac{n\pi x}{L}\right)$ into the ODE yields

$$\lambda_n = \bar{h}^3 \left(-\frac{n^4 \pi^4}{L^4} - \frac{n^2 \pi^2}{L^2} \Pi'(\bar{h}) \right) \quad (3.62)$$

for $n = 0, \pm 1, \pm 2, \dots$. From (3.62), we know that if $\Pi'(\bar{h}) > -\frac{n^2\pi^2}{L^2}$, then $\lambda_n \leq 0$.

If $\Pi'(\bar{h}) < -\frac{n^2\pi^2}{L^2}$, then $\lambda_n \geq 0$, which makes the trivial steady-state unstable. For

$\bar{h} < \frac{4}{3}\epsilon$, $\Pi'(\bar{h}) > 0$ so \bar{h} is stable. For $h > \frac{4}{3}\epsilon$, $\Pi'(h) < 0$ and has a minimum at $h = \frac{5}{3}\epsilon$. If $L < \frac{\pi}{\sqrt{|\Pi'(\frac{5}{3}\epsilon)|}}$, then $\Pi'\left(\frac{5}{3}\epsilon\right) > -\frac{\pi^2}{L^2}$ and $\lambda_n < 0$ for all $n \geq 1$.

This suggests that for sufficiently small domain L , all eigenmodes are stable. For

$L > \frac{\pi}{\sqrt{|\Pi'(\frac{5}{3}\epsilon)|}}$, there exists a range (h_a, h_b) such that for $h_a < \bar{h} < h_b$, $\Pi'(\bar{h}) < -\frac{\pi^2}{L^2}$

and $\lambda_1 > 0$ where h_a and h_b are the positive roots of $\Pi'(h) = -\frac{\pi^2}{L^2}$. For large domain

$L \rightarrow \infty$, $h_a \rightarrow \frac{4}{3}\epsilon$ and $h_b \rightarrow \left(\frac{3\epsilon^2 L^2}{\pi^2}\right)^{\frac{1}{4}}$. This suggests that if we fix $L > \frac{\pi}{\sqrt{|\Pi'(\frac{5}{3}\epsilon)|}}$,

then for extremely small and large film mass, the solution is stable. There exists an intermediate film thickness range $h_a < \bar{h} < h_b$ such that the solution is unstable.

Our goal is to study the stability of a nontrivial solution with pressure $p \equiv \bar{p}$ and period $2L$. To calculate the eigenvalues of $\mathcal{L}f = \lambda f$ for a nontrivial steady-state droplet $\bar{h}(x, \bar{p})$ numerically, we discretize the linear operator \mathcal{L} using a second order central finite difference method, which leads to the eigenvalue problem for a penta-diagonal matrix A . We use MATLAB's built-in eigenvalue solver to find the eigenvalues of A . To validate the numerical computation results given by MATLAB, we first compare the numerical results with the analytical results for flat film solutions. The exact eigenvalues of flat film solutions are given by (3.62). Let $\text{Re}(\lambda)$ denote the real part of an eigenvalue λ . Figure 3.6 shows $\max_n \text{Re}(\lambda_n)$ vs. p computed for flat film solutions numerically in MATLAB and analytically using (3.62). The numerical simulation results in Figure 3.6 suggest that the eigenvalues calculated by

MATLAB agree very well with the exact eigenvalues for flat films.

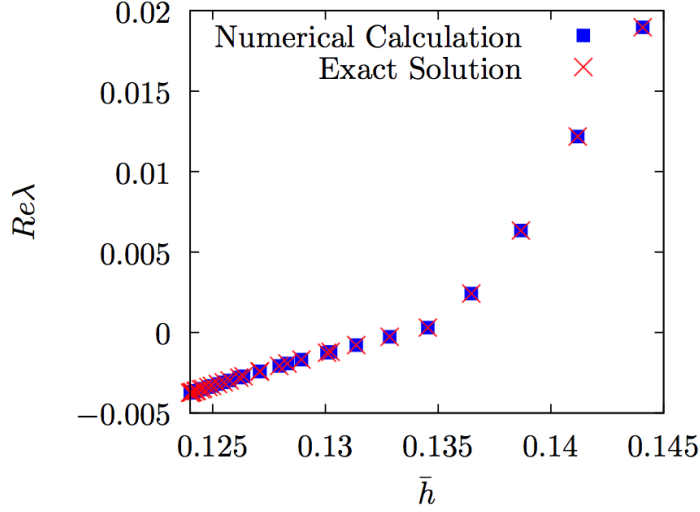


FIGURE 3.6: Largest nonzero $Re(\lambda)$ computed numerically in MATLAB and analytically using (3.62). $L = 3.5$.

Next, we validate MATLAB's eigenvalue calculation for nontrivial steady-states $\bar{h}(x)$. To this end, we initialize the full evolution PDE by $h(x, 0) = \bar{h}(x) + \delta g_1(x)$ where $g_1(x)$ is the normalized eigenfunction in L_2 norm that corresponds to the most unstable eigenmode. $\delta \ll 1$ is a small positive parameter. Let λ_1 denote the most unstable eigenvalue. If we evolve the PDE forward in time, then for short time, we expect $\|h(x, t) - \bar{h}(x)\|_2 \sim \delta e^{\lambda_1 t}$. Therefore, we compare $\|h(x, t) - \bar{h}(x)\|_2$ computed numerically from the time-dependent PDE with $\delta e^{\lambda_1 t}$ for λ_1 computed using the eigenvalue solver in MATLAB. Figure 3.7 shows the rate at which $h(x, t)$ moves away from $\bar{h}(x)$ plotted in semi-log scale for short time. This further confirms the numerical accuracy of the eigenvalue calculations for nontrivial steady-states in MATLAB. In all of our calculations, all eigenvalues are real with no imaginary part.

Now we employ MATLAB's eigenvalue solvers to investigate the stability of steady-states on $[0, L]$. First, we fix L and study the stability of solutions as the

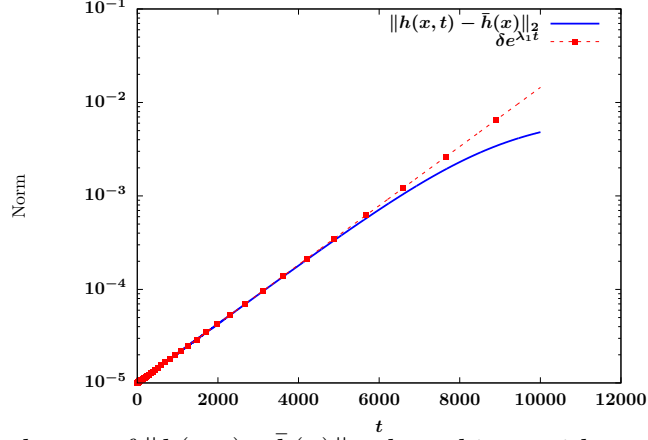


FIGURE 3.7: Growth rate of $\|h(x, t) - \bar{h}(x)\|_2$ plotted in semi-log scale for short time. Results of time-dependent PDE simulations compared with eigenvalue predictions with parameter values $L = 5, \bar{p} = 0.92, \delta = 10^{-5}$.

droplet pressure p changes. As we vary the pressure \bar{p} , the droplet mass m changes. For a fixed L , for extremely large mass, there is no droplet-type solution. Only trivial flat film solutions $\bar{h}(x) \equiv \bar{h}$ exist. Figure 3.8 (a) shows the mass m vs. pressure p of droplets with $L = 2.5$ for large m . Figure 3.8 (b) shows the eigenvalue computed by continuation in droplet mass. Figure 3.8 (c) shows the eigenvalue plotted against the droplet pressure as the droplet mass changes. In Figure 3.8 (a)-(c), The blue solid curve represents nontrivial steady-states. The red curve represents flat film solutions. As can be observed from Figure 3.8 (a), as film mass decreases from large mass, nontrivial steady-states first start to exist as the mass passes through some critical $m = m_a$. Besides m_a , there also exists a mass $m_b < m_a$ such that for $m \in (m_b, m_a)$, there exist two distinct steady-state solutions both with mass m . The eigenvalue computation results in Figure 3.8 (b) show that one of these two steady-states is stable and the other one is unstable. Figure 3.8 (c) shows that of the two steady-state droplets with $m \in (m_b, m_a)$, the solution with smaller pressure is unstable. The solution with larger pressure is stable. The eigenvalue results in Figure 3.8 (b) also show that the flat film solution has a stability change at $m = m_b$. For $m > m_b$, flat film is stable. As m passes through m_b , flat film becomes unstable.

Note that m_b is also the mass at which nontrivial solutions start to bifurcate from trivial solutions, as shown in Figure 3.8 (a). The unstable solutions cease to exist for $m < m_b$.

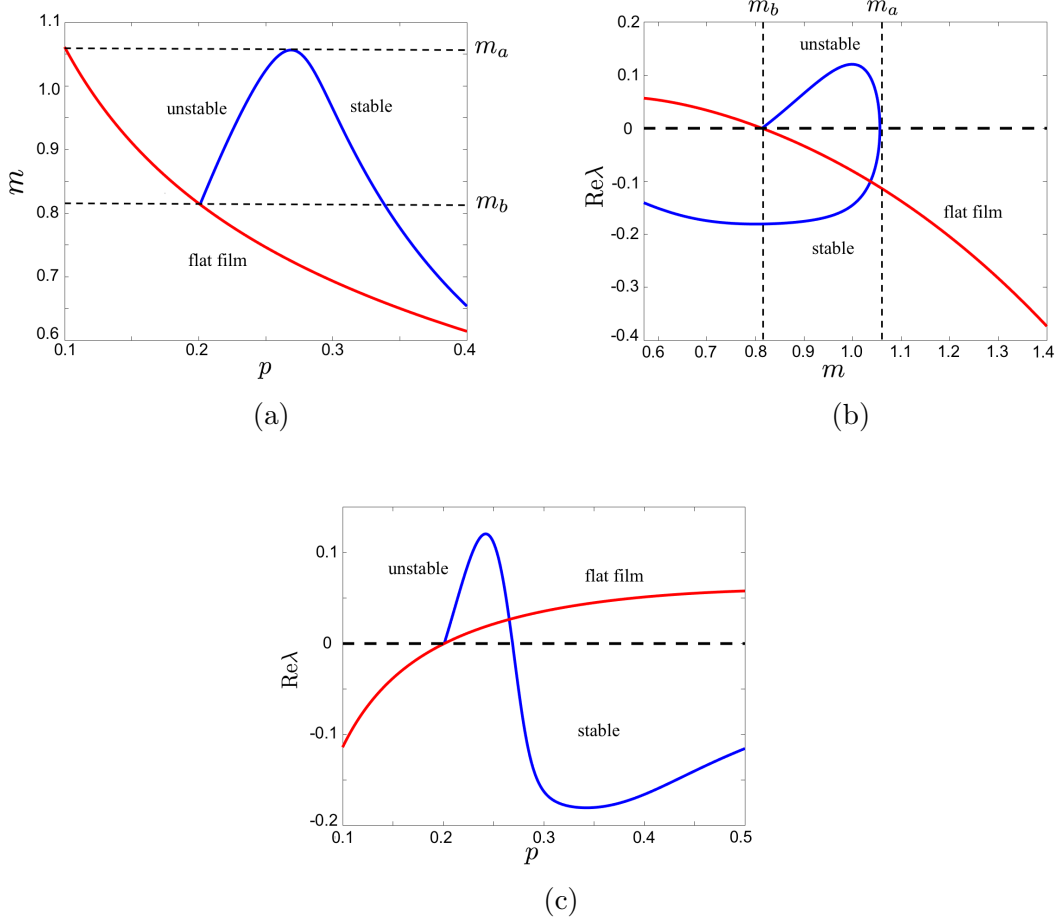


FIGURE 3.8: (a) Mass m vs. pressure p of droplets of large mass. (b) Plot of $\max_n \text{Re}(\lambda_n)$ vs. mass m for large-mass droplets. (c) Plot of $\max_n \text{Re} \lambda_n$ vs. droplet pressure p for large-mass droplets. In (a)-(c), $L = 2.5$.

When $m < m_b$, as m continues to decrease, only the branch of stable droplets discussed above remains to exist. As m decreases, the pressure of this branch of stable solutions increases, as shown in Figure 3.8 (a). This branch of solutions remains stable until \bar{p} approaches p_{\max} . Figure 3.9 (a) shows mass m vs. pressure \bar{p} for \bar{p} near p_{\max} for $L = 2.5$. We found that there exists another mass interval (m_d, m_c)

such that for $m \in (m_d, m_c)$, there are two distinct nontrivial steady-states both with mass m . Compared to (m_b, m_a) , the mass in the range (m_d, m_c) is smaller in value. The corresponding droplet pressure is larger. Figure 3.9 (b) shows the eigenvalue $\max_n \text{Re}(\lambda_n)$ computed for each steady-state for a range of film mass m . The eigenvalue results suggest that the two nontrivial steady-states with $m \in (m_d, m_c)$ have different stability. Figure 3.9 (c) shows the plot of eigenvalue $\max_n \text{Re}(\lambda_n)$ for a range of droplet pressure p . This figure suggests that of the two nontrivial solutions with the same mass $m \in (m_d, m_c)$, the solution with smaller p is stable. The solution with larger p is unstable. In Figure 3.9 (a)-(c), the blue solid curve represents the nontrivial solutions. The red curve represents the trivial flat film solutions. We also observe that at $m = m_c$, the flat film solution has a stability change. For $m \in (m_c, m_b)$, the flat film solutions are stable. As m falls below $m = m_c$, the flat film solutions lose stability to become unstable.

As illustrated above, if we fix period $L = 2.5$, then we observe two mass ranges, (m_b, m_a) and (m_d, m_c) such that for any m in these two mass intervals, there are two distinct steady-states with mass m . One of the steady-states is stable, while the other steady-state is unstable. The co-existence of two solutions and their difference in stability can also be observed in the bifurcation diagram for m vs. h_{\min}, h_{\max} . Figure 3.10 (a) and (b) show the change in droplet size, represented by mass m vs. h_{\max}, h_{\min} . Figure 3.10 (a) zooms into a range of small mass, near (m_d, m_c) . Figure 3.10 (b) zooms into a range of large mass, near (m_b, m_a) . In both cases, when two different nontrivial steady-states with the same mass co-exist, the larger-amplitude solution is always stable. The smaller-amplitude solution is always unstable.

Next, we study the stability of steady-state solutions by fixing $p \equiv \bar{p}$ and varying L . We fix the pressure to be some \bar{p} near p_{\max} and increase L . Figure 3.12 (a) shows

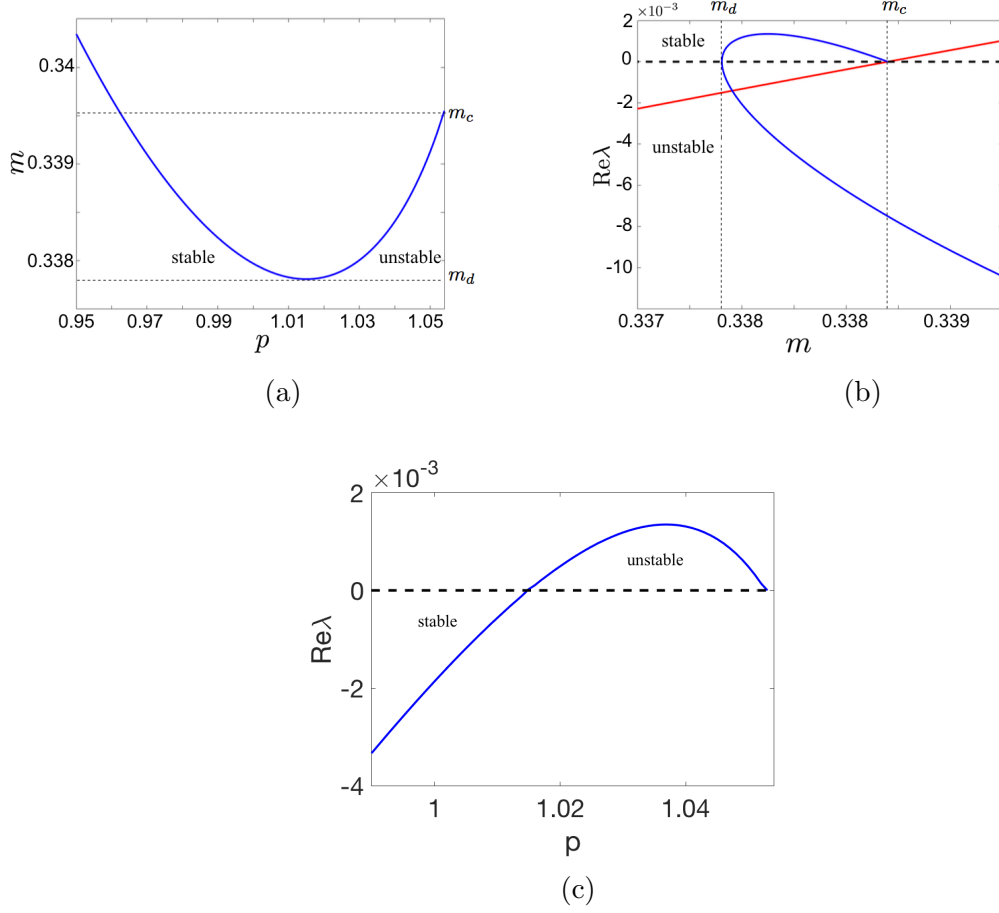


FIGURE 3.9: (a) Droplet mass m vs. droplet pressure p for p near p_{\max} . (b) Plot of $\max_n \operatorname{Re}(\lambda_n)$ vs. droplet mass m . (c) Plot of eigenvalue $\max_n \operatorname{Re}(\lambda_n)$ vs. droplet pressure p . $L = 2.5$.

$\max_n \operatorname{Re} \lambda_n$ of the steady-state solution with pressure $\bar{p} = 1$ on $[0, L]$ as L increases. We observe that $\max_n \operatorname{Re}(\lambda_n)$ changes from negative to positive at some p^* near p_{\max} , implying that the steady-state solution with $\bar{p} = 1$ loses stability as L increases. Figure 3.12 (b) shows the plot of $\max_n \operatorname{Re}(\lambda_n)$ vs. m for steady-state droplet with $\bar{p} = 1$. If we fix \bar{p} , as L increases, the droplet mass also increases. It follows that there also exists a critical m^* at which the solution changes stability. The simulation results in Figure 3.12 (a)-(b) suggest that the stability of small-mass droplets has a dependence on L . Specifically, increasingly L has the effect of destabilizing small

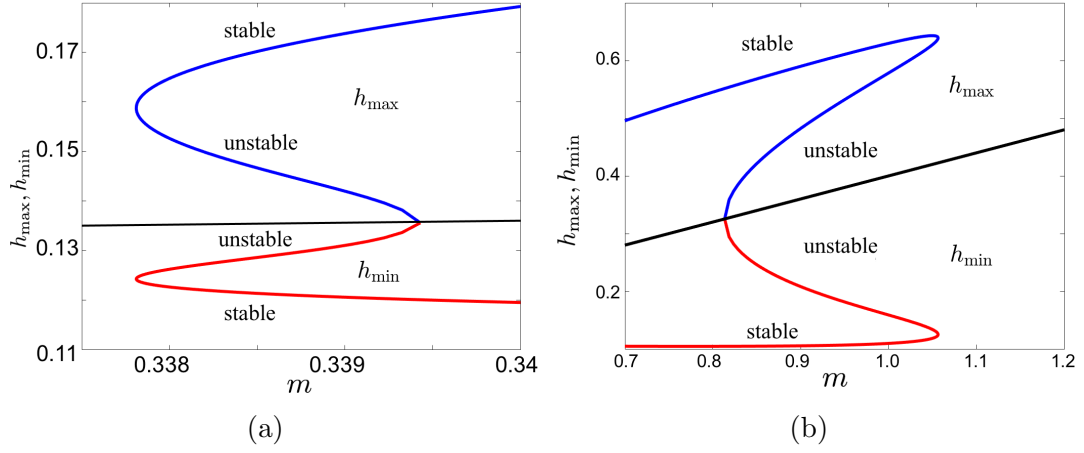


FIGURE 3.10: (a) Plot of m vs. h_{\max}, h_{\min} for small m (b) Plot of m vs. h_{\max}, h_{\min} for large m . In (a)-(c), $L = 2.5$.

mass droplets.

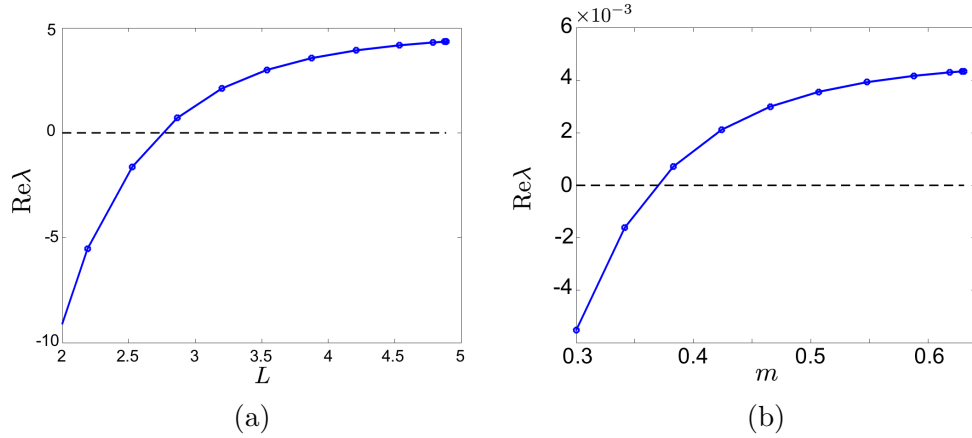


FIGURE 3.11: (a) $\max_n \text{Re} \lambda_n$ vs. L (b) $\max_n \text{Re} \lambda_n$ vs. mass m . In (a)-(b), pressure $\bar{p} = 1$ is fixed.

To further illustrate this destabilizing effect, we compare the stability of the continuous family of nontrivial steady-state solutions that could exist on $[0, L]$ for $L = 1.5$ and $L = 2.5$. Figure 3.12 (a) shows $\max_n \text{Re}(\lambda_n)$ vs. p computed for the continuous family of nontrivial steady-states on $[0, L]$ for both $L = 1.5$ and $L = 2.5$.

From the figure, we observe that for both $L = 1.5$ and $L = 2.5$, there exists a range of small pressure such that the steady-state is unstable. This corresponds to the branch of unstable solutions with mass $m \in (m_b, m_a)$ as discussed above. Figure 3.12 (b) shows the same plot zoomed into \bar{p} near p_{\max} . As $\bar{p} \rightarrow p_{\max}$, for $L = 1.5$, all of the eigenvalues have negative real part, suggesting that the branch of stable solutions that arises from $m = m_b$ remains stable as $\bar{p} \rightarrow p_{\max}$. For this branch of solutions, as \bar{p} increases, the droplet mass m decreases. The results in Figure 3.12 (b) suggest that for $L = 2.5$, however, we observe a critical p^* such that for $\bar{p} > p^*$, the nontrivial steady-states change from being stable to unstable. This corresponds to the unstable solution in the mass range (m_d, m_c) as discussed above. For $L = 2.5$, droplets are unstable in the limit of small mass.

The difference in stability of small droplets between $L = 1.5$ and $L = 2.5$ can be further illustrated by the change in structure of the bifurcation diagram for m vs. h_{\max}, h_{\min} for these two L values. Figure 3.13 (a) and (b) show the plot of m vs. h_{\max}, h_{\min} for a continuous family of solutions for $L = 1.5$ and $L = 2.5$ respectively. Figure 3.13 (c)-(d) show exactly the same plot zoomed into small mass for $L = 1.5$ and $L = 2.5$, which highlights the difference in the structure of the bifurcation curve for films with small mass. In both figures, nontrivial solution bifurcates from flat film. This bifurcation is a pitchfork bifurcation, which has been previously studied [7]. Specifically, Bertozzi et al. studied the local structure of the bifurcation of steady-states on a fixed domain $[0, 1]$ with varying droplet mass [7]. All branches of nontrivial steady-states including those that characterize more than one droplet in the domain were considered. By using perturbation methods, they developed an asymptotic approximation for the local structure of the bifurcation, showing that near the k th bifurcation point \bar{u}_k , the structure is given by

$$(u(0) - \bar{u}_k)^2 = \frac{24k^2\pi^2\Pi''(\bar{u}_k)}{\Pi''(\bar{u}_k)^2 - 3k^2\pi^2\Pi'''(\bar{u}_k)}(\bar{u} - \bar{u}_k) \quad (3.63)$$

for $\bar{u} = \int_0^1 u(x)dx$ where $u(x)$ denotes the thin film profile. From the analysis, they determined that the pitchfork could be either supercritical or subcritical [7]. The bifurcation at the k th bifurcation point on a fixed domain for different k is related to the bifurcation of one fixed branch of solutions on $[0, L]$ with different L . As can be observed from Figure 3.13 (c), for $L = 1.5$, nontrivial solution bifurcates from flat film at a supercritical pitchfork bifurcation. In Figure 3.13 (d), for $L = 2.5$, nontrivial solution bifurcates from the trivial branch at $m = m_c$, a subcritical pitchfork bifurcation, which leads to unstable nontrivial steady-states near the bifurcation point. The increase in L leads to a change in structure of the local bifurcation of small-mass films, which ultimately results in the destabilization of some small-mass droplets.

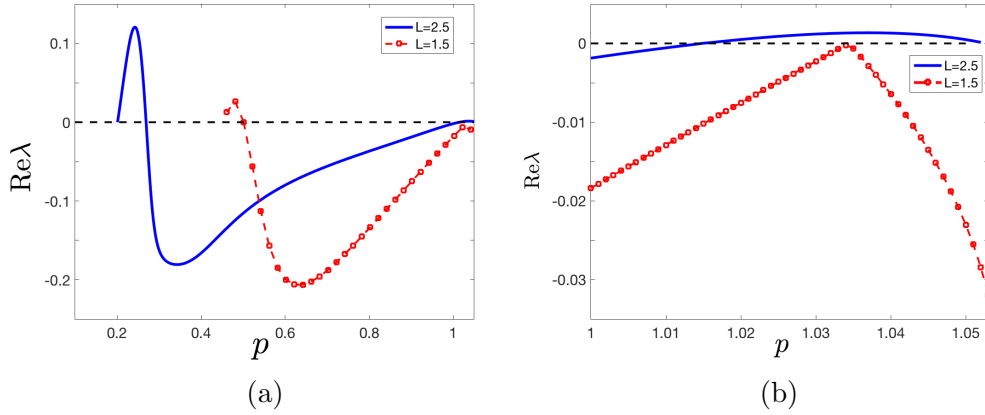


FIGURE 3.12: $\max_n \text{Re} \lambda_n$ vs. p for (a) $L = 1.5$ (b) $L = 2.5$

3.3.2 Bifurcation of axisymmetric solutions

In this section, we study the bifurcation of steady-state axisymmetric thin films. An asymptotic analysis of the local bifurcation structure of axisymmetric solutions on $[0, 1]$ has been previously presented by Witelski and Bernoff [71]. They considered a disjoining pressure of the form $\Pi(h) = \frac{1}{3h^3}$. By writing out the solution near the

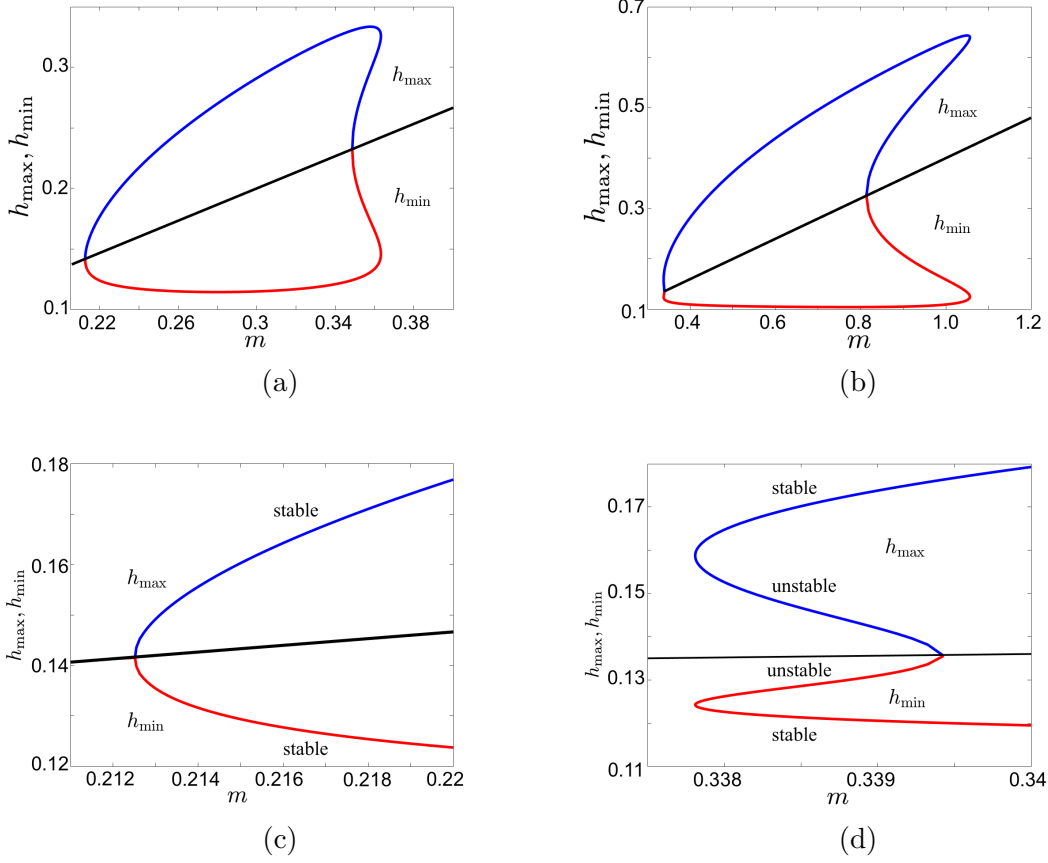


FIGURE 3.13: m vs. h_{\min}, h_{\max} for (a) $L = 1.5$ (b) $L = 2.5$ (c) $L = 1.5$ zoomed into the bifurcation for small mass film (d) $L = 2.5$ zoomed into the bifurcation for small mass films.

bifurcation point as a perturbation expansion, they showed that the bifurcation near the primary bifurcation point $k = 1$ is a transverse bifurcation given by

$$h(0) = \bar{h}_1 + C_1(\bar{h} - \bar{h}_1) \quad (3.64)$$

where \bar{h}_1 is the film mass at the primary bifurcation point $k = 1$, $\bar{h} = \frac{1}{2} \int_0^1 h(r) r dr$

and $C_1 = 1 - 2 \frac{\int_0^1 J_0^2(\Lambda_1 r) r dr}{\int_0^1 J_0^3(\Lambda_1 r) r dr} \approx -4.6773$. $J_0(r)$ denotes Bessel function of the first

kind. Note that the leading order approximation given in (3.64) is independent of the disjoining pressure $\Pi(h)$. In this section, we expand their work by considering a

higher-order description of the bifurcation of steady-states on $[0, L]$. We still focus on the primary bifurcation point $k = 1$. We show that the higher-order term depends on both the form of disjoining pressure and the domain length L . The higher-order term derived reflects the local concavity of the bifurcation and the change in bifurcation structure as the form of $\Pi(h)$ and L vary.

We consider the steady-state axisymmetric problem given by (3.44a)-(3.44b), i.e.

$$rh'' + h' - r\Pi(h) + \bar{p}r = 0 \quad (3.65a)$$

$$h'(0) = h'(L) = 0 \quad (3.65b)$$

where $\Pi(h) = \frac{\epsilon^2}{h^3} - \frac{\epsilon^3}{h^4}$. To derive a local approximation of the bifurcation near h_1 , we write the nontrivial steady-state solution near the bifurcation point \bar{h} as $h(r) = \bar{h} + \delta h_1(r) + \delta^2 h_2(r)$, $m = \bar{m} + \delta$, $p = p_0 + \delta p_1 + \delta^2 p_2$ where m is the mass of the nontrivial steady-state solution near the flat film $h(x) \equiv \bar{h}$, $\bar{m} = \frac{1}{2}\bar{h}L^2$ is the mass of the flat film $h(x) \equiv \bar{h}$ and $p_0 = \Pi(\bar{h})$ is the pressure of the flat film. Substituting the asymptotic expansion into (3.65a) and linearizing, at $O(\delta)$, we obtain

$$rh_1'' + h_1' + a^2 r h_1 = -p_1 r \quad (3.66a)$$

$$h_1'(0) = h_1'(L) = 0 \quad (3.66b)$$

where $a = \sqrt{-\Pi'(\bar{h})}$. The bifurcation occurs at \bar{h} when $aL = \Lambda_n$ for $J_1(\Lambda_k) = 0$ with $k = 1, 2, 3, \dots$. We focus on the thin film solution with no interior extremum, i.e. the primary bifurcation point $k = 1$. The branch of solutions that bifurcates from this point is given by $h_1(r) = \tilde{h}_1(ar)$ where

$$\tilde{h}_1(r) = C J_0(r) + \frac{p_1}{\Pi'(\bar{h})} \quad (3.67)$$

for \bar{h} such that $\sqrt{-\Pi'(\bar{h})}L = aL = \Lambda_1$ with $\Lambda_1 \approx 3.8317$ and some constant C to be determined by the solvability condition.

Applying the mass condition $m = \bar{m} + \delta$, i.e. $\int_0^L h(r)rdr = \bar{m} + \delta \int_0^L h_1(r)rdr$, we obtain

$$\int_0^L h_1(r)rdr = 1 \quad (3.68)$$

Since $\int_0^L J_0(ar)rdr = \int_0^{\Lambda_1} J_0(z)zdz = 0$, (3.68) reduces to

$$\frac{p_1}{\Pi'(\bar{h})} = \frac{2}{L^2} \quad (3.69)$$

At $O(\delta^2)$, (3.65a) is given by

$$rh_2'' + h_2' + a^2rh_2 = \frac{1}{2}\Pi''(\bar{h})h_1^2r - p_2r \quad (3.70a)$$

$$h_2'(0) = h_2'(L) = 0 \quad (3.70b)$$

Let \mathcal{T} be a linear operator defined by $\mathcal{T}g = x\frac{d^2g}{dx^2} + \frac{dg}{dx} + a^2xg$. Then (3.70a) can be written as $\mathcal{T}h_2 = \frac{1}{2}\Pi''(\bar{h})h_1(r)^2r - p_2r$. Subject to the boundary conditions (3.70b), \mathcal{T} is self-adjoint. The nullspace of \mathcal{T} is spanned by $J_0(ar)$. If we apply the solvability condition given by Fredholm alternative to (3.70a), we obtain

$$\int_0^L h_1(r)^2rJ_0(ar)dr = 0 \quad (3.71)$$

This determines the coefficient C in (3.67). The coefficient C in $h_1(r)$ is therefore given by

$$C = \tilde{C} \frac{p_1}{\Pi'(\bar{h})} = \frac{2\tilde{C}}{L^2} \quad (3.72)$$

where

$$\tilde{C} = -2 \frac{\int_0^L J_0(ar)^2 r dr}{\int_0^L J_0(ar)^3 r dr} = -2 \frac{\int_0^{\Lambda_1} J_0(u)^2 u du}{\int_0^{\Lambda_1} J_0(u)^3 u du} \approx -5.6773 \quad (3.73)$$

Hence, the nontrivial solution with mass $m = \bar{m} + \delta$ can be approximated by

$$h(r) \sim \bar{h} + \delta \left[\frac{2}{L^2} \left(\tilde{C} J_0 \left(\frac{\Lambda_1}{L} r \right) + 1 \right) \right] \quad (3.74)$$

If we describe the bifurcation using $h(0)$ and m , we have

$$h(0) \sim \bar{h} + \frac{2(\tilde{C} + 1)}{L^2} (m - \bar{m}) \quad (3.75)$$

If we substitute $\bar{m} = \frac{1}{2} \bar{h} L^2$ in (3.75) and let $L = 1$, we recover (3.64), the leading order approximation of the bifurcation structure derived by Witelski and Bernoff. Similarly, to leading order, $h(L)$ is given by

$$h(L) \sim \bar{h} + \frac{2(\tilde{C} J_0(\Lambda_1) + 1)}{L^2} (m - \bar{m}) \quad (3.76)$$

If we focus on the primary branch $k = 1$, which characterizes solutions with no interior extremum and describes a single droplet on the domain $0 \leq r \leq L$, $h(0)$ and $h(L)$ correspond to the maximum and minimum of the droplet respectively.

We consider disjoining pressure function given by $\Pi(h) = \frac{\epsilon^2}{h^3} - \frac{\epsilon^3}{h^4}$. For this disjoining pressure, $\Pi'(h) < 0$ for all $h > \frac{4}{3}\epsilon$ and $\Pi'(h)$ has a minimum at $h = \frac{5}{3}\epsilon$.

The bifurcation points occur at \bar{h} when $\Pi'(\bar{h}) = -\frac{\Lambda_k^2}{L^2}$. For the primary branch

$k = 1$, we require $L \geq \frac{\Lambda_1}{\sqrt{-\Pi'(\frac{5}{3}\epsilon)}}$. $L = \frac{\Lambda_1}{\sqrt{-\Pi'(\frac{5}{3}\epsilon)}} \approx 1.374$ is the minimum domain

size that allows for the bifurcation of nontrivial solutions from the trivial branch.

For $L > \frac{\Lambda_1}{\sqrt{-\Pi'(\frac{5}{3}\epsilon)}}$, $\Pi'(\bar{h}) = -\frac{\Lambda_1^2}{L^2}$ has two roots, $\bar{h}^1 < \frac{5}{3}\epsilon$ and $\bar{h}^2 > \frac{5}{3}\epsilon$, which correspond to the two nontrivial steady-states with maximum at $r = 0$ and $r = L$ respectively. (3.75) shows at leading order, the slope of the bifurcation curve at each \bar{h}^i is independent of $\Pi(h)$ and only depends on L .

To estimate the local concavity of the bifurcation curve, we seek for a higher-order asymptotic expansion. At $O(\delta^3)$, (3.44a) is given by

$$rh_3'' + h_3' + a^2rh_3 = r \left[\Pi''(\bar{h})h_1h_2 + \frac{1}{6}\Pi'''(\bar{h})h_1^3 \right] - p_3r \quad (3.77a)$$

$$h_3'(0) = h_3'(L) = 0 \quad (3.77b)$$

where $h_2(r)$ is the solution to (3.70a). Specifically, $h_2(r)$ is given by

$$h_2(r) = DJ_0(ar) + q(r) + \frac{p_2}{\Pi'(\bar{h})} \quad (3.78)$$

where D is a constant and $q(r)$ is the particular solution to $rh_2'' + h_2' + a^2rh_2 = \frac{1}{2}\Pi''(\bar{h})h_1^2r$. Applying the solvability condition given by Fredholm alternative like (3.71) determines the coefficient D , yielding

$$D = \frac{-\frac{1}{6}\frac{\Pi'''(\bar{h})}{\Pi''(\bar{h})}\int_0^{\Lambda_1}\tilde{h}_1(u)^3J_0(u)udu - \int_0^{\Lambda_1}\tilde{h}_1(u)q(u)J_0(u)rdr - \frac{p_2}{\Pi'(\bar{h})}\int_0^{\Lambda_1}\tilde{h}_1(u)J_0(u)udu}{\int_0^{\Lambda_1}\tilde{h}_1(u)J_0(u)^2udu} \quad (3.79)$$

Applying the mass condition $m = \bar{m} + \delta$, we have

$$0 = \int_0^L h_2(r)rdr = \frac{1}{\Pi'(\bar{h})} \left(\int_0^L -\frac{1}{2}\Pi''(\bar{h})h_1^2rdr + \frac{1}{2}p_2L^2 \right) \quad (3.80)$$

This determines p_2 , which yields

$$p_2 = \frac{\Pi''(\bar{h})}{L^2} \int_0^L h_1^2rdr \quad (3.81)$$

Together, we obtain an asymptotic expansion for $h(0)$ and $h(L)$ near \bar{h} up to $O((m - \bar{m})^2)$, given by

$$h(0) \sim \bar{h} + b_1^0(m - \bar{m}) + b_2^0(m - \bar{m})^2 \quad (3.82)$$

$$h(L) \sim \bar{h} + b_1^L(m - \bar{m}) + b_2^L(m - \bar{m})^2 \quad (3.83)$$

where $b_1^0 = \frac{2(\tilde{A} + 1)}{L^2}$, $b_2^L = D + q(0) + \frac{p_2}{\Pi'(\bar{h})}$, $b_1^L = \frac{2(\tilde{A} + 1)}{L^2}$ and $b_2^L = DJ_0(\Lambda_1) + q(\Lambda_1) + \frac{p_2}{\Pi'(\bar{h})}$. The concavity of $h(0)$ is determined by the sign of $b_2 = D + q(0) + \frac{p_2}{\Pi'(\bar{h})}$. The bifurcation occurs at \bar{h} for $\Pi'(\bar{h}) = -\frac{\Lambda_1^2}{L^2}$. The slope of the bifurcation curve of $h(0)$ vs. \bar{h} is the same for \bar{h}^i for $i = 1, 2$ since $\Pi'(\bar{h}^1) = \Pi'(\bar{h}^2)$. However, because $\Pi''(\bar{h})$ and $\Pi'''(\bar{h})$ are different at \bar{h}^1 and \bar{h}^2 , the concavity of the bifurcation curve $h(0)$ vs. \bar{h} at \bar{h}^1 and \bar{h}^2 are different.

To determine D , we first need to solve for $q(r)$, which is the particular solution to

$$\mathcal{T}h_2 = \frac{1}{2}\Pi''(\bar{h})h_1^2r \quad (3.84)$$

Solution exists by solvability condition imposed by (3.71). Since \mathcal{T} has a nontrivial nullspace spanned by $J_0(ar)$, we find $q(r)$ by constructing a modified Green's function $G(x, x_0)$ [30] which solves

$$\mathcal{L}G(x, x_0) = \delta(x - x_0) + cxJ_0(ax) \quad (3.85)$$

We choose c so that the solvability condition is satisfied, i.e.

$$\int_0^L \left[\delta(x - x_0) + cxJ_0(ax) \right] J_0(ax) dx = 0 \quad (3.86)$$

This gives

$$c = -\frac{J_0(ax_0)}{\int_0^L J_0(ax)^2 x dx} = -\frac{a^2 J_0(ax_0)}{M} \quad (3.87)$$

where $M = \int_0^{\Lambda_1} J_0(u)^2 u du$.

For $x \neq x_0$, $\mathcal{L}G = cxJ_0(ax)$. The particular solution y_p can be found by applying variation of parameters to

$$q''(x) + \frac{1}{x}q(x) + a^2q(x) = J_0(ax) \quad (3.88)$$

The homogeneous solution to (3.88) is spanned by $J_0(ax)$ and $Y_0(ax)$. The Wronskian of the two fundamental solutions is given by

$$W(J_0(ax), Y_0(ax)) = \frac{2}{\pi x} \quad (3.89)$$

By variation of parameters, we have

$$y_p = -J_0(ax) \int \frac{\pi x}{2} Y_0(ax) c J_0(ax) dx + Y_0(ax) \int \frac{\pi x}{2} J_0(ax) c J_0(ax) dx \quad (3.90)$$

After simplification, we obtain

$$y_p = -\frac{aJ_0(ax_0)}{2M} x J_1(ax) \quad (3.91)$$

Note that this particular solution satisfies the boundary condition required at $x = 0$ since $\frac{d}{dx}(xJ_1(ax)) = axJ_0(ax)$. Thus, the modified Green's function $G(x, x_0)$ is given by

$$G(x, x_0) = \begin{cases} c(x_0)J_0(ax) - \frac{aJ_0(ax_0)}{2M_1} x J_1(ax) & x < x_0 \\ d(x_0)Y_0(ax) + e(x_0)J_0(ax) - \frac{aJ_0(ax_0)}{2M} x J_1(ax) & x > x_0 \end{cases} \quad (3.92)$$

for some coefficient $c(x_0)$, $d(x_0)$ and $e(x_0)$ to be determined by the continuity of $G(x, x_0)$, the right boundary condition and the symmetry of $G(x, x_0)$ respectively.

For the boundary condition to hold at $x = L$, we need

$$-aY_1(aL)d(x_0) + \frac{aJ_0(ax_0)}{2M} aLJ_0(aL) = 0 \quad (3.93)$$

which gives $d(x_0) = -\frac{J_0(ax_0)\gamma}{2}$ where $\gamma = \frac{\Lambda_1 J_0(\Lambda_1)}{MY_1(\Lambda_1)}$. In addition, we require continuity of $G(x, x_0)$ at $x = x_0$, which gives $c(x_0) - e(x_0) = -\frac{\gamma}{2}Y_0(ax_0)$. Together, the modified Green's function is given by

$$G(x, x_0) = \begin{cases} -\frac{\gamma}{2}Y_0(ax_0)J_0(ax) - \frac{aJ_0(ax_0)}{2M}xJ_1(ax) + e(x_0)J_0(ax) & x < x_0 \\ -\frac{\gamma}{2}J_0(ax_0)Y_0(ax) - \frac{aJ_0(ax_0)}{2M}xJ_1(ax) + e(x_0)J_0(ax) & x > x_0 \end{cases} \quad (3.94)$$

We choose $e(x_0) = -\frac{ax_0J_1(ax_0)}{2M}$ so that $G(x, x_0)$ is symmetric, i.e. $G(x, x_0) = G(x_0, x)$ as required by theory. Note that the choice of $e(x_0)$ will not change the particular solution $q(x)$ since it will only change the coefficient of $J_0(ax)$, which is the homogeneous solution. Using the modified Green's function constructed above, we can represent $q(x)$ by

$$q(x) = \frac{1}{2}\Pi''(\bar{h}) \int_0^L G(x, s)h_1(s)^2 ds \quad (3.95)$$

We know $h_1(s) = BJ_0(as) + C$ where $B = \frac{2}{L^2}\tilde{A}$ and $C = \frac{2}{L^2}$. This gives

$$q(x) = \frac{1}{2}\Pi''(\bar{h}) \int_0^L G(x, s) \left(BJ_0(as) + C \right)^2 ds \quad (3.96)$$

Ignoring the homogeneous solution in $q(x)$ and using the solvability condition given by (3.71), we can simplify the particular solution to $q(x) = \frac{1}{2}\Pi''(\bar{h})\tilde{q}(x)$ where

$$\tilde{q}(x) = -\frac{\gamma}{2a^2} \left[Y_0(ax) \int_0^{ax} J_0(u) \left(BJ_0(u) + C \right)^2 u du + J_0(ax) \int_{ax}^{\Lambda_1} Y_0(u) \left(BJ_0(u) + C \right)^2 u du \right] \quad (3.97)$$

It follows that at $r = 0$,

$$q(0) = -\frac{\gamma}{4a^2}\Pi''(\bar{h}) \int_0^{\Lambda_1} Y_0(u) \left(BJ_0(u) + C \right)^2 u du \quad (3.98)$$

At $r = L$, we have

$$q(L) = -\frac{\gamma}{4a^2}\Pi''(\bar{h})Y_0(\Lambda_1)\int_0^{\Lambda_1}J_0(u)\left(BJ_0(u)+C\right)^2udu=0 \quad (3.99)$$

by the solvability condition imposed by (3.71). Substituting $q(0)$, $q(L)$ and D into b_2^0 and b_2^L , after simplification, we obtain

$$b_2^0 = c_1^0 \frac{\Pi'''(\bar{h})}{\Pi''(\bar{h})} \frac{1}{L^4} + c_2^0 \frac{\Pi''(\bar{h})}{L^2} \quad (3.100)$$

$$b_2^L = c_1^L \frac{\Pi'''(\bar{h})}{\Pi''(\bar{h})} \frac{1}{L^4} + c_2^L \frac{\Pi''(\bar{h})}{L^2} \quad (3.101)$$

where $c_1^0 \approx -39.1384$, $c_2^0 \approx 0.4525$, $c_1^L \approx 15.7634$, $c_2^L \approx -0.8116$ and \bar{h} is the solution to $\Pi'(\bar{h}) = -\frac{\Lambda_1}{L^2}$.

At \bar{h}^1 , b_2^0 changes from positive to negative at approximately $L \approx 3.2906$; b_2^L changes from negative to positive at approximately $L \approx 1.9486$. At \bar{h}^2 , b_2^0 changes from negative to positive at approximately $L \approx 1.5172$; b_2^L changes from positive to negative at approximately $L \approx 1.4819$. As $L \rightarrow \infty$, $\bar{h}^1 \rightarrow \frac{4}{3}\epsilon$ and $\Pi''(\bar{h}^1) \rightarrow -\frac{729}{1024\epsilon^3}$. At \bar{h}^1 , b_2 is dominated by $c_2 \frac{\Pi''(\bar{h}^1)}{L^2} < 0$ as $L \rightarrow \infty$. Hence, for large L , b_2^0 will remain negative and b_2^L will remain positive. Both b_2^0 and b_2^L approach 0 at a rate proportional to $\frac{1}{L^2}$ at \bar{h}^1 . As $L \rightarrow \infty$, $\bar{h}^2 \rightarrow \infty$, $\Pi''(\bar{h}) \rightarrow 0$ and $\frac{\Pi'''(\bar{h})}{\Pi''(\bar{h})} \rightarrow 0$. As $L \rightarrow \infty$, $\Pi''(\bar{h}^2) \rightarrow 0$ is positive. Hence, b_2^0 is positive and b_2^L is negative. Both b_2^0 and b_2^L approach 0 at a rate proportional to $\frac{\Pi''(\bar{h})}{L^2}$ as $L \rightarrow \infty$. Figure 3.14 (a) and (b) show b_2 computed using (3.100) and (3.101) respectively. The solid blue curve represents b_2 calculated at \bar{h}^1 . The dotted red curve represents b_2 calculated at \bar{h}^2 . The solid black curve represents 0. We observe in the figure that at both

\bar{h}^i , b_2 approaches 0 as $L \rightarrow \infty$. Specifically, b_2 approaches 0 faster at \bar{h}^2 , which is consistent with our analysis above. Figure 3.15 (a) and (b) show the bifurcation

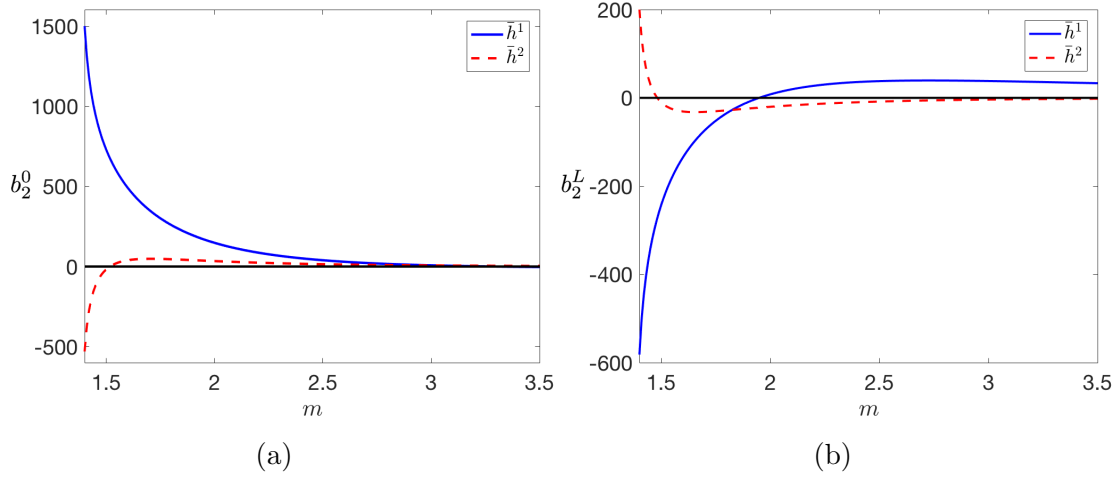


FIGURE 3.14: Concavity b computed at \bar{h}^1 and \bar{h}^2 (a) b_2^0 vs. m (b) b_2^L vs. m

diagram of steady-states for $L = 1.4$ and $L = 3$ respectively. For both $L = 1.4$ and $L = 3$, there exists three distinct types of steady-states, a droplet-type solution with maximum at $r = 0$, a ring-type solution with maximum at $r = L$ and a flat film solution. The solid blue curve represents $h(0)$. The solid red curve represents $h(L)$. The solid black curve is the flat film solution. $h(0) > \frac{2m}{L^2}$ and $h(L) > \frac{2m}{L^2}$ represent the maximum film thickness centered at $r = 0$ and $r = L$ respectively. For $h(0) > h(L)$, the nontrivial solution has a maximum at $r = 0$. The solution has a maximum at $r = L$ otherwise.

Figure 3.16 (a) and (b) show the linear and quadratic approximation of the bifurcation structure for $L = 1.4$ at \bar{h}^1 and \bar{h}^2 respectively. The linear approximation is given by (3.64). The quadratic approximation at \bar{h}^1 and \bar{h}^2 is given by (3.82) and (3.83) respectively. At \bar{h}^1 , $b_2 > 0$. At \bar{h}^2 , $b_2 < 0$. We observe that the quadratic approximation captures the concavity of the bifurcation curve and provides a better

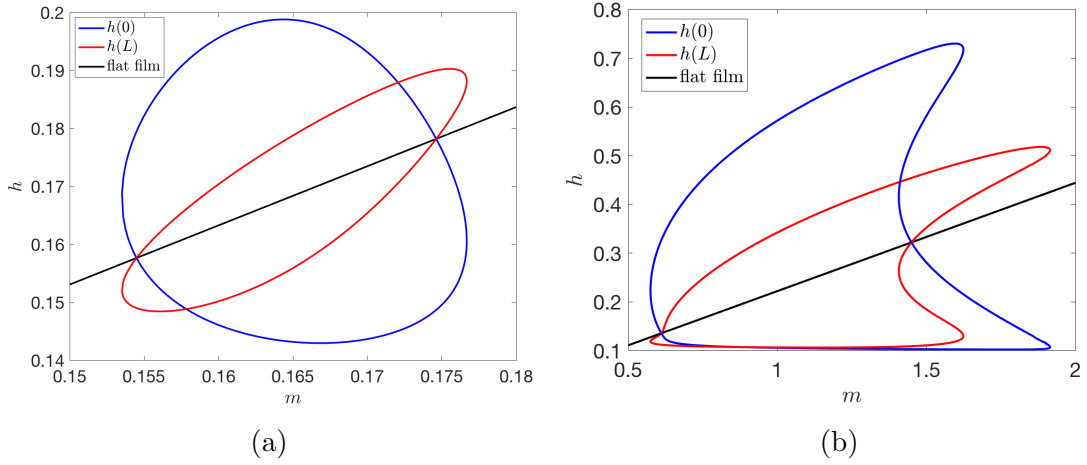


FIGURE 3.15: Bifurcation diagram of $h(0)$ and $h(L)$ vs. m for (a) $L = 1.4$ and (b) $L = 3$. The blue curve represents $h(0)$. The red curve represents $h(L)$. The black curve represents the flat film solution.

prediction of the bifurcation structure. Similarly, Figure 3.16 (c) and (d) show the linear and quadratic approximation computed at \bar{h}^1 and \bar{h}^2 for $L = 3$. At \bar{h}^1 , $b_2 > 0$. At \bar{h}^2 , $b_2 > 0$. Compared to Figure 3.16 (a)-(b), we observe a change in concavity of the bifurcation structure near \bar{h}^2 , which is reflected only through the quadratic approximation.

3.4 Summary

In this chapter, we presented the formulation and analysis of 1-D steady-state solutions and axisymmetric solutions subject to no-flux boundary conditions. In Section 3.1, we first reviewed the phase-plane analysis for 1-D steady-states and classified the steady-state solutions into three types, i.e. periodic solution, homoclinic solution and solution whose derivative diverges to infinity. We then reviewed the asymptotic analysis previously derived for large homoclinic droplets in the limit of small ϵ . Next, we illustrated the difference between a large and small droplet, based on which, we developed by an approximation for the profiles of small-mass droplets by introducing

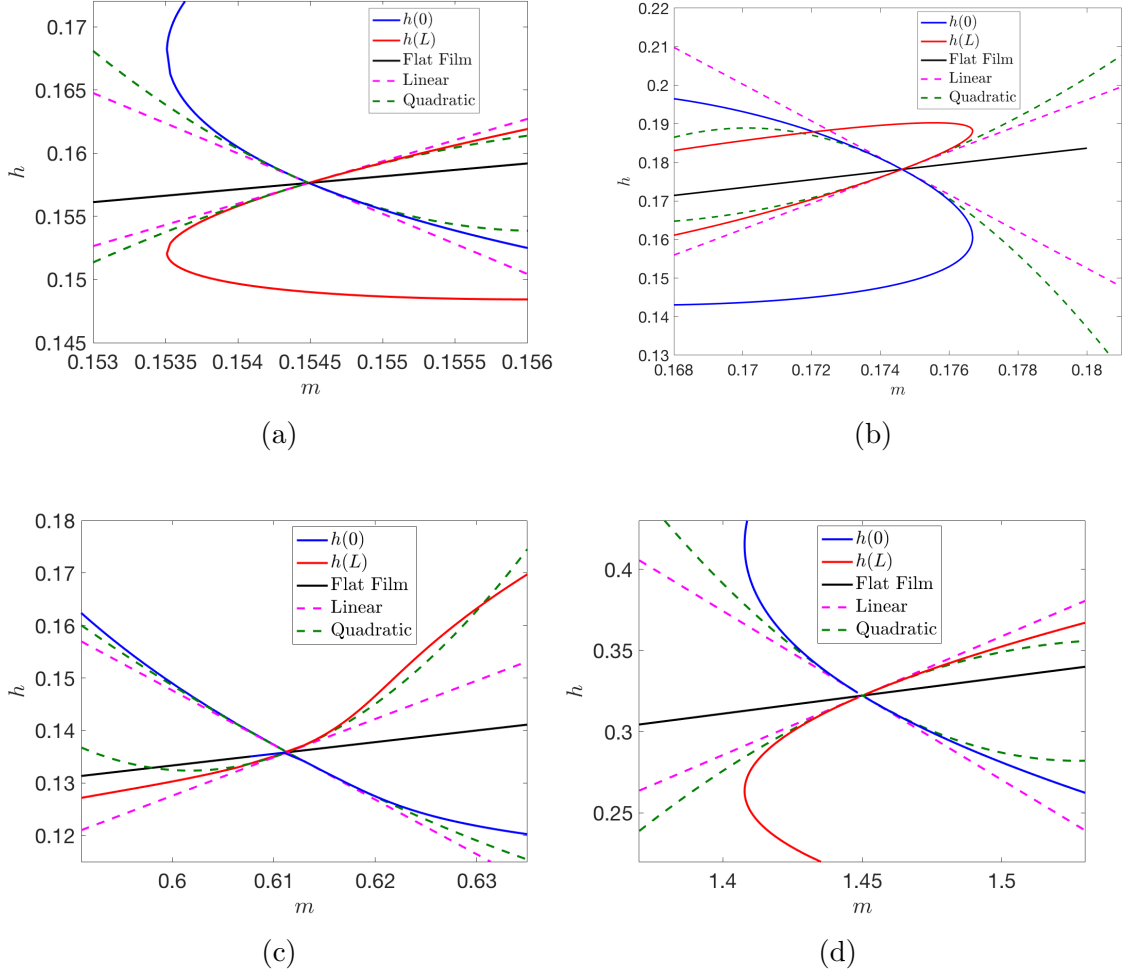


FIGURE 3.16: Bifurcation of $h(0), h(L)$ vs. m at (a) \bar{h}^1 for $L = 1.4$ (b) \bar{h}^2 for $L = 1.4$ (c) \bar{h}^1 for $L = 3$ (d) \bar{h}^2 for $L = 3$. The solid curves represent the numerical solution. The dashed curves represent the linear and quadratic approximations.

an approximate steady-state equation. Through numerical simulations, we showed that the homoclinic droplet profile can be well described by hyperbolic functions in the limit of small mass.

In Section 3.2, we extended the asymptotic analysis for large 1-D droplets to large axisymmetric droplets in the limit of small ϵ . Through asymptotic analysis, we showed that the large axisymmetric droplets could be described a parabola similar to the large 1-D droplets, with a modified coefficient. In Section 3.3, we discussed

the stability and bifurcation of 1-D steady-state solutions on a finite domain $[0, L]$. Through numerical simulations, we demonstrated the dependence of solution stability on droplet pressure and domain size L . We also illustrated the change in local bifurcation structure near the small-mass droplets as L increases and the destabilizing effect of increasing L on these small-mass droplets.

For the bifurcation of axisymmetric droplets, we first reviewed the leading order asymptotic results derived previously for axisymmetric droplets with only attractive van der Waals forces. To develop a further understanding of the local structure of the bifurcation, we expanded the previous work by computing a higher-order approximation and considering droplets with both attractive and repulsive van der Waals forces. We showed that the higher-order term depends on both the form of the disjoining pressure and the domain size L and that it captures the local concavity of the bifurcation structure, which has not been captured by the leading order term in previous studies.

Thin films on heterogeneous substrates

Chemically structured substrates have been used extensively in applications where accurate dispensing and distribution of fluids on a substrate is required. Classic theory states that the disjoining pressure of a thin film on chemically homogeneous substrate is given by $A\Pi(h)$ where A is a constant is called Hamaker constant, which measures the strength of van der Waals interactions. To study the dynamics and steady-states of thin films on chemically heterogeneous substrates, Thiele and Kao have both considered thin film flow on a chemically patterned substrates by incorporating a spatially dependent disjoining pressure [34, 66]. Specifically, they introduced a spatially dependent Hamaker constant $A(x)$ into the van der Waals potential. They considered a van der Waals potential of the form

$$\tilde{\Pi}(h, x) = A(x)\Pi(h) \quad (4.1)$$

on a domain with periodic boundary conditions where $A(x) = 1 + \varepsilon \cos\left(\frac{2\pi}{P_{\text{het}}}x\right)$. Here, P_{het} represents the imposed heterogeneity period and $\varepsilon \ll 1$ characterizes the amplitude of heterogeneity. The smooth spatial variation and the assumption that

$\varepsilon \ll 1$ allow for the analysis of the solutions on heterogeneous substrates through an asymptotic expansion in terms of ε .

However, for an engineered patterned substrate, a piecewise-constant $A(x)$ would be a better description than a sinusoidal pattern. For example, micro-patterned surfaces with alternate hydrophilic and hydrophobic rectangular areas are extensively used in digital microfluidics and high-throughput screening nanoarrays [38]. In such applications, a stepwise Hamaker constant is needed to model the chemical properties of the surfaces. Kao et al. studied the stationary states of thin films on substrates with square-wave patterning in both 1-D and 2-D [34]. Specifically, they considered a stepwise $A(x)$ with periodic boundary conditions, which is given by

$$A(\xi) = \begin{cases} 1 + \varepsilon^3, & 0 \leq \xi \leq \frac{\pi}{2} \\ 1, & \frac{\pi}{2} \leq \xi \leq \frac{3\pi}{2} \\ 1 + \varepsilon^3, & \frac{3\pi}{2} \leq \xi \leq 2\pi \end{cases} \quad (4.2)$$

for some $\xi = k_p x$ that is scaled by the patterning wavenumber k_p . To study the bifurcation of stationary states on substrates with such patterning, they wrote $A(x)$ as a Fourier series. In particular, they performed asymptotic analysis for solutions near the bifurcation point. Imperfect bifurcations were observed for chemical patterning of the form (4.2). They found that the bifurcation and steady-states resemble those of sinusoidally patterned substrates.

In this chapter, we explore the steady-state profile and bifurcation diagram of thin film on a stepwise-patterned substrate. Unlike the work presented in [34, 66], we consider thin film on a finite domain subject to no-flux boundary conditions so that the total fluid mass is conserved. Instead of considering a spatial modulation with small amplitude, we extend our study to a more generalized step function $A(x)$

of the form given by (4.3) where the amplitude of $A(x)$ need not be small.

$$A(x) = \begin{cases} A_1 & 0 \leq x \leq s \\ A_2 & s < x \leq L \end{cases} \quad (4.3)$$

Here, L is the size of the domain and A_i is a constant. The disjoining pressure we will consider in this chapter is given by

$$\tilde{\Pi}(h, x) = A(x) \left(\frac{\epsilon^2}{h^3} - \frac{\epsilon^3}{h^4} \right) \quad (4.4)$$

for $A(x)$ of the form (4.3).

4.1 Introduction of chemical heterogeneity into substrates

The evolution of thin liquid films, subject to no-flux boundary conditions, on a finite heterogeneous substrate with patterning $A(x)$ is governed by

$$\frac{\partial h}{\partial t} = \frac{\partial}{\partial x} \left(h^3 \frac{\partial}{\partial x} \left(A(x) \Pi(h) - \frac{\partial^2 h}{\partial x^2} \right) \right) \quad (4.5a)$$

$$J(0) = J(L) = 0, \quad \frac{\partial h}{\partial x}(0) = \frac{\partial h}{\partial x}(L) = 0 \quad (4.5b)$$

For the same reason stated previously for homogeneous case in Chapter 3, the boundary condition (4.5b) reduces to

$$\frac{\partial h}{\partial x}(0) = \frac{\partial h}{\partial x}(L) = 0, \quad \frac{\partial^3 h}{\partial x^3}(0) = \frac{\partial^3 h}{\partial x^3}(L) \quad (4.6)$$

It follows that the steady-state solution is parametrized by uniform pressure $p \equiv \bar{p}$ just like in the 1-D case described in Chapter 3. The steady-state equation on a heterogeneous substrate with patterning described by $A(x)$, subject to no-flux boundary conditions in 1-D is thus given by

$$h_{xx} = A(x) \Pi(h) - \bar{p} \quad (4.7a)$$

$$h_x(0) = h_x(L) = 0 \quad (4.7b)$$

In the following sections of this chapter, we consider a stepwise $A(x)$ of the form (4.3). We seek solution that is continuous and whose derivative is continuous at $x = s$, i.e.

$$\lim_{x \rightarrow s^-} h(x) = \lim_{x \rightarrow s^+} h(x) \quad (4.8a)$$

$$\lim_{x \rightarrow s^-} h'(x) = \lim_{x \rightarrow s^+} h'(x) \quad (4.8b)$$

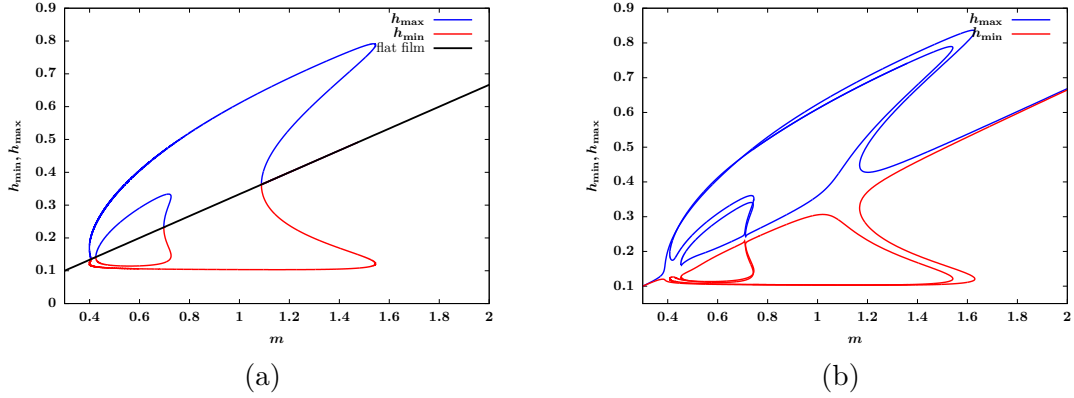


FIGURE 4.1: Bifurcation diagram for m vs. h_{\min}, h_{\max} for steady-state solutions (a) on homogeneous substrate $A(x) \equiv 1$ for $L = 3$. (b) on heterogeneous substrate with patterning of the form (4.3) where $L = 3$, $s = 1.5$, $A_1 = 1$, and $A_2 = 1.1$. In both (a) and (b), the solid blue curve represents the maximum film thickness. The red curve represents the minimum film thickness. In both (a) and (b), $\epsilon = 0.1$.

Since $A(x)$ is a step function with $A_1 \neq A_2$, for a steady-state solution to be a flat film, i.e. $h(x) \equiv \bar{h}$, the only option is to have $\Pi(\bar{h}) = 0$, yielding $\bar{h} = \epsilon$. Hence, $h(x) \equiv \epsilon$ is the only possible flat film solution with pressure $p \equiv 0$. Figure 4.1 (a) and (b) show the film mass plotted against the maximum and minimum film thickness denoted by h_{\max} and h_{\min} respectively on homogeneous and stepwise-patterned substrate on $[0, L]$ for $L = 3$. In Figure 4.1 (a), the solid black curve represents the flat film solution. On a stepwise-patterned substrate with $A_2 = 1.1$ and $s = 1.5$, there is no more flat film solution except for the solution $h(x) \equiv \epsilon$,

as shown in Figure 4.1 (b). In presence of spatially modulated disjoining pressure, the steady-state solutions centered at $x = 0$ and $x = L$ are no longer symmetric with respect to the center of the domain since $A_1 \neq A_2$. As a consequence, in the bifurcation diagram, there are two distinct branches representing droplets centered at two different sides of the domain with the same mass. For thin liquid films on a homogeneous substrate with $L = 3$, there are two branches in total. As we introduce chemical heterogeneity by choosing $s = 1.5$ and $A_2 = 1.1$, we observe two loops, an outer loop and an inner loop. The number of loops is related to the number of bifurcation points, which is determined by the domain size L . The bifurcation points h_k of the steady-state solutions on a finite homogeneous substrates subject to no-flux boundary conditions were previously given in [7], i.e.

$$\Pi'(h_k) = -\frac{k^2\pi^2}{L^2} \quad (4.9)$$

Compared to the homogeneous case, two new branches arise in the bifurcation diagram for the heterogeneous case, which leads to a total of four branches of solutions, as shown in Figure 4.1 (b). Figure 4.2 (a) shows two distinct droplets centered at the two different sides of the domain with the same mass $m = 0.6$. Due to the heterogeneity of the substrates ($A_1 \neq A_2$), the two droplets are asymmetric, as can be observed from the two different black dashed lines which denote the maximum height of the two droplets. Figure 4.2 (b) shows three distinct steady-state solutions on the inner loop with the same mass $m = 0.6$. The blue solid curve and the red square-dotted curve represent two smaller-amplitude solutions. The solid blue curve describes two droplets in the domain. However, these droplets are not identical, as can be seen from the two black dashed lines, which denote the respective maximum thickness of each solution. The purple triangle-dotted curve represents a solution slightly perturbed from a constant, which is analogous to the flat film solution on a homogeneous substrate.

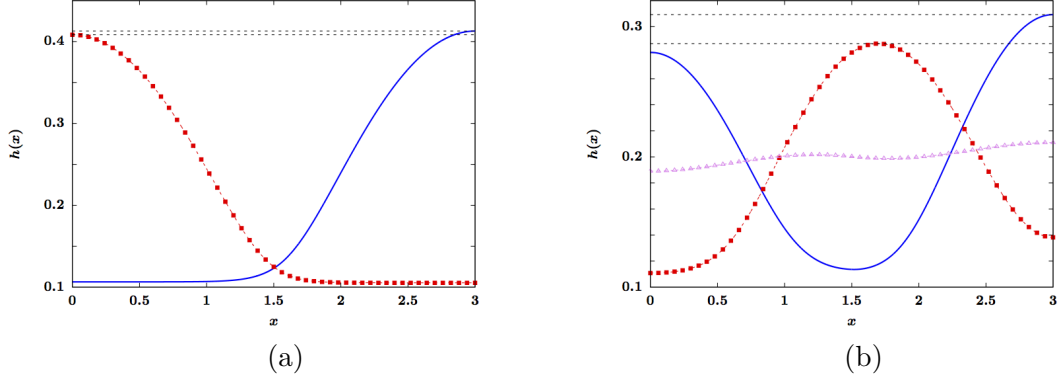


FIGURE 4.2: (a) Asymmetric steady-state droplets centered at $x = 0$ and $x = L$ with the same mass $m = 0.6$. The difference in droplet height is highlighted by two black dashed lines. (b) Profiles of three distinct steady-state solutions on the inner loop, all with the same mass $m = 0.6$. Compared to the two solutions in (a), these solutions have smaller amplitude. In both (a) and (b), $A_1 = 1$, $A_2 = 1.1$, $m = 0.6$, $\epsilon = 0.1$.

In Figure 4.1 (b), $A_2 - A_1$ is relatively small so the structure of the bifurcation diagram is only slightly perturbed from that of the homogeneous case. As we keep increasing A_2 with $A_1 = 1$ fixed, the structure of the bifurcation diagram changes more drastically. Figure 4.5 (a)-(i) illustrate the evolution of the structure of the inner loop as A_2 increases from $A_2 = 1.1$ to $A_2 = 7$.

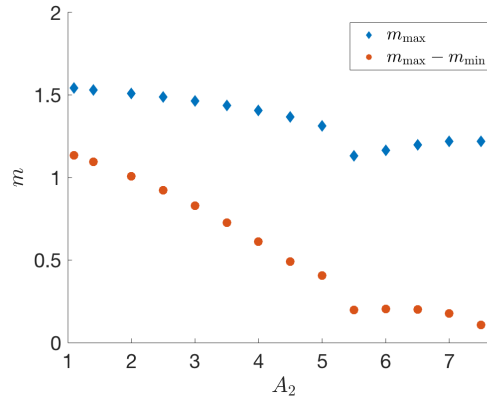


FIGURE 4.3: Maximum film mass m_{\max} and $m_{\max} - m_{\min}$ computed for the inner loop, like those shown in Figure 4.5 (a)-(i), plotted against a set of increasing A_2 values, for $L = 3$, $s = 1.5$.

Figure 4.3 shows the change in structure of the bifurcation diagram measured by m_{\max} and $m_{\max} - m_{\min}$ where m_{\max} and m_{\min} denote the maximum and minimum film mass of the loops in Figure 4.5 (a)-(i) as A_2 changes. For A_2 between 1.1 and 5.5, as A_2 increases, $m_{\max} - m_{\min}$ decreases steadily. For A_2 between 5.5 and 7, $m_{\max} - m_{\min}$ first increases and then decreases slightly. For $A_2 > 7$, $m_{\max} - m_{\min}$ decreases rapidly to zero, implying that the inner loop solutions representing droplets centered at $x = L$ exist on an increasingly small parameter range as A_2 grows. As the A_2 region becomes more hydrophobic, it is less likely for the film to concentrate its mass on the A_2 region with droplets centered at $x = L$. When $A_2 = 7$, the structure of the bifurcation diagram degenerates into a closed loop with no self-intersections as shown in Figure 4.5 (i). As A_2 continues to increase, the loop shrinks and eventually vanishes in the limit of large A_2 . Similarly, we study the structure of the outer loop which characterizes droplets centered at $x = 0$ as A_2 increases. We define m_{\max} to be the maximum mass for which a droplet-type steady-state centered at $x = 0$ could exist, as labeled by the black dashed line in Figure 4.4 for the outer loop in the bifurcation diagram presented earlier in Figure 4.1 (b).

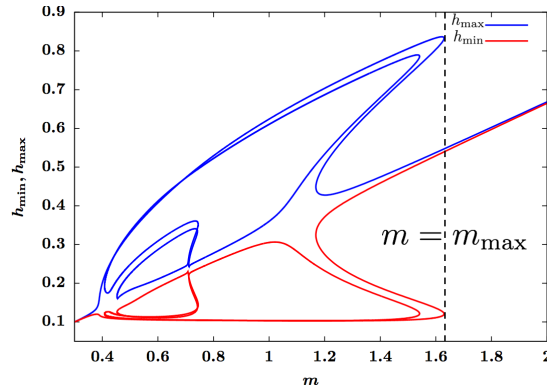


FIGURE 4.4: Definition of m_{\max} for the outer loop structure in the bifurcation diagram.

We will show later in Section 4.2.5 that in the limit $A_2 \rightarrow \infty$ or $\epsilon \rightarrow 0$, $m_{\max} \sim \frac{\sqrt{A_2} L^2}{3\sqrt{3}}$, suggesting that unlike the inner loop which shrinks in size as A_2 increases,

the outer loop characterizing droplets centered at $x = 0$ grows in size as A_2 increases. As A_2 becomes larger, the A_2 region becomes more hydrophobic, in which case, the fluid mass will become increasingly concentrated on the A_1 region. For large A_2 , the solid substrate is capable of supporting droplets of mass that scales with $\sqrt{A_2}$. For this reason, in the remaining sections of this chapter, we will focus on the branch of solutions on the outer loop of the bifurcation diagram, which primarily describes one single droplet whose maximum film thickness occurs at $x = 0$.

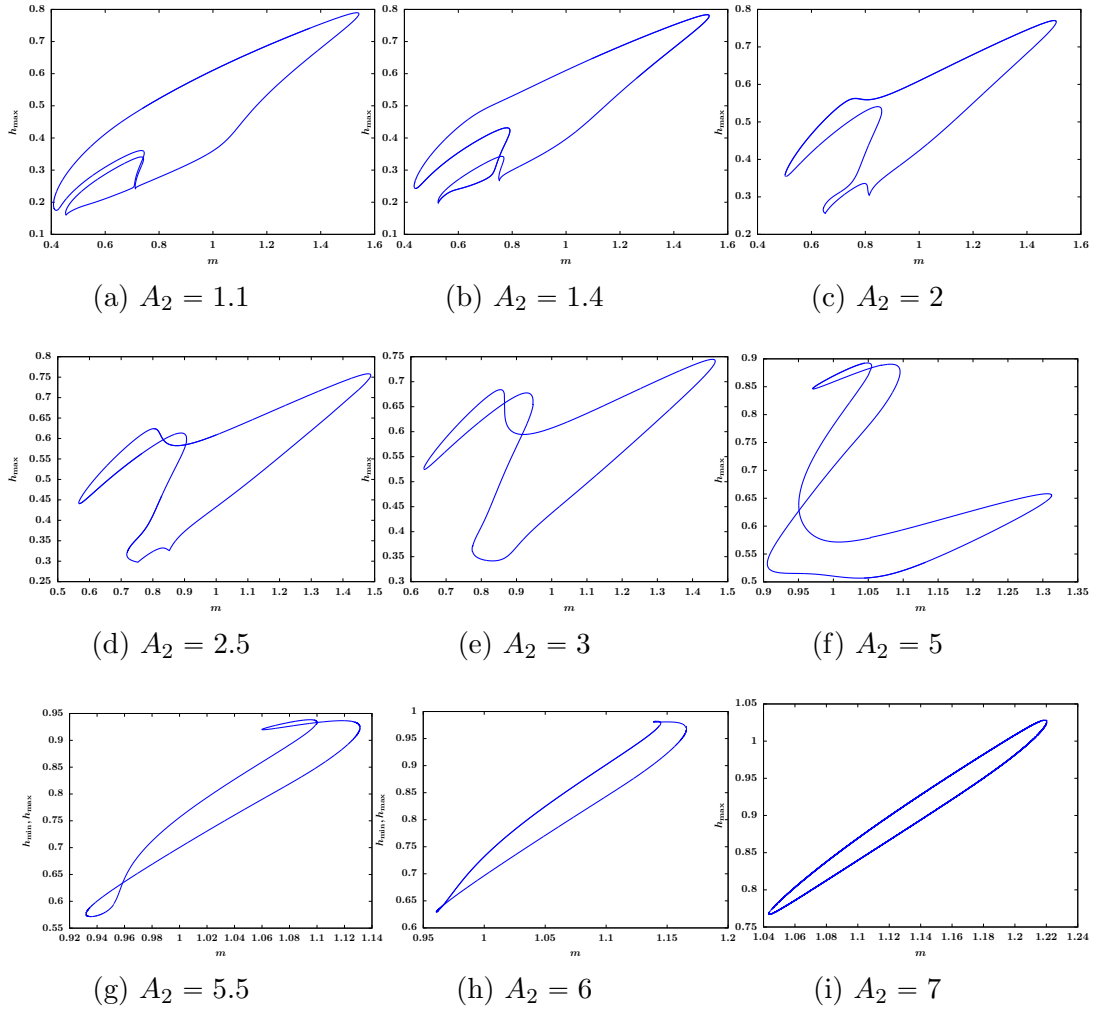


FIGURE 4.5: Bifurcation diagram for m vs. h_{\max} for steady-state solutions on a heterogeneous substrate for $A_1 = 1$ and a range of A_2 values. In (a)-(i), $L = 3$, $s = 1.5$, $\epsilon = 0.1$.

Figure 4.6 (a)-(b) show the bifurcation diagram p vs. h_{\max} for steady-states on homogeneous and heterogeneous substrates on a domain of length $L = 6$ with $\epsilon = 0.001$. On the heterogeneous substrate, we let $A_2 = 1.5$, $s = 3$. In Figure 4.6 (a), the solid blue curve represents nontrivial steady-state solutions. The dashed black curve represents two branches of flat film solutions that merge with the nontrivial branch at $\bar{p} = p_{\max} = \frac{27}{256\epsilon}$. Figure 4.6 (b) shows the same bifurcation diagram plotted for thin films on heterogeneous substrates with parameter values $A_1 = 1$, $A_2 = 1.5$, and $s = 3$. In the limit of small ϵ , we observe a clear division of segments of the bifurcation curve. Based on these divided segments, we classify all the steady-state solutions that could exist on such substrates into six different branches, each of which corresponds to a segment of the bifurcation curve labeled in Figure 4.6 (b). Although there is no more flat film solution except for $h(x) \equiv \epsilon$ for $A_1 \neq A_2$, as we will show later in Section 4.2.1 and Section 4.2.2, branch 1 and branch 6 are two branches that are analogous to the flat film solutions in Figure 4.6 (a). Branch 3 is an entirely new branch of solutions characterizing a class of “pinned” droplets that emerges due to the presence of chemical heterogeneity. In the following subsections, we will present our analysis and computation of these steady-state solutions by branch. For each branch, we develop an asymptotic prediction for the steady-state profile and show that the leading order solution for each branch depends on different parameters in (L, s, A_1, A_2) , which describe the chemical heterogeneity of the substrates.

4.2 Classification of branches of bifurcation diagram in 1-D

Based on the structure of the diagram shown in Figure 4.6 (b), we divide the steady-state solutions that could exist on a heterogeneous substrate for $A(x)$ of the form (4.3) into six different categories, as follows.

- Branch 1: small-thickness films

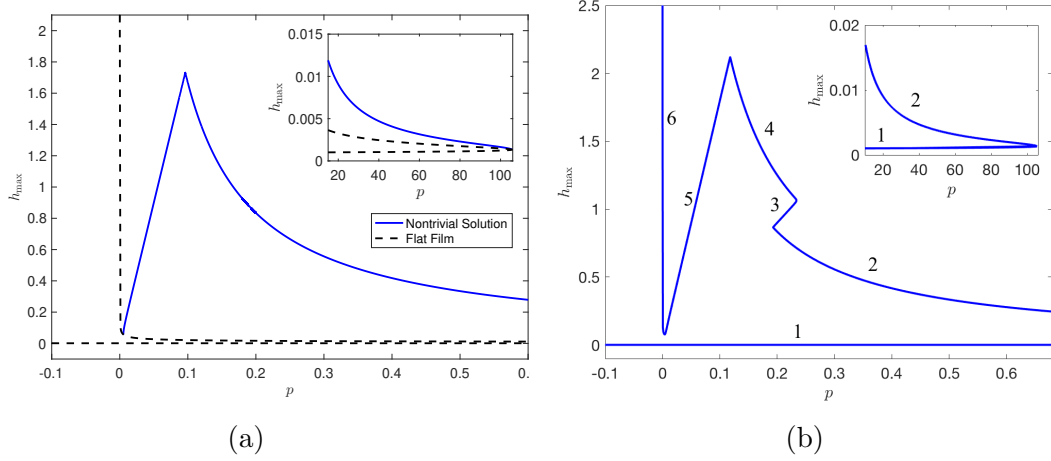


FIGURE 4.6: Bifurcation diagram p vs. h_{\max} for steady-states on (a) a homogeneous substrate $A(x) \equiv 1$. (b) on a heterogeneous substrate with $A_1 = 1$, $A_2 = 1.5$, $s = 3$. In both (a) and (b), $\epsilon = 0.001$ and $L = 6$.

- Branch 2: small-width droplets
- Branch 3: pinned droplets
- Branch 4: large-width droplets
- Branch 5: large confined droplets
- Branch 6: large-thickness films

For each class of solutions, we present asymptotic analysis of the profile and the bifurcation diagram of steady-state solutions. Through asymptotic analysis and numerical simulations, we illustrate the leading order dependence of solutions on parameters such as mass, pressure and domain length. Instead of employing a Fourier series approach, we use the piecewise-constant definition of $A(x)$ through a phase-plane approach, which allows us to perform asymptotic analysis in the limit of large heterogeneity contrast. In the limit of large A_2 , the A_2 region becomes increasingly hydrophobic and has an increasingly confining effect on the fluid in the A_1 region.

As a consequence, there is less fluid leaking from the A_1 region onto the A_2 region as A_2 increases. To quantify this phenomenon, we present an effective measure of the fluid leakage. We show that this leakage is inversely proportional to A_2 in the limit of large A_2 . Finally, we show that the results derived in 1-D can be easily extended to axisymmetric solutions.

4.2.1 Small-thickness films

First, we study branch 1, which characterizes steady-state solutions with small mass, specifically with $m = O(\epsilon L)$ or smaller. Two examples of steady-state profiles on branch 1 are given in Figure 4.7 (a) and (b). Figure 4.7 (a) shows an example of a steady-state on branch 1 with mass $m > \epsilon L$ and pressure $\bar{p} > 0$. For such solutions, the maximum of the film thickness occurs at $x = 0$. Figure 4.7 (b) shows an example of a steady-state on branch 1 with mass $m < \epsilon L$ and pressure $\bar{p} < 0$. For such solutions, the maximum film thickness occurs at $x = L$. Both solutions are characterized by nearly flat film away from the interface $x = s$ and a rapid change in the profile in a small neighborhood of $x = s$.

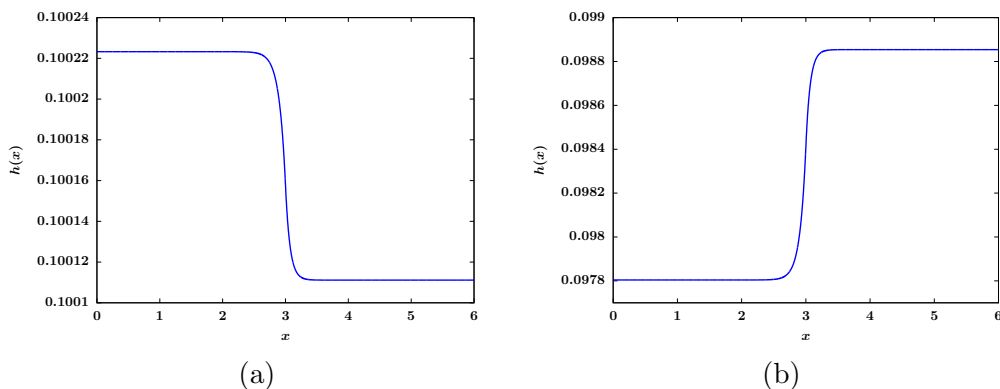


FIGURE 4.7: A steady-state profile on branch 1 with (a) pressure $\bar{p} > 0$, $m = 0.601 > \epsilon L$ (b) $\bar{p} < 0$, $m = 0.59 < \epsilon L$. In both (a) and (b), $A_1 = 1$, $A_2 = 2$, $L = 6$, $s = 3$, $\epsilon = 0.1$.

The rapid change in the steady-state profile $h(x)$ near the interface is due to the

change in disjoining pressure for films of thickness $h = O(\epsilon)$. For films of thickness $h = O(\epsilon)$, the disjoining pressure $\Pi(h)$ increases rapidly on the thickness range $0 < h < \frac{4}{3}\epsilon$ in the limit $\epsilon \rightarrow 0$. For solutions on branch 1, the film thickness $h(x)$ falls within this range. To describe the solution on this branch, we seek a rescaled solution for h . We rescale h by writing $h = \epsilon^a H$ for some $a > 0$. In the rescaled variable H , the steady-state equation given by (4.7a) can thus be written as

$$\epsilon^a H'' = A(x)\Pi(\epsilon^a H) - \bar{p} \quad (4.10)$$

We seek an outer solution of the form $H = H_0 + \epsilon H_1 + H.O.T.$ and will construct solutions using matched asymptotic expansion. The leading order equation is then given by

$$A(x)\Pi(\epsilon^a H_0) - \bar{p} = 0 \quad (4.11)$$

Using the piecewise definition of $A(x)$, we know that for $0 \leq x \ll s$, $A(x) = A_1$ and for $s \ll x \leq L$, $A(x) = A_2$. Hence, H_0 satisfies

$$A_1 \Pi(\epsilon^a H_0) = \bar{p}, \quad 0 \leq x \ll s \quad (4.12a)$$

$$A_2 \Pi(\epsilon^a H_0) = \bar{p}, \quad s \ll x \leq L \quad (4.12b)$$

Let $h_{\min i}$ be the saddle point on a homogeneous substrate with $A \equiv A_i$ for a given pressure \bar{p} , as described previously in Chapter 3. Then we have $\epsilon^a H_0 = h_{\min 1}$ for $0 \leq x \ll s$ and $\epsilon^a H_0 = h_{\min 2}$ for $s \ll x \leq L$.

$$\text{For } h \ll \epsilon \text{ and } \bar{p} \rightarrow -\infty, \Pi(\epsilon^a H_0) = \epsilon^{3-4a} H_0^{-4} \left(-1 + \frac{\epsilon^a H}{\epsilon} \right) \sim -\epsilon^{3-4a} H_0^{-4} = \frac{\bar{p}}{A_i}.$$

We choose $a = \frac{3}{4}$. This gives

$$H_0 = \frac{A_i^{\frac{1}{4}}}{(-\bar{p})^{\frac{1}{4}}} \quad (4.13)$$

Hence, $h_{\min i} = \epsilon^a H_0 \sim \frac{\epsilon^{\frac{3}{4}} A_i^{\frac{1}{4}}}{(-\bar{p})^{\frac{1}{4}}} \ll \epsilon$ for $\bar{p} \gg \epsilon^{-1}$.

For $h \sim \epsilon$ and $\bar{p} \rightarrow 0$, since we know $\Pi(\epsilon) = 0$, we choose $a = 1$. To see the dependence of H_0 on \bar{p} , we write $H_0 = 1 + \epsilon h_1$ and expand $\Pi(\epsilon H_0)$ near $H_0 = 1$. We get

$$\Pi'(\epsilon)\epsilon^2 h_1 = \frac{\bar{p}}{A_i} \quad (4.14)$$

This gives $h_1 = \frac{\bar{p}}{A_i}$ and therefore $h_{\min i} = \epsilon H_0 \sim \epsilon + \frac{\epsilon^2 \bar{p}}{A_i}$ for $\bar{p} \rightarrow 0$.

To compute the next order solution H_1 , we use Taylor expansion of $\Pi(h)$ around $h = \epsilon^a H_0 = h_{\min i}$. At $O(\epsilon^{a+1})$,

$$H_1'' = A(x)\Pi'(\epsilon^a H_0)H_1 \quad (4.15)$$

We have shown that $h_{\min i} \sim \frac{\epsilon^{\frac{3}{4}} A_i^{\frac{1}{4}}}{(-\bar{p})^{\frac{1}{4}}}$ as $\bar{p} \rightarrow -\infty$ and $h_{\min i} \sim \epsilon + \frac{\epsilon^2 \bar{p}}{A_i}$ as $\bar{p} \rightarrow 0$. It

follows that $\Pi'(h_{\min i}) = O\left(\frac{1}{\epsilon}\right)$ as $\bar{p} \rightarrow -\infty$ and $\Pi'(h_{\min i}) = O\left(\frac{1}{\epsilon^2}\right)$ as $\bar{p} \rightarrow 0$. As

$\epsilon \rightarrow 0$, $\Pi'(\epsilon^a H_0) \gg 1$. Now we introduce another small positive parameter σ_i so that

$\Pi'(\epsilon^a H_0) = \Pi'(h_{\min i}) = \frac{1}{\sigma_i}$ on the A_i region. Then the equation for H_1 on the A_i

region can be rewritten as

$$\sigma_i H_1'' = A_i H_1 \quad (4.16)$$

We observe that (4.16) also has a boundary layer. The outer solution at leading order is given by $H_1^{\text{out}} \equiv 0$. For H_0 , we use the piecewise constant property of $A(x)$ for x away from $x = s$. For x near $x = s$, we expect a boundary layer so we rescale x by letting $X = \frac{x-s}{\sigma_i^b}$ on the A_i region for some $b > 0$. This gives

$$\sigma_i^{1-2b} H_1'' = A_i H_1 \quad (4.17)$$

Choose $b = \frac{1}{2}$. Solving for H_1 , we have

$$H_1 = B_i e^{\sqrt{A_i} X} + D_i e^{-\sqrt{A_i} X} \quad (4.18)$$

where B_i and D_i are two constants for the solution on the A_i region. For $0 \leq x \leq s$ (A_1 region), we need $H'_1(X) \rightarrow 0$ as $X \rightarrow -\infty$ so $D_1 = 0$. For $s \leq x \leq L$ (A_2 region), we need $H'_1(X) \rightarrow 0$ as $X \rightarrow \infty$ so $B_2 = 0$. This gives

$$H_1 = B_1 e^{\frac{\sqrt{A_1}(x-s)}{\sqrt{\sigma_1}}} \quad 0 \leq x \leq s \quad (4.19a)$$

$$H_1 = D_2 e^{-\frac{\sqrt{A_2}(x-s)}{\sqrt{\sigma_2}}} \quad s \leq x \leq L \quad (4.19b)$$

Hence, at leading order, the profile of the solution with mass $m = O(\epsilon L)$ on branch 1 can be described by

$$h(x) \sim \begin{cases} h_{\min 1} + C_1 e^{\sqrt{A_1 \Pi'(h_{\min 1})}(x-s)} & 0 \leq x \leq s \\ h_{\min 2} + C_2 e^{-\sqrt{A_2 \Pi'(h_{\min 2})}(x-s)} & s < x \leq L \end{cases} \quad (4.20)$$

for some constant C_1, C_2 to be determined by the continuity of $h(x)$ and $h'(x)$. To determine C_1 and C_2 , we use the continuity of $h(x)$ and $h'(x)$ at $x = s$, given by (4.8a) and (4.8b), which is restated below.

$$\lim_{x \rightarrow s^-} h(x) = \lim_{x \rightarrow s^+} h(x) \quad (4.21a)$$

$$\lim_{x \rightarrow s^-} h'(x) = \lim_{x \rightarrow s^+} h'(x) \quad (4.21b)$$

This gives

$$C_1 = -\frac{(h_{\min 1} - h_{\min 2})\sqrt{A_2 \Pi'(h_{\min 2})}}{\sqrt{A_1 \Pi'(h_{\min 1})} + \sqrt{A_2 \Pi'(h_{\min 2})}} \quad (4.22a)$$

$$C_2 = \frac{(h_{\min 1} - h_{\min 2})\sqrt{A_1 \Pi'(h_{\min 1})}}{\sqrt{A_1 \Pi'(h_{\min 1})} + \sqrt{A_2 \Pi'(h_{\min 2})}} \quad (4.22b)$$

Hence,

$$h(0) \sim h_{\min 1} + C_1 e^{-\sqrt{A_1 \Pi'(h_{\min 1})}s} \quad (4.23a)$$

$$h(L) \sim h_{\min 2} + C_2 e^{-\sqrt{A_2 \Pi'(h_{\min 2})}(L-s)} \quad (4.23b)$$

We have shown that $h_{\min i} \sim \frac{\epsilon^{\frac{3}{4}} A_i^{\frac{1}{4}}}{(-\bar{p})^{\frac{1}{4}}}$ as $\bar{p} \rightarrow -\infty$ and $h_{\min i} \sim \epsilon + \frac{\epsilon^2 \bar{p}}{A_i}$ as $\bar{p} \rightarrow 0$. It

follows that $\Pi'(h_{\min i}) = O\left(\frac{1}{\epsilon}\right)$ as $\bar{p} \rightarrow -\infty$ and $\Pi'(h_{\min i}) = O\left(\frac{1}{\epsilon^2}\right)$ as $\bar{p} \rightarrow 0$.

Hence, as $\bar{p} \rightarrow -\infty$,

$$C_1 \sim \frac{\epsilon^{3/4}}{(-\bar{p})^{1/4}} (A_2^{1/4} - A_1^{1/4}) \frac{A_1^{1/8}}{A_1^{1/8} + A_2^{1/8}} \quad (4.24a)$$

$$C_2 \sim \frac{\epsilon^{3/4}}{(-\bar{p})^{1/4}} (A_1^{1/4} - A_2^{1/4}) \frac{A_2^{1/8}}{A_1^{1/8} + A_2^{1/8}} \quad (4.24b)$$

For $\bar{p} \rightarrow 0$,

$$C_1 \sim -\frac{h_{\min 1} - h_{\min 2}}{\sqrt{\frac{A_1}{A_2}} + 1} \quad (4.25a)$$

$$C_2 \sim \frac{h_{\min 1} - h_{\min 2}}{\sqrt{\frac{A_2}{A_1}} + 1} \quad (4.25b)$$

For $A_1, A_2 = O(1)$, $C_i = O(\epsilon^2 \bar{p})$ so $C_i \ll h_{\min i}$ for as long as $\bar{p} \ll \epsilon^{-1}$. For $A_1 = O(1)$ and $A_2 \rightarrow \infty$, $C_1 = O(\epsilon^2 \bar{p}) \ll h_{\min 1}$ and $C_2 = O\left(\frac{\epsilon^2 \bar{p}}{\sqrt{A_2}}\right) \ll h_{\min 2}$ for $\bar{p} \ll \epsilon^{-1}$.

In the limit $\bar{p} \rightarrow -\infty$, in order for the linearization of $h(x)$ around $h_{\min i}$ to be valid, we need $A_1 - A_2 \ll 1$ so that $C_i \ll h_{\min i}$ near $x \sim s$. Hence, (4.24a)-(4.24b) are valid for $A_1 - A_2 \ll 1$. To capture the solution profile near $x = s$ as $\bar{p} \rightarrow -\infty$,

we seek an alternative scaling by letting $\delta = -\frac{1}{\bar{p}}$ for $\delta \ll 1$. Since $h_{\min i} \sim \frac{\epsilon^{\frac{3}{4}} A_i^{\frac{1}{4}}}{(-\bar{p})^{\frac{1}{4}}}$, we

scale h by $h = \delta^{1/4} H$ and we have $A_i \Pi(h) \sim -A_i \frac{\epsilon^3}{h^4}$. This gives

$$\delta^{1/4} H_{xx} = -\frac{A\epsilon^3}{\delta H^4} + \frac{1}{\delta} \quad (4.26)$$

To describe the boundary layer as $x \rightarrow s$, we let $X = \frac{x-s}{\delta^a}$. Hence,

$$\delta^{1/4-2a} H_{xx} = -\frac{A\epsilon^3}{\delta H^4} + \frac{1}{\delta} \quad (4.27)$$

By dominant balance, we get $a = \frac{5}{8}$, which suggests that the boundary layer scales

like $X \propto (-\bar{p})^{5/8}$ and the solution profile satisfies $H_{xx} = -\frac{\epsilon^3}{H^4} + 1$ to leading order.

Note that the scale of the boundary layer $a = \frac{5}{8}$ can also be obtained by using a

linearization approach, which gives $X = \frac{x-s}{A_i^{1/4} \epsilon^{3/4} \delta^{5/8}}$. In all cases, $h(0) - h_{\min 1}$ and

$h(L) - h_{\min 2}$ are both exponentially small as $\epsilon \rightarrow 0$. Hence, in the limit $\epsilon \rightarrow 0$, $h(0) \sim h_{\min 1}$ and $h(L) \sim h_{\min 2}$ to leading order.

Figure 4.8 (a) and Figure 4.8 (b) show the numerical solution of $h(0)$ and $h(L)$ compared with $h_{\min i}$, which is the leading order outer solution in both the limit $\bar{p} \rightarrow -\infty$ and $\bar{p} \rightarrow 0$. Figure 4.8 (c) and Figure 4.8 (d) show the leading order asymptotic approximation for $h_{\min i}$ in the limit $\bar{p} \rightarrow -\infty$ and $\bar{p} \rightarrow 0$ respectively. Because this type of small-mass solutions has a boundary layer near $x = s$, the steady-state profile for this class of solutions approaches the step function given by (4.28) in the limit $\epsilon \rightarrow 0$.

$$h_{\text{step}}(x) = \begin{cases} h_{\min 1}, & 0 \leq x \leq s \\ h_{\min 2}, & s < x \leq L \end{cases} \quad (4.28)$$

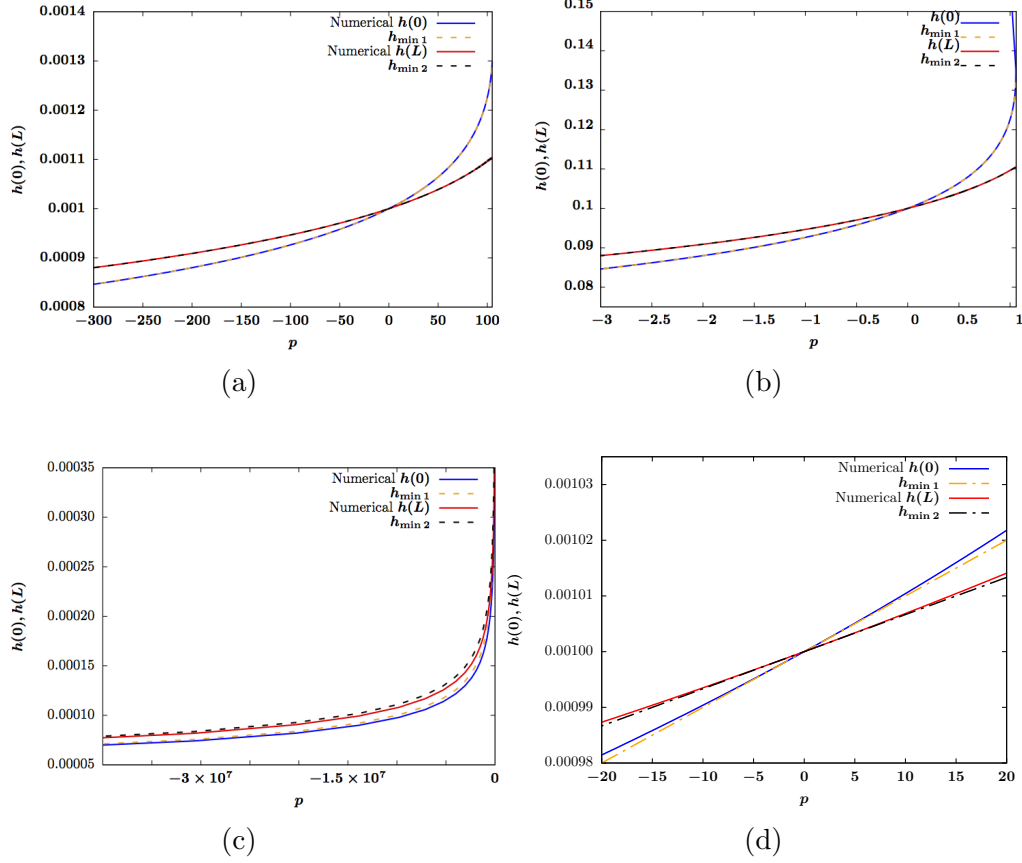


FIGURE 4.8: (a) Comparison of numerically computed $h(0)$, $h(L)$ and $h_{\min i}$ for $i = 1, 2$ for $\epsilon = 0.001$. (b) Same plot as (a) for $\epsilon = 0.1$. (c) Comparison of numerically computed $h(0)$, $h(L)$ and their further asymptotic reduction in the limit $p \rightarrow -\infty$ where $h(0)$ and $h(L)$ are asymptotically given by $\frac{\epsilon^{\frac{3}{4}} A_i^{\frac{1}{4}}}{p^{\frac{1}{4}}}$ for $i = 1$ and $i = 2$ respectively with $\epsilon = 0.001$. (d) Comparison of numerically computed $h(0)$, $h(L)$ and their respective further asymptotic reduction in the limit $p \rightarrow 0$ where $h(0)$ and $h(L)$ are asymptotically given by $\epsilon + \frac{\epsilon^2 p}{A_i}$ for $i = 1$ and $i = 2$ respectively with $\epsilon = 0.001$. In (a)-(d), $L = 6$, $s = 3$, $A_1 = 1$, $A_2 = 1.5$.

Figure 4.9 (a) shows a small-thickness thin film with $m = 0.31$ for $\epsilon = 0.1$, $L = 3$, when m is slightly greater than $\epsilon L = 0.3$. The red and black dashed curves represent the approximation on $[0, s]$ and $[s, L]$ given by (4.20) respectively. The two curves intersect at the interface $x = s$, as a result of the condition imposed by (4.8a) and (4.8b). Figure 4.9 (b) shows the thin film profile for $m = 0.2 < \epsilon L$ and $\bar{p} < 0$. When

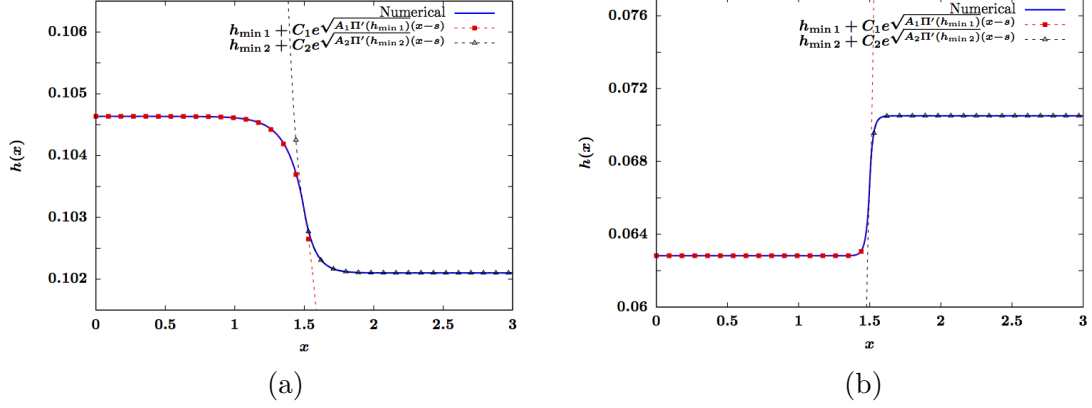


FIGURE 4.9: (a) A steady-state solution on heterogeneous substrate with mass slightly larger than ϵL , compared with its asymptotic prediction derived above on both the A_1 and A_2 region with parameter values $m = 0.31$, $p \equiv \bar{p} = 0.3498$. (b) A steady-state solution on the same heterogeneous substrate with large negative p , compared with its asymptotic prediction in both the A_1 and A_2 region with parameter values $m = 0.2$, $p \equiv \bar{p} = -23.8727$. In both (a) and (b), $A_1 = 1$, $A_2 = 2$, $s = 1.5$

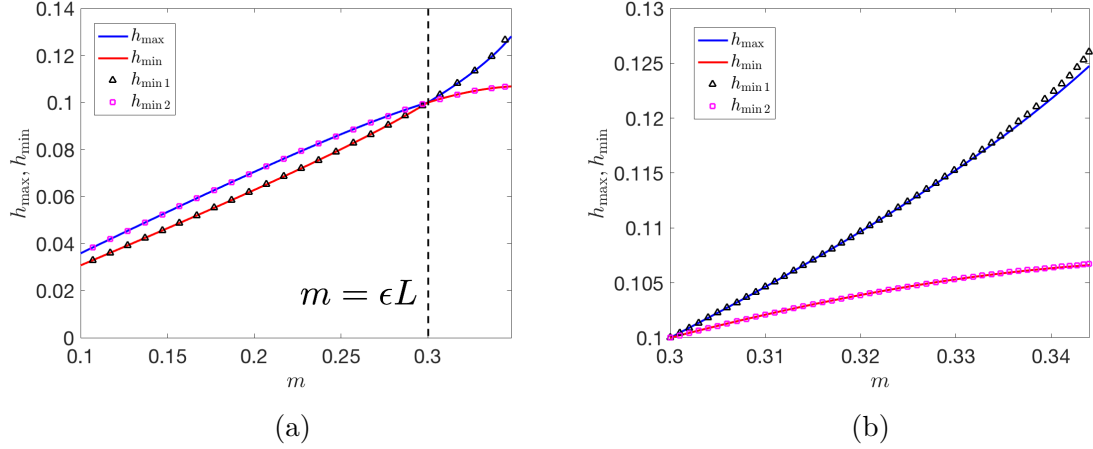


FIGURE 4.10: (a) Bifurcation diagram for m vs. h_{\max} , h_{\min} zoomed into the mass range $m \ll \epsilon L$. The solid curves represent numerically calculated bifurcation. The dotted curves represent the bifurcation calculated using asymptotic approximations given by $h_{\min 1}$ and $h_{\min 2}$. The dashed line represents $m = \epsilon L = 0.3$. (b) Same bifurcation diagram as (a), but zoomed into the mass range where m is slightly above ϵL . In both (a) and (b), $L = 3$, $A_1 = 1$, $A_2 = 2$, $s = 1.5$

mass falls below ϵL and continues to decrease, $h_{\min 1} < h_{\min 2}$. More fluid mass starts to concentrate on the A_2 region. In both Figure 4.9 (a) and (b), the boundary layer near $x = s$ can be well approximated by (4.20).

Figure 4.10 (a) shows the bifurcation diagram for mass vs. the corresponding maximum and minimum film thickness, zoomed into the mass range $m = O(\epsilon L)$. The solid blue curve and solid red curve represent the maximum and minimum film thickness determined from the numerical solution respectively. The triangle-dotted curve and square-dotted curve represent $h_{\min 1}$ and $h_{\min 2}$ calculated by solving $A_i \Pi(h_{\min i}) = \bar{p}$ respectively. Note that when $m = \epsilon$, $h(x) \equiv \epsilon$ is a flat film solution with $h_{\max} = h_{\min}$. For $h > \epsilon$, $\bar{p} > 0$. If $A_1 < A_2$, then $h_{\min 1} > h_{\min 2}$ so the maximum of the film thickness occurs at $x = 0$, i.e. the A_1 region. For $h < \epsilon$, $\bar{p} < 0$. If $A_1 < A_2$, then $h_{\min 1} < h_{\min 2}$, in which case the maximum film thickness occurs at $x = L$. Figure 4.10 (b) zooms in to the mass $m > \epsilon L$. As mass continues to increase, the leading order approximation becomes less accurate, which is expected from the derivation of (4.20), which assumes the solution is a small perturbation from $h = h_{\min i}$.

4.2.2 Large-thickness films

In Section 4.2.1, we studied small-mass small-thickness solutions for $p \rightarrow 0$. In the limit $\bar{p} \rightarrow 0^+$, there exists another class of solutions, characterized by large mean film thickness and large mass, which corresponds to branch 6 labeled in Figure 4.6 (b). Unlike small-thickness solution characterized by a boundary layer near $x = s$, whose profile approaches a step function in the limit $\epsilon \rightarrow 0$, this class of thick solutions has small amplitude deviations from the mean film thickness and slowly-varying derivative. An example of a steady-state profile on this branch is shown in Figure 4.11.

Specifically, for this type of solutions, as $\bar{p} \rightarrow 0^+$, $m \rightarrow \infty$ and $h_{\max} - h_{\min} \ll \frac{m}{L}$.

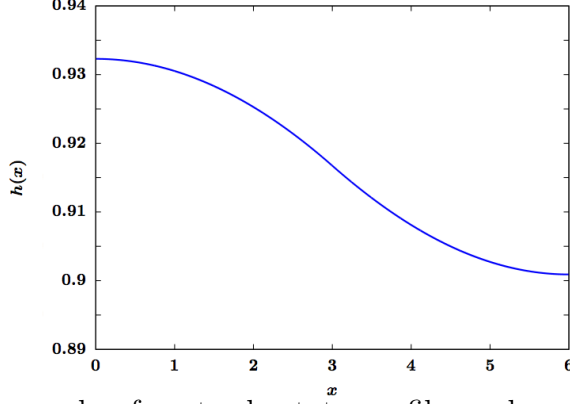


FIGURE 4.11: An example of a steady-state profile on branch 6 with parameter values $A_1 = 1$, $A_2 = 1.5$, $L = 6$, $s = 3$, $\epsilon = 0.1$. $m = 5.5$, and $p = 0.014564$.

It follows that in the limit $\bar{p} \rightarrow 0$, $\Pi\left(\frac{m}{L}\right) \rightarrow 0$. Compared to the small-thickness solutions, films with large mass is influenced by weaker intermolecular force and thus weaker impact of the heterogeneity contrast across $x = s$. To approximate this class of solutions, we choose $\delta = \Pi\left(\frac{m}{L}\right) \ll 1$ to be a small parameter in our asymptotic expansion. We write the solution as $h(x) = \bar{h} + \delta h_1(x)$ for $\bar{h} = \frac{m}{L}$. Substituting this expansion into the full steady-state equation and linearizing around $h(x) = \bar{h}$, at $O(\delta)$, on the A_i region, we have

$$\delta h_{1xx} = A_1 \delta - \bar{p} + \delta A_1 \Pi'(\bar{h}) h_1, \quad h_{1x}(0) = 0, \quad 0 < x \leq s \quad (4.29a)$$

$$\delta h_{1xx} = A_2 \delta - \bar{p} + \delta A_2 \Pi'(\bar{h}) h_1, \quad h_{1x}(L) = 0, \quad s < x < L \quad (4.29b)$$

To balance the equation at $O(\delta)$, we choose $\bar{p} = O(\delta)$ by writing $\bar{p} = \delta p_0$ for some $p_0 = O(1)$. As $m \rightarrow \infty$, $\Pi'(\bar{h}) < 0$. Solving for $h_1(x)$ on $0 \leq x \leq s$ and $s < x \leq L$ respectively, we obtain

$$h(x) \sim \begin{cases} \bar{h} + C_1 \cos(\sqrt{-A_1 \Pi'(\bar{h})} x) - \frac{A_1 - p_0}{A_1 \Pi'(\bar{h})} \Pi(\bar{h}) & 0 \leq x \leq s \\ \bar{h} + C_2 \cos(\sqrt{-A_2 \Pi'(\bar{h})} (-x + L)) - \frac{A_2 - p_0}{A_2 \Pi'(\bar{h})} \Pi(\bar{h}) & s < x \leq L \end{cases} \quad (4.30)$$

for some constant C_1 and C_2 . To determine C_1 and C_2 , we use the same condition given by (4.8a) and (4.8b). C_1 and C_2 are both linear in p with $C_1 = p_0 \tilde{C}_1$ and

$C_2 = p_0 \tilde{C}_2$ where

$$\tilde{C}_1 = \frac{(A_1 - A_2) r_2 \sin(r_2 (-s + L))}{A_1 A_2 \Pi'(\bar{h}) (\sin(r_1 s) \cos(r_2 (-s + L)) r_1 + \sin(r_2 (-s + L)) \cos(r_1 s) r_2)} \quad (4.31)$$

$$\tilde{C}_2 = \frac{-\sin(r_1 s) r_1 (A_1 - A_2)}{A_1 A_2 \Pi'(\bar{h}) (\sin(r_1 s) \cos(r_2 (-s + L)) r_1 + \sin(r_2 (-s + L)) \cos(r_1 s) r_2)} \quad (4.32)$$

Here, $r_i = \sqrt{-A_i \Pi'(\bar{h})}$. Note that an alternative choice of small parameter in writing out the asymptotic expansion is $\bar{p} = \delta \ll 1$. However, if we use $\bar{p} = \delta \ll 1$ as the small parameter in our expansion, we would need to solve the nonlinear equation $\Pi(\bar{h}) = \bar{p}$ for \bar{h} to obtain the leading order term to calculate mass m . The advantage of using $\delta = \Pi\left(\frac{m}{L}\right)$ as our small parameter is that given a film mass m , we can use the mass condition $\int_0^L h_1(x) dx = 0$ to directly solve for the corresponding pressure $\bar{p} = \delta p_0$ through a linear equation since C_i 's are both linear in p_0 . Direct analytical calculations show that the pressure \bar{p} is given by

$$\bar{p} \sim \frac{\Pi(\bar{h})L}{\frac{s}{A_1} + \frac{L-s}{A_2} + \frac{\tilde{C}_1 \Pi'(\bar{h})}{r_1} \sin(r_1 s) + \frac{\tilde{C}_2 \Pi'(\bar{h})}{r_2} \sin(r_2 (L - s))} \quad (4.33)$$

Figure 4.12 shows an example of a thick steady-state film with small pressure. The pressure of the film is given by $\bar{p} = 0.0192$. The solid blue curve represents the numerical solution. The dotted red curve and the dotted black curve represent the solution computed asymptotically using (4.30) on $[0, s]$ and $[s, L]$ respectively. Specifically, the constant C_1 and C_2 are computed using (4.31), (4.32) and (4.33). The numerical simulation results indicate that (4.30) agrees very well with the numerical solution. To simplify (4.33) further, we derive an asymptotic expansion for

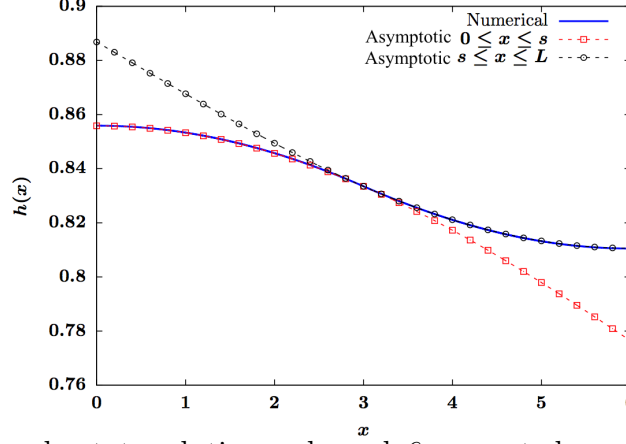


FIGURE 4.12: A steady-state solution on branch 6 computed numerically and asymptotically as described above, with parameter values $\bar{p} = 0.0192$, $A_1 = 1$, $A_2 = 1.5$, $L = 6, s = 3$, $\epsilon = 0.1$

\bar{p} in the limit of large mass. In the limit of large \bar{h} , we have

$$\begin{aligned}
 \bar{p} &= \frac{A_1 s + A_2(L-s)}{L\bar{h}^3} \Pi(\bar{h}) + O\left(\frac{\epsilon^3}{\bar{h}^4}\right) \\
 &= \frac{\epsilon^2(A_1 s + A_2(L-s))}{L\bar{h}^3} + O\left(\frac{\epsilon^3}{\bar{h}^4}\right) \\
 &= \frac{\epsilon^2(A_1 s + A_2(L-s))L^2}{m^3} + O\left(\frac{\epsilon^3}{m^4}\right)
 \end{aligned} \tag{4.34}$$

This suggests that \bar{p} is inversely proportional to m^3 for large mass. For fixed large mass, \bar{p} scales linearly with both A_1 and A_2 . From (4.30), we can also derive an asymptotic expansion of $h(0)$ and $h(L)$, which are the maximum and minimum thickness of the film. Note that in the limit of large \bar{h} , $h(0) - \bar{h}$ and $h(L) - \bar{h}$ are asymptotically given by (4.35a) and (4.35b).

$$h(0) - \bar{h} \sim C_1 - \frac{A_1 - p_0}{A_1 \Pi'(\bar{h})} \Pi(\bar{h}) = -\frac{1}{6} \frac{s(L-s)(2L-s)(A_1 - A_2)\epsilon^2}{L\bar{h}^3} + O\left(\frac{\epsilon^3}{\bar{h}^4}\right) \tag{4.35a}$$

$$h(L) - \bar{h} \sim C_2 - \frac{A_2 - p_0}{A_2 \Pi'(\bar{h})} \Pi(\bar{h}) = \frac{1}{6} \frac{s(L-s)(L+s)(A_1 - A_2)\epsilon^2}{L\bar{h}^3} + O\left(\frac{\epsilon^3}{\bar{h}^4}\right) \tag{4.35b}$$

Figure 4.13 shows m as a function of \bar{p} for $\epsilon = 0.001, 0.01, 0.1$ computed numerically and asymptotically using (4.34), which is a further reduced asymptotic prediction from the full asymptotic prediction given by (4.33). The solid curves represent the numerically computed bifurcation curves. The blue, red and black curve correspond to $\epsilon = 0.001$, $\epsilon = 0.01$ and $\epsilon = 0.1$ respectively. The orange dotted curve with filled squares, the green dotted curve with empty circles and the purple dotted curve with empty squares represent the asymptotic predictions given by (4.34) for $\epsilon = 0.001$, $\epsilon = 0.01$ and $\epsilon = 0.1$ respectively. This figure shows that the large m asymptotic results given by (4.34) agree well with the numerical results for $\epsilon = 0.001$ and $\epsilon = 0.01$. For $\epsilon = 0.1$, the further reduced asymptotic approximation (4.34), denoted by dashed and dotted curve with empty squares, is slightly less accurate. This can be explained by the dependence of the remainder term on ϵ . Note that the remainder term in (4.34) is $O\left(\frac{\epsilon^3}{L^4}\right)$. However, for $\epsilon = 0.1$, the full asymptotic description given by (4.33), denoted in the figure as “full asymptotic”, is still capable of producing a good approximation of the numerical results.

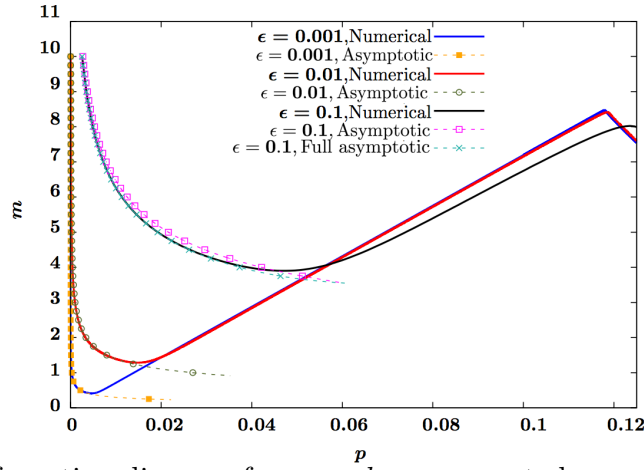


FIGURE 4.13: Bifurcation diagram for p vs. h_{\max} computed numerically and asymptotically for $\epsilon = 0.001, 0.01, 0.1$. In all our simulations, we set $A_1 = 1$, $A_2 = 1.5$, $L = 6$, $s = 3$.

4.2.3 Small-width droplets

In this subsection, we study the solutions on branch 2, which is a branch that folds back from branch 1. These solutions are of droplet-type where the droplet core completely resides in the A_1 region $x \in [0, s]$. Compared to the solutions on branch 1 which are thin, nearly flat film in the outer A_1 and A_2 regions with a boundary layer near $x = s$, solutions on branch 2 are characterized by larger mass so that droplets could form on the A_1 region, but are not so large as to form large droplets with widths $w \geq s$. This class of solutions have the smallest possible mass that allows droplets centered at $x = 0$ to form.

For a droplet with its core completely inside of $[0, s]$, the profile decays to an ultra-thin film region with film thickness $h = O(\epsilon)$ for $x < s$. The tail of the droplet on the A_1 region extends to the interface of the A_1 and A_2 region, where a boundary layer occurs near $x = s$, similar to that observed in the small-thickness solutions on branch 1. An example of this type of solutions is shown below in Figure 4.14.

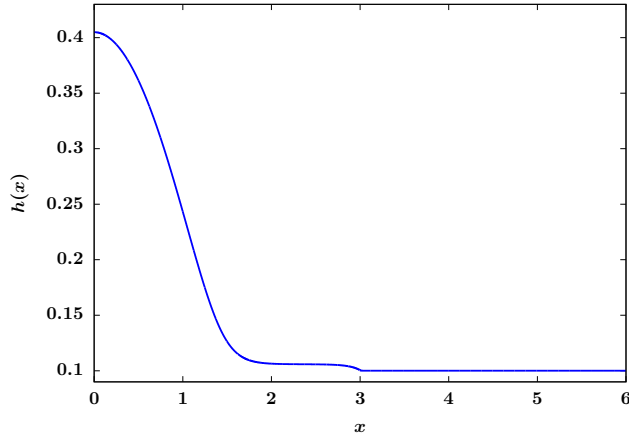


FIGURE 4.14: Profile of a steady-state on branch 2, characterized by a droplet on $[0, s]$ and ultra-thin film on $[s, L]$. A boundary layer where thickness changes rapidly is observed near the interface of the A_1 and A_2 region.

Here, we discuss the asymptotic approximation of such solutions in two limits, in the limit $A_2 \rightarrow \infty$ and $\epsilon \rightarrow 0$ respectively. We will show that in both limits, the

droplet profile on the A_1 region falls below $h(x) = h_{\min 1}$ at some $x \leq s$, where $h_{\min 1}$ is the saddle point given by $A_1 \Pi(h_{\min 1}) = \bar{p}$. Specifically, we use a width formulation similar to that presented in (3.15) in Section 3.1.1 to study the properties of branch 2 solutions. For $A(x) = A_1$, (3.15) is given by

$$\frac{1}{2} \left(\frac{dh}{dx} \right)^2 = A_1 U(h) - \bar{p}h + C \quad (4.36)$$

To determine C , we apply the boundary condition $h(0) = h_{\max}$, which yields

$$C = -A_1 U(h_{\max}) + \bar{p}h_{\max} \quad (4.37)$$

Together, the steady-state equation for a monotone decreasing profile on $[0, s]$ can be described by

$$\frac{dh}{dx} = -\sqrt{2R(h)} \quad (4.38)$$

where

$$R(h) = A_1 U(h) - \bar{p}h - (A_1 U(h_{\max}) - \bar{p}h_{\max}) \quad (4.39)$$

If $h(x_1) = h_1$ and $h(x_2) = h_2$, then by (4.38), we have

$$x_2 - x_1 = \int_{h_1}^{h_2} \frac{dh}{\sqrt{2R(h)}} \quad (4.40)$$

Since $h(x)$ falls below $h_{\min 1}$ for some $x \leq s$, then using (4.40), we can describe solutions on branch 2 by the property

$$\int_{h_{\min 1}}^{h_{\max}} \frac{1}{\sqrt{2R(h)}} dh < s \quad (4.41)$$

Figure 4.15 (a) shows the homoclinic orbit for $A(x) \equiv A_1 = 1$ and $A(x) \equiv A_2 = 2$ respectively and h vs. h_x plotted for a chosen steady-state solution on branch 2. The blue dotted curve denotes the homoclinic orbit on $A(x) \equiv A_1 = 1$. The red

dotted curve denotes the homoclinic orbit on $A(x) \equiv A_2 = 2$. The black solid curve denotes the orbit for the chosen steady-state solution on branch 2. Figure 4.15 (b) is the same plot shown in (a) zoomed into the range $h \in (h_{\min 2}, h_{\min 1})$. For $A_2 > A_1$, we have $h_{\min 1} > h_{\min 2}$, $h_{\text{cen}2} > h_{\text{cen}1}$ and $h_{\max 2} > h_{\max 1}$ where $h_{\text{cen}i}$ denotes the center-fixed point for $A(x) \equiv A_i$. Since the steady-state solution exists on a finite domain $[0, L]$, the minimum film thickness satisfies $h_{\min} > h_{\min 2}$. We will show that in the limit $A_2 \rightarrow \infty$ and $\epsilon \rightarrow 0$, $h_{\min} \rightarrow \epsilon$ to leading order. Hence, in these two limits, the steady-state solution on the A_1 region must lie outside of the homoclinic orbit for $A(x) \equiv A_1$ and inside the homoclinic orbit for $A(x) \equiv A_2$.

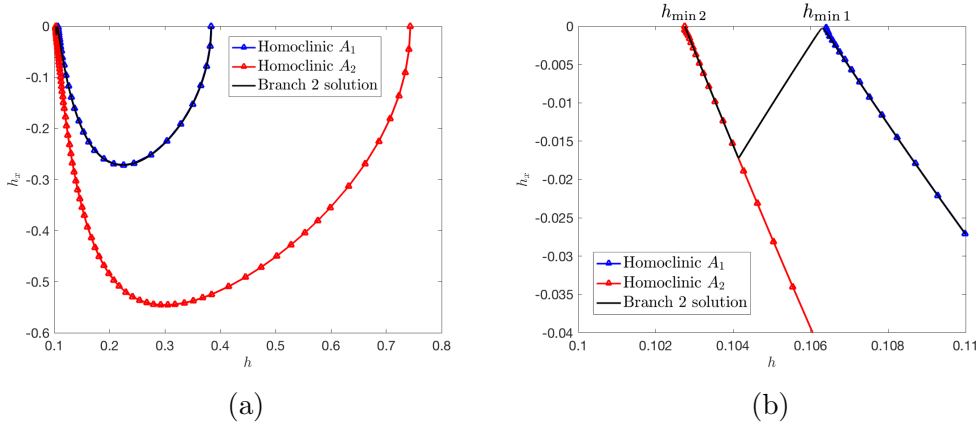


FIGURE 4.15: (a) Homoclinic orbit for $A(x) \equiv A_1$ and $A(x) \equiv A_2$ respectively and the orbit of a branch 2 solution. (b) Same phase plane plot zoomed into $h \in (h_{\min 2}, h_{\min 1})$, for parameter values $A_1 = 1$, $A_2 = 2$, $L = 6$, $s = 3$, $\bar{p} = 0.493$, $\epsilon = 0.1$

First, we study the steady-state in the limit $A_2 \rightarrow \infty$ for $A_1 = 1$ fixed. On the A_2 region, the steady-state equation is given by

$$\frac{d^2 h}{dx^2} = A_2 \Pi(h) - \bar{p} \quad (4.42)$$

To study the limit $A_2 \rightarrow \infty$, write $A_2 = \frac{1}{\delta}$ for some $\delta \ll 1$. Then we have

$$\delta \frac{d^2 h}{dx^2} = \Pi(h) - \delta \bar{p} \quad (4.43)$$

(4.43) is a problem with a boundary layer near $x \sim s$. We write the outer solution as $h^{out}(x) = h_0^{out}(x) + \delta h_1^{out}(x) + H.O.T.$ At $O(1)$, $\Pi(h_0^{out}) = 0$, so $h_0^{out} = \epsilon$. At $O(\delta)$, we have

$$\frac{d^2 h_0^{out}}{dx^2} + \bar{p} = \Pi'(\epsilon) h_1 \quad (4.44)$$

so $h_1^{out} = \epsilon^2 \bar{p}$. Hence, the outer solution $h^{out}(x)$ is given by

$$h^{out}(x) \sim \epsilon + \delta \epsilon^2 \bar{p} = \epsilon + \frac{1}{A_2} \epsilon^2 \bar{p} \quad (4.45)$$

Next, we seek the inner solution of the form $h^{in}(X) = h_0^{in}(X) + \sigma h_1^{in}(X) + \sigma^2 h_2^{in}(X) + H.O.T.$ for $X = \frac{x-s}{\delta^a}$ for some $a > 0$ and $\sigma \ll 1$. In the rescaled variable, the steady-state equation for $h(x)$ on $[s, L]$ is given by

$$\delta^{1-2a} \frac{d^2 h^{in}}{dX^2} = \Pi(h^{in}) - \bar{p} \delta \quad (4.46)$$

Choose $a = \frac{1}{2}$. Then at leading order, we obtain

$$\frac{d^2 h_0^{in}}{dX^2} = \Pi(h_0^{in}) \quad (4.47)$$

We can write (4.47) as a first order equation by multiplying both sides by $\frac{dh_0^{in}}{dx}$ and integrating with respect to x . For a monotonically decreasing solution, we have

$$\frac{dh_0^{in}}{dX} = -\sqrt{2U(h_0^{in}) + C} \quad (4.48)$$

for some constant C . To match h_0^{in} with h_0^{out} , we need $h_0^{in}(X) \rightarrow \epsilon$ as $X \rightarrow \infty$. This determines $C = -2U(\epsilon)$. Since we expect $\lim_{x \rightarrow s^-} h(x) \rightarrow \epsilon$ in the limit $A_2 \rightarrow \infty$, we would like $h_0^{in}(0) = \epsilon$. This pins the solution $h_0^{in}(X)$ down to the constant solution $h_0^{in}(X) \equiv \epsilon$.

Now if we write $h(x)$ in terms of the original variable x , then for $x \rightarrow s^+$, $h'(x) \sim \sigma h_1'(x) \sim \frac{\sigma}{\sqrt{\delta}} h_1^{in'}(X) \sim O\left(\frac{\sigma}{\sqrt{\delta}}\right)$ since $h_0(x) \equiv \epsilon$ is a constant. For $0 \leq x < s$, the solution is characterized by a droplet structure. We expect $\lim_{x \rightarrow s^-} h'(x) = O(1)$. It follows from the balance $\lim_{x \rightarrow s^-} h'(x) = \lim_{x \rightarrow s^+} h'(x)$ that $\sigma = \sqrt{\delta}$. Hence, at $O(\sqrt{\delta})$, we obtain the equation for $h_1^{in}(X)$ given by

$$\frac{d^2 h_1^{in}}{dX^2} = \Pi'(h_0^{in}) h_1^{in}(X) = \frac{1}{\epsilon^2} h_1 \quad (4.49)$$

This gives

$$h_1^{in}(X) = E e^{\frac{X}{\epsilon}} + F e^{-\frac{X}{\epsilon}} \quad (4.50)$$

To match $h^{in}(X)$ with $h^{out}(x)$ at $O(\sqrt{\delta})$, we need $h_1^{in} \rightarrow 0$ as $X \rightarrow \infty$ since $h^{out}(x)$ does not have a $O(\sqrt{\delta})$ term in the expansion, so $E = 0$.

Next, at $O(\delta)$, the equation for $h_2^{in}(X)$ is given by

$$\frac{d^2 h_2^{in}}{dX^2} = \Pi'(h_0^{in}) h_2^{in} + \frac{1}{2} \Pi''(h_0^{in}) (h_1^{in})^2 - \bar{p} \quad (4.51)$$

The solution $h_2^{in}(X)$ is therefore given by

$$h_2^{in}(X) = C_2 e^{\frac{X}{\epsilon}} + C_1 e^{-\frac{X}{\epsilon}} + \frac{1}{6} \epsilon^2 \left(6\bar{p} + F^2 \Pi''(h_0) e^{-\frac{2X}{\epsilon}} \right) \quad (4.52)$$

To match the inner solution with the outer solution at $O(\delta)$, we require $h_2 \rightarrow \epsilon^2 \bar{p}$ as $X \rightarrow \infty$. This gives $C_2 = 0$. Together, on the A_2 region $s \leq x \leq L$, in the limit of large A_2 ,

$$h(x) \sim \epsilon + \sqrt{\delta} F e^{-\frac{(x-s)}{\epsilon\sqrt{\delta}}} + \delta \left(\epsilon^2 \bar{p} + C_1 e^{-\frac{x-s}{\epsilon\sqrt{\delta}}} + \frac{1}{6} \epsilon^2 F^2 \Pi''(\epsilon) e^{-\frac{2}{\epsilon} \frac{(x-s)}{\sqrt{\delta}}} \right) \quad (4.53)$$

Up to $O(\sqrt{\delta})$, $h(s) \sim \epsilon + \sqrt{\delta}F + O(\delta)$. For a given pressure \bar{p} , in the limit $A_2 \rightarrow \infty$, $h(s) \rightarrow \epsilon < h_{\min 1}$. By continuity of $h(x)$, $\lim_{x \rightarrow s^-} h(x) \rightarrow \epsilon < h_{\min 1}$. It follows that in the phase plane, the steady-state solution on the A_1 region must be a solution that lies outside of the homoclinic orbit that corresponds to $A(x) \equiv A_1$.

To determine F , we consider the solution on the A_1 region. In the limit $A_2 \rightarrow \infty$, $h(s) \rightarrow \epsilon$. To leading order, the steady-state problem on A_1 region is given by the Dirichlet problem

$$\frac{d^2 h}{dx^2} = A_1 \Pi(h) - \bar{p} \quad (4.54a)$$

$$h'(0) = 0, \quad h(s) = \epsilon \quad (4.54b)$$

Since the solution on A_1 region lies outside of the homoclinic orbit, there exists $x_f < s$ such that $h(x_f) = h_{\min 1}$, at which $h'(x)$ has a local extremum, implying that $h(x)$ has a concavity change. Since $h_{\min 1} = \epsilon + O(\epsilon^2)$, we approximate the solution in the region where $\epsilon + \sqrt{\delta}F < h(x) < h_{\min 1}$ by

$$h(x) = h_{\min 1} + \tilde{\delta} h_1(x)$$

for some $\tilde{\delta} \ll h_{\min 1}$, to be determined later. Substituting the expansion into (4.54a) and linearizing, at $O(\tilde{\delta})$, we have

$$\frac{d^2 h_1}{dx^2} = A_1 \Pi'(h_{\min 1}) h_1 \quad (4.55)$$

Solving (4.55) for h_1 , we obtain the asymptotic expansion for $h(x)$, given by

$$h(x) \sim h_{\min 1} + G e^{\sqrt{A_1 \Pi'(h_{\min 1})}(x-s)} + H e^{-\sqrt{A_1 \Pi'(h_{\min 1})}(x-s)} \quad (4.56)$$

for some constant G and H to be determined. Note that $\sqrt{\Pi'(h_{\min 1})} = O\left(\frac{1}{\epsilon}\right)$. $h(x)$ has a boundary layer as $x \rightarrow s$. For the inner solution to match the outer solution as

$x \rightarrow -\infty$, $H = 0$. To determine F , we apply the condition (4.8a)-(4.8b). This gives

$$G = \frac{\epsilon - h_{\min 1}}{\epsilon \sqrt{\delta} \sqrt{A_1 \Pi'(h_{\min 1})} + 1} \quad (4.57a)$$

$$F = \frac{\epsilon \sqrt{A_1 \Pi'(h_{\min 1})} (h_{\min 1} - \epsilon)}{\epsilon \sqrt{\delta} \sqrt{A_1 \Pi'(h_{\min 1})} + 1} \quad (4.57b)$$

Hence, $G = O(\epsilon^2) \ll h_{\min 1}$. It follows that $h'(s) \sim G \sqrt{A_1 \Pi'(h_{\min 1})} \sim -\epsilon \bar{p}$. The steady-state equation on A_1 region can be written as a first order equation given by

$$\frac{1}{2} \left(\frac{dh}{dx} \right)^2 = A_1 U(h) - \bar{p}h + K \quad (4.58)$$

for some constant K . Plugging $h'(s) \sim -\epsilon \bar{p}$ and $h(s) \sim \epsilon + \sqrt{\delta} F$ into (4.58), we find

$$K = \frac{1}{2} G^2 A_1 \Pi'(h_{\min 1}) - A_1 U(\epsilon + \sqrt{\delta} F) + \bar{p}(\epsilon + \sqrt{\delta} F) \quad (4.59)$$

If we take $\epsilon \rightarrow 0$, to leading order, we have

$$F \sim \frac{\epsilon^2 \bar{p}}{\sqrt{A_1}} \quad (4.60)$$

and thus,

$$h(s) \sim \epsilon + \sqrt{\delta} \frac{\epsilon^2 \bar{p}}{\sqrt{A_1}} \quad (4.61)$$

In the same limit, at $h(x_f) = h_{\min 1}$,

$$\frac{1}{2} h'(x_f)^2 = A_1 U(h_{\min 1}) - \bar{p} h_{\min 1} + \frac{1}{2} G^2 A_1 \Pi'(h_{\min 1}) - A_1 U(\epsilon + \sqrt{\delta} F) + \bar{p}(\epsilon + \sqrt{\delta} F) \quad (4.62a)$$

$$\sim \frac{\epsilon^2 \bar{p}^2}{\sqrt{A_1}} \sqrt{\delta} - \frac{1}{2} \epsilon^2 \bar{p}^2 \delta \quad (4.62b)$$

Hence, as $A_2 \rightarrow \infty$, $h'(x_f) \rightarrow 0$, suggesting that the droplet formed on $[0, s]$ approaches the homoclinic orbit corresponding to $A(x) \equiv A_1$ and therefore can be

approximated by the homoclinic solution in the limit of large A_2 to leading order. Figure 4.16 (a)-(b) shows the profile of one steady-state solution that belongs to branch 2 for $A_2 = 50$. Figure 4.16 (a) shows a comparison of the homoclinic droplet on $A(x) \equiv A_1$ and the steady-state solution on heterogeneous $A(x)$ with the same pressure. This shows that the droplet core of branch 2 solutions can be well approximated by the homoclinic solution on the region with $A(x) \equiv A_1$ of the same pressure. Figure 4.16 (b) shows the boundary layer approximation compared to the numerical solution for the same branch 2 solution zoomed into the interface of A_1 and A_2 region. We conclude that the droplet portion of the branch 2 solutions depends on A_1 to leading order.

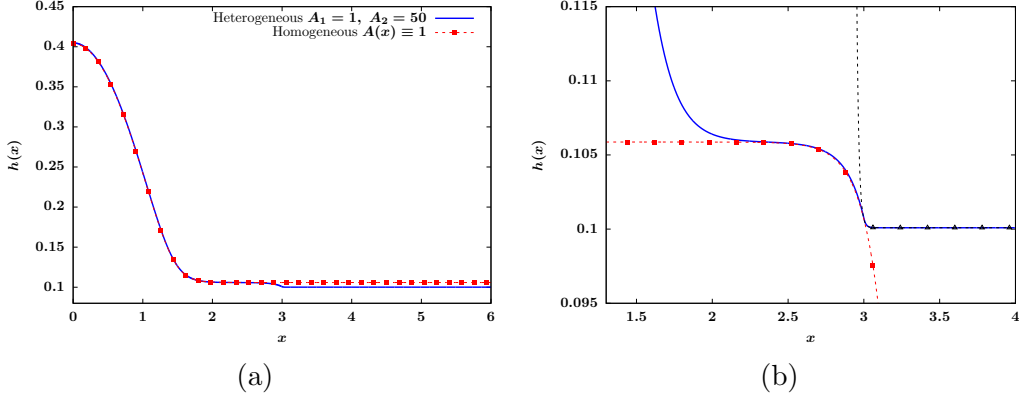


FIGURE 4.16: (a) Comparison of a branch 2 steady-state on a heterogeneous substrate with the homoclinic solution on $A(x) \equiv A_1$ for the same pressure. The solid blue curve represents the numerically computed steady-state. The dotted red curve represents the homoclinic solution with the same pressure on a homogeneous substrate $A(x) \equiv A_1$. (b) Comparison of the numerically computed steady-state and the boundary layer approximation near the interface $x = s$. The solid blue curve represents the numerically computed solution. The dotted red curve represents the asymptotic approximation near the interface. In both (a) and (b), $L = 6$, $s = 3$, $A_1 = 1$, $A_2 = 50$, $\epsilon = 0.1$, $\bar{p} = 0.467332$.

Now, instead of taking $A_2 \rightarrow \infty$ for fixed A_1 and ϵ , we consider the same steady-state equation in the limit $\epsilon \rightarrow 0$ for fixed $A_1, A_2 = O(1)$. For the same droplet-type solution where the droplet resides completely in the A_1 region with width $w < s$, the

film thickness decays to $O(\epsilon)$ as $x \rightarrow s$. Since the solution should be monotonically decreasing, the film thickness on $[s, L]$ is $O(\epsilon)$. In the limit $\epsilon \rightarrow 0$, $\Pi(h)$ changes rapidly near $h = O(\epsilon)$. It follows that the solution for $s \leq x \leq L$ and $w \ll x < s$ can be asymptotically approximated by (4.20) where C_1 and C_2 are given by (4.22a)-(4.22b), as derived in Section 4.2.1 for small-thickness films. This gives

$$h(s) \sim h_{\min 2} + \frac{(h_{\min 1} - h_{\min 2})\sqrt{A_1\Pi'(h_{\min 1})}}{\sqrt{A_1\Pi'(h_{\min 1})} + \sqrt{A_2\Pi'(h_{\min 2})}} \quad (4.63)$$

In the limit $\epsilon \rightarrow 0$, we can further reduce C_2 asymptotically so

$$C_2 \sim \frac{h_{\min 1} - h_{\min 2}}{\sqrt{\frac{A_2}{A_1}} + 1}$$

which has been described in (4.25a)-(4.25b) for small-thickness solution in the same

limit. Using $h_{\min 2} = \epsilon + \frac{\epsilon^2 \bar{p}}{A_2} + O(\epsilon^3)$, we have

$$h(s) \sim \epsilon + \epsilon^2 \frac{\bar{p}}{\sqrt{A_1 A_2}} \quad (4.64)$$

Note that that in the limit $A_2 \rightarrow \infty$, (4.64) is the same as (4.61) derived earlier by first taking $A_2 \rightarrow \infty$ and then $\epsilon \rightarrow 0$.

To get an estimate of the maximum film thickness of this class of solutions in the limit $\epsilon \rightarrow 0$, we first write the steady-state equation as a first order equation on $[0, s]$, given by

$$\frac{1}{2} \left(\frac{dh}{dx} \right)^2 = A_1 U(h) - \bar{p}h + M \quad (4.65)$$

for some constant M . By applying the boundary condition $h_x(0) = 0$ and $h(0) = h_{\max}$, we have

$$M = -A_1 U(h_{\max}) + \bar{p}h_{\max} \quad (4.66)$$

Writing the steady-state equation on $s < x \leq L$ as a first order equation, we have

$$\frac{1}{2}h_x^2 = A_2U(h) - \bar{p}h + P \quad (4.67)$$

for some constant P . Applying the boundary condition $h_x(L) = 0$ and $h(L) = h_{\min}$, we get

$$P = -A_2U(h_{\min}) + \bar{p}h_{\min} \quad (4.68)$$

Since $h'(x)$ is continuous at $x = s$, we have $\lim_{x \rightarrow s^-} h'(x) = \lim_{x \rightarrow s^+} h'(x)$. This gives

$$(A_1 - A_2)U(h(s)) + \bar{p}(h_{\max} - h_{\min}) = A_1U(h_{\max}) - A_2U(h_{\min}) \quad (4.69)$$

As $\epsilon \rightarrow 0$, $h(s) = \epsilon + O(\epsilon^2)$, $h_{\min} = \epsilon + O(\epsilon^2)$ and $U(h_{\max}) = O(\epsilon^2)$. At $O(1)$, we have

$$A_1U(h(s)) + \bar{p}(h_{\max} - h_{\min}) = 0 \quad (4.70)$$

It follows that the maximum film thickness is given by

$$h_{\max} \sim -\frac{A_1U(\epsilon)}{\bar{p}} + \epsilon \sim \frac{A_1}{6\bar{p}} \quad (4.71)$$

in the limit $\epsilon \rightarrow 0$. Note that $h_{\max} \sim \frac{A_1}{6\bar{p}}$ is the leading order asymptotic approximation of the maximum film thickness of the homoclinic solution on $A \equiv A_1$ with pressure \bar{p} . This is consistent with our earlier results on the steady-state solution in the limit $A_2 \rightarrow \infty$. Hence, the homoclinic solution on the homogeneous substrate $A(x) \equiv A_1$ can be used to describe the droplet portion of the branch 2 solution in both the limit $A_2 \rightarrow \infty$ and $\epsilon \rightarrow 0$. Specifically, as $\epsilon \rightarrow 0$, we can approximate the droplet core using the parabola $h(x) \sim -\frac{1}{2}\bar{p}x^2 + h_{\max}$. With $h_{\max} \sim \frac{A_1}{6\bar{p}}$, we have $w \sim \frac{\sqrt{A_1}}{\sqrt{3\bar{p}}}$. On branch 2, the maximum film thickness h_{\max} and droplet width w increase as \bar{p} decreases. It follows that in the limit $\epsilon \rightarrow 0$, branch 2 solutions terminate

at pressure $p_{2,3}^*$ when $w(p_{2,3}^*) \sim s$. Note that $p_{2,3}^*$ is also the pressure where branch 2 intersects with branch 3, to be discussed in Section 4.2.4 shortly. Asymptotically,

$$\frac{\sqrt{A_1}}{\sqrt{3}p_{2,3}^*} \sim s \quad (4.72)$$

which gives $p_{2,3}^* \sim \frac{\sqrt{A_1}}{\sqrt{3}s}$. Figure 4.17 shows the bifurcation diagram for h_{\max} vs. p zoomed into a portion of branch 2, computed numerically and asymptotically in the limit of small ϵ . The asymptotic prediction is computed using (4.71), which is represented by the red dotted curve. The simulation results show that the leading order asymptotic prediction agrees well with the numerical solution.

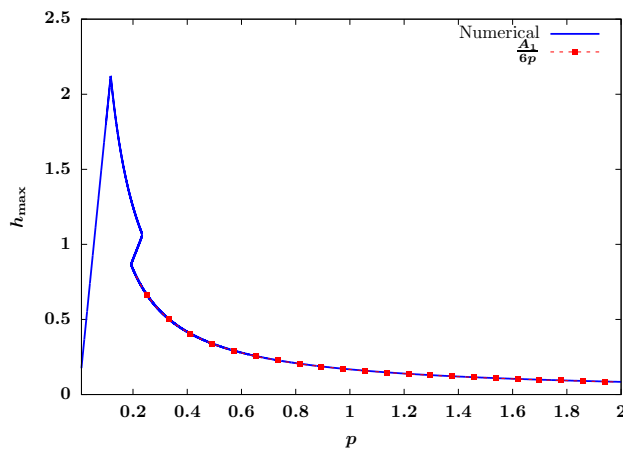


FIGURE 4.17: Bifurcation diagram for p vs. h_{\max} of steady-states on branch 2. The solid blue curve represents the numerical solution. The red dotted curve represents the asymptotic prediction of h_{\max} in the limit $\epsilon \rightarrow 0$, with parameters $A_1 = 1$, $A_2 = 1.5$, $L = 6$, $s = 3$, and $\epsilon = 0.001$.

4.2.4 Pinned droplets

On branch 2, the droplets formed have width $w < s$. Now we describe a new class of solutions, which corresponds to branch 3 labeled in Figure 4.6 (b), a branch that connects with branch 2 at pressure p^* where $w(p^*) \sim s$. As $\epsilon \rightarrow 0$, we have shown in Section 4.2.3 that $p^* \sim \frac{\sqrt{A_1}}{\sqrt{3}s}$. This branch of solutions is characterized by droplets

with width $w \sim s$. An example of such a solution is shown in Figure 4.18. In other words, this is a class of droplets where the droplet width does not change with droplet mass and size at leading order. The motion of the droplet is constrained by the strength of chemical heterogeneity at the interface of the solid substrate. This branch arises as a consequence of the heterogeneity introduced in the chemical properties of the substrate. To study and develop an asymptotic prediction for this type of solutions, we consider the steady-state in two separate limits, namely the limit $\epsilon \rightarrow 0$ and the limit $A_2 \rightarrow \infty$ respectively.

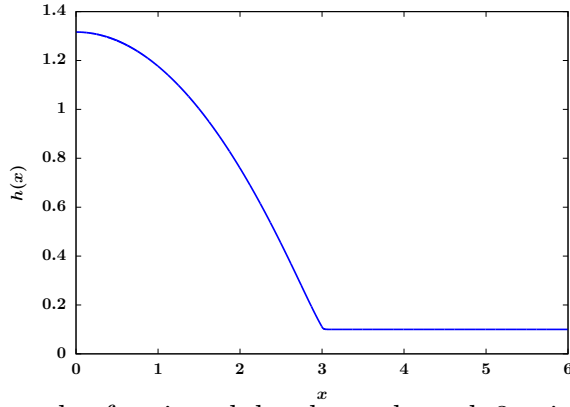


FIGURE 4.18: An example of a pinned droplet on branch 3, with parameters $A_1 = 1$, $A_2 = 50$, $L = 6$, $s = 3$, $\epsilon = 0.1$.

First, we study the solution in the limit $\epsilon \rightarrow 0$ for fixed $A_1, A_2 = O(1)$. As $\epsilon \rightarrow 0$, solutions on this branch are characterized by a droplet on $[0, s]$ with width $w \sim s$, $h_{\max} = O(1)$, $h(s) = O(\epsilon)$ and $h_{\min} = O(\epsilon)$. Hence, in the droplet core region, for $0 \leq x \ll s$, $A_1 \Pi(h) \ll 1$. At leading order, the steady-state equation can be described by $h'' \sim -\bar{p}$. It follows that the steady-state profile on $[0, s]$ is described by

$$h(x) \sim -\frac{1}{2}\bar{p}x^2 + h_{\max}$$

in the limit $\epsilon \rightarrow 0$. Since the droplet has width $w \sim s$, to leading order, the maximum

film thickness of the solution is given by

$$h_{\max} \sim \frac{1}{2} \bar{p} s^2 \quad (4.73)$$

Now we follow the equation (4.69) derived in Section 4.2.3, which is exact for all steady-states, given by

$$(A_1 - A_2)U(h(s)) + \bar{p}(h_{\max} - h_{\min}) = A_1 U(h_{\max}) - A_2 U(h_{\min})$$

In the limit $\epsilon \rightarrow 0$, $h_{\max} = O(1)$, $h(s) = O(\epsilon)$ and $h_{\min} = O(\epsilon)$. At $O(1)$, this equation reduces to

$$(A_1 - A_2)U(h(s)) + \bar{p}h_{\max} = -A_2 U(h_{\min}) \quad (4.74)$$

This produces a leading order asymptotic approximation for $h(s)$, given by

$$U(h(s)) = \frac{\frac{A_2}{6} - \frac{1}{2}\bar{p}^2 s^2}{A_1 - A_2} \quad (4.75)$$

Note that (4.75) reduces to a cubic polynomial. We choose $h(s)$ to be the real positive root larger than ϵ so $h(s) > \epsilon$. Figure 4.19 shows a comparison between $h(s)$ computed numerically and $h(s)$ computed by solving the asymptotically reduced equation (4.75) for $A_2 = O(1)$. The simulation results show that the asymptotic prediction agrees well with the numerical results.

Next, we study the solution on branch 3 in the limit $A_2 \rightarrow \infty$. Let $\delta = \frac{1}{A_2} \ll 1$. We follow the same derivation presented in (4.43)-(4.53) in Section 4.2.3. On the A_2 region, the solution can be asymptotically described by

$$h(x) \sim \epsilon + \sqrt{\delta} F e^{-\frac{(x-s)}{\epsilon\sqrt{\delta}}} + O(\delta) \quad (4.76)$$

for some constant F , which would be different from that in Section 4.2.3 since the solution on the A_1 region changes. We determine F so that $\lim_{x \rightarrow s^-} h(x) = \lim_{x \rightarrow s^+} h(x)$.

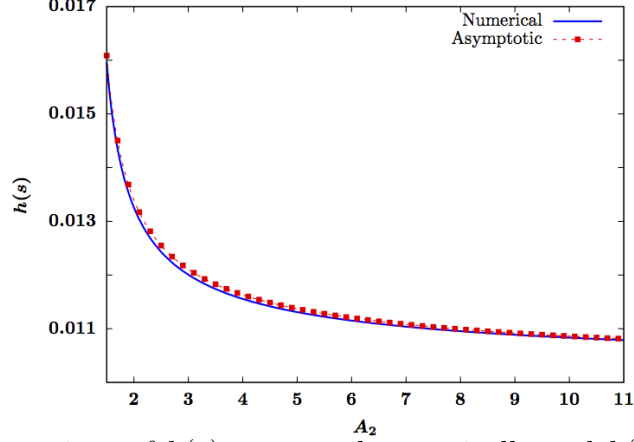


FIGURE 4.19: Comparison of $h(s)$ computed numerically and $h(s)$ computed using the asymptotic approximation (4.75) for a droplet on branch 3 with fixed pressure \bar{p} as $A_2 = O(1)$ increases. The solid blue curve denotes the numerical result. The red dashed curve represents the solution to the asymptotic prediction (4.75), with parameters $A_1 = 1$, $\bar{p} = 0.2075$, $L = 6$, $s = 3$, $\epsilon = 0.01$.

To determine $h(s)$ in the limit of large A_2 , we divide both sides of (4.69) by A_2 . We can rewrite (4.69) in terms of δ as

$$(\delta A_1 - 1)U(h(s)) + \delta \bar{p}(h_{\max} - h_{\min}) = \delta A_1 U(h_{\max}) - U(h_{\min}) \quad (4.77)$$

At $O(1)$, we have

$$U(h(s)) = U(h_{\min}) \quad (4.78)$$

In (4.43)-(4.53), we have derived that $h(s) = \epsilon + O(\sqrt{\delta})$ in the limit $A_2 \rightarrow \infty$ where the higher-order term in the expansion depends on the solution on $x \in [0, s)$. To obtain a higher-order prediction for $h(s)$ for branch 3 in the limit $A_2 \rightarrow \infty$, we write $h(s) = h_0 + \delta^a h_1$ for some $a > 0$. Here, the leading order term h_0 is given by ϵ by (4.78). The Taylor expansion of $U(\epsilon + \delta^a h_1)$ at $h = \epsilon$ yields

$$U(h(s)) = U(\epsilon + \delta^a h_1) \sim U(\epsilon) + \frac{1}{2} \delta^{2a} \Pi'(\epsilon) h_1^2 \quad (4.79)$$

At $O(\delta)$, we have

$$\frac{1}{2} \Pi'(\epsilon) h_1^2 \delta^{2a} = \delta(A_1 U(\epsilon) + \frac{1}{2} \bar{p}^2 s^2) \quad (4.80)$$

This suggests $a = \frac{1}{2}$. Solving (4.80), we have

$$h_1 = \sqrt{2\epsilon} \sqrt{A_1 U(\epsilon) + \frac{1}{2} \bar{p}^2 s^2} = \epsilon \sqrt{-\frac{A_1}{3} + \bar{p}^2 s^2} \quad (4.81)$$

Together, in the limit $A_2 \rightarrow \infty$, we have

$$h(s) \sim \epsilon + \delta h_1 = \epsilon + \frac{\epsilon}{\sqrt{A_2}} \sqrt{-\frac{A_1}{3} + \bar{p}^2 s^2} \quad (4.82)$$

It follows that for $\lim_{x \rightarrow s^-} h(x) = \lim_{x \rightarrow s^+} h(x)$ to hold, F is given by

$$F = \epsilon \sqrt{-\frac{A_1}{3} + \bar{p}^2 s^2} \quad (4.83)$$

Figure 4.20 shows $h(s) - \epsilon$ calculated numerically and asymptotically plotted in log scale. The asymptotic approximation used is given by (4.82). In the limit of large A_2 , the asymptotic prediction agrees well with the numerical solution.

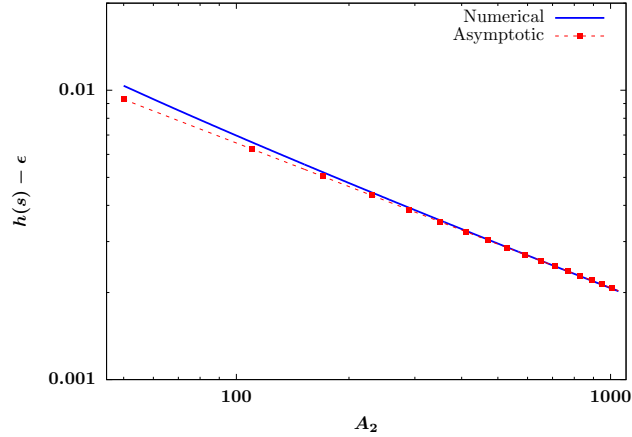


FIGURE 4.20: Comparison of $h(s) - \epsilon$ computed numerically and $h(s)$ from the asymptotic approximation (4.82) for large A_2 plotted in log scale. The solid blue curve denotes the numerical result. The red dashed curve denotes the solution to the asymptotic prediction given by (4.82), with parameters $A_1 = 1$, $\bar{p} = 0.29159$, $L = 6$, $s = 3$, and $\epsilon = 0.1$.

Using the asymptotic prediction $h(s) \sim \epsilon + \frac{\epsilon}{\sqrt{A_2}} \sqrt{-\frac{A_1}{3} + \bar{p}^2 s^2}$, we can also derive $h'(s)$, which represents the contact angle of this class of pinned droplets since the

droplet width $w \sim s$. On the A_1 region $[0, s]$, as $x \rightarrow s^-$, we have

$$\frac{1}{2}h'(s)^2 = A_1 U(h(s)) - \bar{p}h(s) + \bar{p}h_{\max} - A_1 U(h_{\max}) \quad (4.84)$$

Substituting $h(s) \sim \epsilon + \frac{\epsilon}{\sqrt{A_2}}\sqrt{-\frac{A_1}{3} + \bar{p}^2 s^2}$ and $h_{\max} \sim \frac{1}{2}\bar{p}s^2$ into (4.84) and using a Taylor expansion of $U(h)$ at $h = \epsilon$, we obtain

$$\frac{1}{2}h'(s)^2 = A_1 U(\epsilon) + \frac{1}{2}\delta \Pi'(\epsilon)\epsilon^2 \left(-\frac{A_1}{3} + \bar{p}^2 s^2\right) + \frac{1}{2}\bar{p}s^2 - \bar{p}\epsilon - A_1 U\left(\frac{1}{2}\bar{p}s^2\right) + O(\delta) \quad (4.85)$$

which simplifies to

$$h'(s)^2 = \left(-\frac{A_1}{3} + \bar{p}^2 s^2\right) (1 + \delta) + O(\delta^2) \quad (4.86)$$

for $\epsilon \ll 1$. It follows from the Taylor expansion of $\sqrt{1 + \delta}$ that

$$h'(s) = -\sqrt{-\frac{A_1}{3} + \bar{p}^2 s^2} + \frac{1}{2}\delta + O(\delta^2) \quad (4.87)$$

This suggests that for fixed pressure p and s , as $A_2 \rightarrow \infty$, the contact angle of the droplet formed on branch 3 approaches a fixed angle $\theta = \sqrt{-\frac{A_1}{3} + \bar{p}^2 s^2}$. Specifically, the contact angle approaches θ at a rate $|h'(s)| - \theta \propto \frac{1}{2A_2}$. (4.87) also shows that for fixed large A_2 , as the droplet pressure increases on branch 3, the contact angle also increases, at a rate $\sqrt{-\frac{A_1}{3} + \bar{p}^2 s^2}$. In Chapter 3, by asymptotic matching, we showed that the droplets formed on a chemically homogeneous substrate with $A(x) \equiv 1$ have contact angle $\theta = \frac{1}{\sqrt{3}}$ in the limit $\epsilon \rightarrow 0$, which is independent of the droplet pressure \bar{p} . With the introduction of heterogeneity, the contact angle of the “pinned” droplet on branch 3 is now modified to have a dependence on s and \bar{p} . As will be discussed

shortly in Section 4.2.5, on branch 3, the pressure range for branch 3 is asymptotically given by $\frac{\sqrt{A_1}}{\sqrt{3}s} \leq \bar{p} \leq \frac{\sqrt{A_2}}{\sqrt{3}s}$. As A_2 increases, the pressure range and the length of branch 3 both increase. It follows that the contact angle of the droplets on branch 3 is ultimately determined by both s and A_2 , the length and strength of the heterogeneity contrast of the chemical patterning.

By (4.82), we have also shown that for each fixed pressure \bar{p} and s , $h(s) - \epsilon \propto A_2^{-1/2}$ in the limit of large A_2 . This provides a measure for how well the film droplet on branch 3 is confined within the A_1 region in the limit $A_2 \rightarrow \infty$. In the limit $A_2 \rightarrow \infty$ and $\epsilon \rightarrow 0$, we have derived for $s \leq x \leq L$, the solution decays like

$$h(x) \sim \epsilon + \frac{\epsilon}{\sqrt{A_2}} \sqrt{-\frac{A_1}{3} + \bar{p}^2 s^2} e^{-\frac{\sqrt{A_2}(x-s)}{\epsilon}}$$

We have determined $F = \epsilon \sqrt{-\frac{A_1}{3} + \bar{p}^2 s^2}$ so that $\lim_{x \rightarrow s^-} h(x) = \lim_{x \rightarrow s^+} h(x)$. Note that besides the continuity of $h(x)$ at $x = s$, to leading order, this asymptotic prediction also satisfies the continuity of $h'(x)$ at $x = s$, i.e. $\lim_{x \rightarrow s^-} h'(x) = \lim_{x \rightarrow s^+} h'(x)$ with

$$\lim_{x \rightarrow s^+} h'(x) = \sqrt{-\frac{A_1}{3} + \bar{p}^2 s^2} = \lim_{x \rightarrow s^-} h'(x) \quad (4.88)$$

Compared to the solutions on branch 2 which depends on A_1 to leading order, the leading order steady-states on branch 3 depend on s . Figure 4.21 shows the bifurcation diagram p vs. h_{\max} zoomed into branch 3. The blue solid curve represents the numerically computed solution. The red dotted curve denotes the asymptotic prediction $h_{\max} \sim \frac{1}{2} p s^2$ in the limit of small ϵ . We observe that the leading order asymptotic prediction agrees well the numerical results.

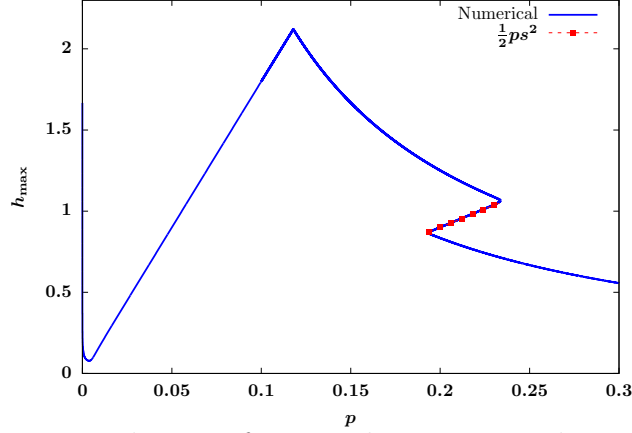


FIGURE 4.21: Bifurcation diagram for p vs. h_{\max} computed numerically and asymptotically using $\frac{1}{2}ps^2$, with parameters $L = 6$, $s = 3$, $A_1 = 1$, $A_2 = 1.5$, and $\epsilon = 0.001$.

4.2.5 Large-width droplets

Branch 4 is also a branch of droplet-type solutions. Compared to the small-width droplets described in Section 4.2.3 and the pinned droplets described in Section 4.2.4, which consists of droplets with width $w \leq s$ and $w \sim \epsilon$ respectively, branch 4 is a class of solutions that describes droplets with $s \leq w \leq L$. For $w \leq x \leq L$, the solution is characterized by an ultra-thin film region with thickness $h = O(\epsilon)$. One example of such a steady-state solution is shown in Figure 4.22. For solutions on branch 2 and branch 3, we have previously shown that $h(s) = O(\epsilon)$. Compared to these solutions, droplets on branch 4 have larger mass, width and h_{\max} , and consequently $h(s) = O(1) \gg \epsilon$. In this subsection, we study the steady-states on branch 4 in two separate limits, in the limit $\epsilon \rightarrow 0$ and the limit $A_2 \rightarrow \infty$. We show that in either limit, the solution depends on A_2 at leading order.

First, we consider the solution in the limit $\epsilon \rightarrow 0$ for $A_1, A_2 = O(1)$. We first assume $h(s) = O(1) \gg \epsilon$. We will show that the asymptotic analysis results produced under this assumption are self-consistent. If $h(s) = O(1)$ and the droplet profile is monotonically decreasing on $[0, L]$, $h_{\max} = O(1) \gg \epsilon$. For $A_1, A_2 = O(1)$, we have $A_i U(h(s)) = O(\epsilon^2)$ and $A_i U(h_{\max}) = O(\epsilon^2)$. In Section 4.2.3, we derived (4.69),

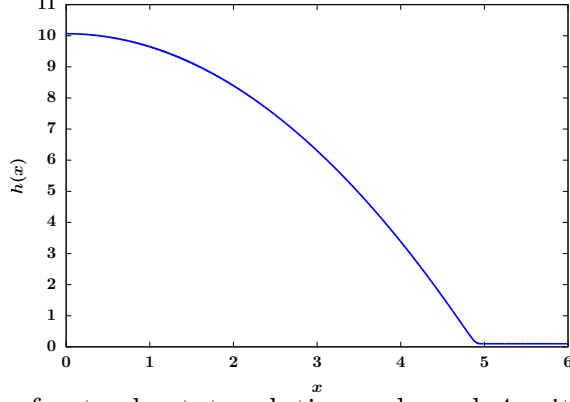


FIGURE 4.22: Profile of a steady-state solution on branch 4, with parameters $A_1 = 1$, $A_2 = 50$, $\bar{p} = 0.835619$, $L = 6$, $s = 3$, and $\epsilon = 0.1$.

which is exact for all steady-state solutions. We use the same equation to study branch 4. For solutions on branch 4, as $\epsilon \rightarrow 0$, at $O(1)$, (4.69) is given by

$$\bar{p}h_{\max} = -A_2U(h_{\min}) + O(\epsilon) = -A_2U(\epsilon) + O(\epsilon) \quad (4.89)$$

This gives

$$h_{\max} = \frac{A_2}{6\bar{p}} + O(\epsilon) \quad (4.90)$$

Note that this is the maximum film thickness of the homoclinic droplet on a homogeneous substrate with $A(x) \equiv A_2$ in the limit $\epsilon \rightarrow 0$. Since $h_{\max} = O(1) \gg \epsilon$, it follows that in the A_1 region $0 \leq x \leq s$, $A_1\Pi(h) \ll \epsilon$. The steady-state equation on the A_1 region can be described by

$$\frac{d^2h}{dx^2} \sim -\bar{p} \quad (4.91)$$

To leading order, the profile of the droplet core is described by

$$h(x) = -\frac{1}{2}\bar{p}x^2 + h_{\max} + O(\epsilon) = -\frac{1}{2}\bar{p}x^2 + \frac{A_2}{6\bar{p}} + O(\epsilon) \quad (4.92)$$

If we evaluate (4.92) at $x = s$, we have

$$h(s) \sim -\frac{1}{2}\bar{p}s^2 + \frac{A_2}{6\bar{p}} = O(1) \quad (4.93)$$

which justifies our earlier assumption that $h(s) = O(1)$ in the limit $\epsilon \rightarrow 0$. Since $h(s) = O(1) \gg \epsilon$ for $\epsilon \rightarrow 0$ and $A_2 = O(1)$, for $s \leq x \ll w$, $A_2 \Pi(h) = O(\epsilon^2) \ll 1$, which suggests that the portion of droplet core residing on the A_2 region could still be approximated by $\frac{d^2 h}{dx^2} \sim -\bar{p}$, yielding (4.92) for $0 \leq x \ll w$. At leading order, the maximum droplet height is determined by A_2 in the limit $\epsilon \rightarrow 0$.

Since the solution exists on a finite domain $[0, L]$, we must have $h_{\min} > h_{\min 2} = O(\epsilon)$. In the phase plane, this means that the solution on branch 4 must be bounded inside the homoclinic orbit that corresponds to $A(x) \equiv A_2$ with $h_{\max} < h_{\max 2}$ where $h_{\max i}$ is the maximum film thickness of the homoclinic solution for $A(x) \equiv A_i$. Figure 4.23 (a) shows the phase plane trajectory of the homoclinic orbit corresponding to $A(x) \equiv A_1$ and $A(x) \equiv A_2$ and the orbit of a chosen steady-state solution on branch 4. The blue dotted curve and the red dotted curve represent the two homoclinic orbits for $A(x) \equiv A_1$ and $A(x) \equiv A_2$ respectively. The solid black curve represents the orbit of the chosen steady-state on branch 4. As can be observed from the figure, the orbit of the branch 4 solution lies inside of the homoclinic orbit for $A(x) \equiv A_2$. Figure 4.23 (b) shows the same plot zoomed into $h_{\min 2} < h_{\min} < h_{\min 1}$. The minimum film thickness of the branch 4 solution is very close to $h_{\min 2}$. Our asymptotic analysis above suggests that as $\epsilon \rightarrow 0$, the solution approaches the homoclinic orbit for the same pressure with $A(x) \equiv A_2$.

Using (4.92), we can calculate an estimate of the droplet width by solving the leading order equation $h(w) \sim 0$, i.e.

$$-\frac{1}{2}\bar{p}w^2 + \frac{A_2}{6\bar{p}} \sim 0 \quad (4.94)$$

It follows that the width of the droplet w at leading order is given by

$$w \sim \frac{\sqrt{A_2}}{\sqrt{3\bar{p}}} \quad (4.95)$$

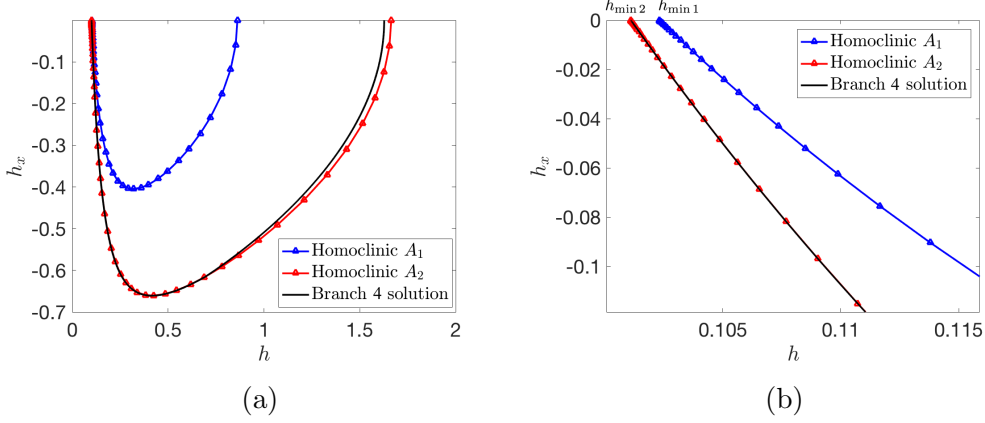


FIGURE 4.23: (a) Phase plane plot of the homoclinic orbit for $A(x) \equiv A_1$ and $A(x) \equiv A_2$ respectively and the plot of h vs. h_x of a steady-state solution on branch 4 (b) Same plot as (a), zoomed into $h_{\min 2} < h < h_{\min 1}$. In both (a) and (b), $A_1 = 1$, $A_2 = 2$, $L = 6$, $s = 3$, $\epsilon = 0.1$, $\bar{p} = 0.210987$.

Since $w \leq L$, the solution is characterized by an ultra-thin film region with $h \sim \epsilon$ for $w \ll x \leq L$. Together, in the limit $\epsilon \rightarrow 0$, the steady-state on the whole domain is given by

$$h(x) \sim \begin{cases} -\frac{1}{2}px^2 + \frac{A_2}{6p} & 0 \leq x \leq \frac{\sqrt{A_2}}{\sqrt{3p}} \\ \epsilon & \frac{\sqrt{A_2}}{\sqrt{3p}} \ll x \leq L \end{cases} \quad (4.96)$$

We described in Section 4.2.4 that the “pinned” droplets on branch 3 have width $w \sim s$. Since branch 4 is connected to branch 3, the intersection of branch 3 and branch 4 occurs at pressure $p_{3,4}^*$ where

$$s \sim \frac{\sqrt{A_2}}{\sqrt{3p_{3,4}^*}} \quad (4.97)$$

This gives

$$p_{3,4}^* \sim \frac{\sqrt{A_2}}{\sqrt{3}s} \quad (4.98)$$

As pressure \bar{p} decreases on branch 4, the droplet width increases. Branch 4 terminates at pressure $p_{4,5}^*$ where branch 4 intersects with branch 5, to be described in the next

section. The point of intersection occurs when $w(p_{4,5}^*) \sim L$, i.e.

$$L \sim \frac{\sqrt{A_2}}{\sqrt{3}p_{4,5}^*} \quad (4.99)$$

which yields

$$p_{4,5}^* \sim \frac{\sqrt{A_2}}{\sqrt{3}L} \quad (4.100)$$

Next, we study the steady-state on branch 4 in the limit $A_2 \rightarrow \infty$ for $A_1 = O(1)$. We show that in the limit of large A_2 , the asymptotic results given by (4.90) still hold as in the limit $\epsilon \rightarrow 0$ for fixed $A_2 = O(1)$. Since (4.69) is exact for all A_1, A_2 , and ϵ , we use (4.69) by first dividing both sides of (4.69) by A_2 . Let $\delta = \frac{1}{A_2} \ll 1$. We arrive at (4.77), which is the same equation previously derived for pinned droplets in the same limit, i.e.

$$(\delta A_1 - 1)U(h(s)) + \delta \bar{p}(h_{\max} - h_{\min}) = \delta A_1 U(h_{\max}) - U(h_{\min}) \quad (4.101)$$

By (4.43)-(4.53) in Section 4.2.3, we have derived that as $A_2 \rightarrow \infty$, for $s \ll x \leq L$, the solution is characterized by an ultra-thin film region which can be described by the outer solution $h(x) = \epsilon$ to leading order. While the length of the ultra-thin film region of the branch 4 solutions has changed, the ultra-thin film near $x = L$ can still be described by this outer solution, which means $h_{\min} = O(\epsilon)$.

Under the assumption that $h(s) \gg \epsilon$, $h_{\min} = O(\epsilon)$ and $A_1 = O(1)$, we know $\delta A_1 U(h(s)) = O(\delta)$, $U(h(s)) \ll 1$, $\delta A_1 U(h_{\max}) = O(\delta)$, $\delta \bar{p} h_{\min} = O(\delta)$ and $U(h_{\min}) = O(1)$. The only term that remains to balance $U(h_{\min})$ is $\delta \bar{p} h_{\max}$. We know that the pressure range for branch 4 is asymptotically given by $p_{3,4}^* < \bar{p} < p_{4,5}^*$. We have also shown in (4.98) and (4.100) that $p_{3,4}^*, p_{4,5}^* = O(\sqrt{A_2}) = O\left(\frac{1}{\sqrt{\delta}}\right)$, which both grow as $A_2 \rightarrow \infty$. As a consequence, we scale \bar{p} by writing $\bar{p} = \sqrt{A_2} \tilde{p}$ for some $\tilde{p} = O(1)$.

This suggests $h_{\max} = O\left(\frac{1}{\delta}\right) = O(\sqrt{A_2})$. We will show that $U(h(s))$ in (4.77) is $O(\delta)$ as a result of this dominant balance, which is consistent with all our earlier assumptions. The dominant balance at leading order for (4.101) is given by

$$\delta \bar{p} h_{\max} = \sqrt{\delta} \tilde{p} h_{\max} = -U(h_{\min}) \quad (4.102)$$

which yields

$$h_{\max} \sim \frac{A_2}{6\bar{p}} \quad (4.103)$$

Note that (4.103) is the same asymptotic estimate for h_{\max} in the limit $\epsilon \rightarrow 0$ for $A_1, A_2 = O(1)$. Although it appears that $h_{\max} \sim \frac{A_2}{6\bar{p}} = O(A_2)$, h_{\max} is, in fact, $O(\sqrt{A_2})$ because $\bar{p} = O(\sqrt{A_2})$, as reasoned above. It follows from this estimate that on $[0, s]$,

$$A_1 \Pi(h_{\max}) = A_1 \Pi\left(\frac{\sqrt{A_2}}{6\tilde{p}}\right) = O\left(\frac{1}{A_2^{3/2}}\right)$$

so $A_1 \Pi(h) \ll \bar{p}$ for $\bar{p} = O(\sqrt{A_2})$ on $[0, s]$. The droplet core on $[0, s]$ can still be described by $\frac{dh^2}{dx^2} \sim -\bar{p}$, which leads to the parabolic profile

$$h(x) \sim -\frac{1}{2}\bar{p}x^2 + h_{\max} \sim -\frac{1}{2}\bar{p}x^2 + \frac{A_2}{6\bar{p}} \quad (4.104)$$

Using the estimate (4.104), we get $h(s) \sim -\frac{1}{2}\bar{p}s^2 + \frac{A_2}{6\bar{p}}$. Even on the A_2 region for $s \leq x \ll w$, we have

$$A_2 \Pi(h(s)) = A_2 \Pi\left(\frac{1}{2}\bar{p}s^2 + \frac{A_2}{6\bar{p}}\right) = A_2 \Pi\left(-\frac{\sqrt{A_2}}{2}\tilde{p}s^2 + \frac{\sqrt{A_2}}{6\tilde{p}}\right) = O\left(\frac{1}{\sqrt{A_2}}\right)$$

which makes $A_2 \Pi(h) \ll \bar{p}$ for $\bar{p} = O(\sqrt{A_2})$ and thus the parabolic profile (4.104) still a valid prediction of the steady-state inside the droplet across the interface of the A_1 and A_2 region.

To show that $U(h(s)) = O(\delta)$, we substitute $h(s)$ into $U(h(s))$, in the limit $A_2 \rightarrow \infty$, we get

$$U(h(s)) = -\frac{18\epsilon^2\tilde{p}^2}{(3\tilde{p}^2s^2 - 1)^2A_2} + O\left(\frac{1}{A_2^{3/2}}\right) \quad (4.105)$$

which confirms that $U(h(s)) = O(\delta)$ in (4.101) and is negligible at $O(1)$. Together, in the limit $A_2 \rightarrow \infty$, the leading order steady-state on the whole domain can be described by

$$h(x) \sim \begin{cases} -\frac{1}{2}\bar{p}x^2 + \frac{A_2}{6\bar{p}} & 0 \leq x \leq \frac{\sqrt{A_2}}{\sqrt{3\bar{p}}} \\ \epsilon & \frac{\sqrt{A_2}}{\sqrt{3\bar{p}}} \ll x \leq L \end{cases} \quad (4.106)$$

which has the same form as the solution in the limit $\epsilon \rightarrow 0$ for fixed $A_2 = O(1)$, as shown in (4.96).

Figure 4.24 (a) shows the bifurcation diagram for p vs. h_{\max} computed numerically and asymptotically for branch 4 for $A_1, A_2 = O(1)$ in the limit of small ϵ . Figure 4.24 (b) shows the bifurcation diagram for p vs. h_{\max} computed numerically and asymptotically for branch 4 in the limit of large A_2 . In both Figure 4.24 (a) and Figure 4.24 (b), the blue solid curve represents the numerically computed bifurcation curve. The red dashed and dotted curve represents the asymptotic prediction given by $\frac{A_2}{6\bar{p}}$. We observe from both figures that the asymptotic prediction $\frac{A_2}{6\bar{p}}$ agrees well with the numerical results in both limits. $p_{3,4}^*$, the pressure at which branch 3 and branch 4 intersect is labeled in both figures. Similarly, $p_{4,5}^*$, the pressure at which branch 4 and branch 5 intersect is also labeled. Note that the film mass $m_{4,5}^*$ corresponding to $p_{4,5}^*$ is the maximum film mass for which a droplet-type solution could exist. The only solution that exists with mass $m > m_{4,5}^*$ belongs to branch 6, which is characterized by a small perturbation from a thick layer of flat film. In both the

limits $\epsilon \rightarrow 0$ and $A_2 \rightarrow \infty$, we can estimate $m_{4,5}^*$ by

$$m_{4,5}^* \sim \frac{\sqrt{3}}{9} \sqrt{A_2} L^2 \quad (4.107)$$

Note that this is also the maximum mass m_{\max} defined for the outer loop solution shown in Figure 4.4 in Section 4.1. This shows for fixed domain size L , the maximum mass for which a droplet could exist on this domain scales with $\sqrt{A_2}$. Through asymptotic analysis, we have shown that branch 4 is a class of solutions that can be described by the homoclinic droplets corresponding to $A(x) \equiv A_2$ at leading order.

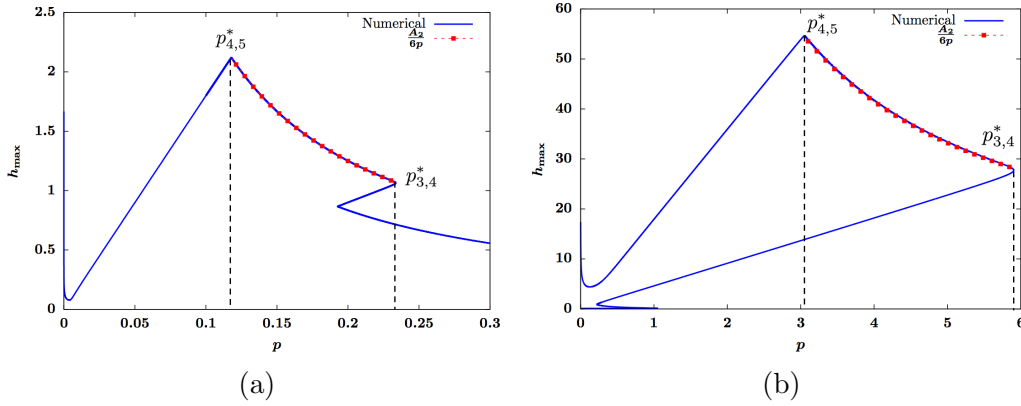


FIGURE 4.24: Bifurcation diagram for p vs. h_{\max} computed numerically and asymptotically for branch 4 (a) in the limit $\epsilon \rightarrow 0$, with parameters $A_1 = 1$, $A_2 = 1.5$, and $\epsilon = 0.001$. (b) in the limit $A_2 \rightarrow \infty$, with parameters $A_1 = 1$, $A_2 = 1000$, $\epsilon = 0.1$. In both (a) and (b), $L = 6$, $s = 3$.

4.2.6 Large confined droplets

In Section 4.2.5, we have shown that for branch 4 solutions, both the maximum film thickness h_{\max} and droplet width w increase with pressure \bar{p} . Branch 4 terminates at $p_{4,5}^*$ when the droplet on branch 4 attains a maximum mass $m_{4,5}^*$. For $\bar{p} < p_{4,5}^*$, there is another branch that connects branch 4 and branch 6. We call it branch 5. Branch 5 is a class of solutions that continues to exist for $\bar{p} < p_{4,5}^*$ and is characterized by a large droplet with width $w \sim L$. As the fluid mass grows on branch 5, the droplets

formed grow in size but are confined by the domain size so the droplet width remains L regardless of fluid mass and pressure. An example of a solution on branch 5 is shown in Figure 4.25. This type of solutions has a similar structure with that of the finite-amplitude solutions on homogeneous substrates studied by Bertozzi et al. in [7]. In this subsection, we focus on the steady-state solutions on branch 5.

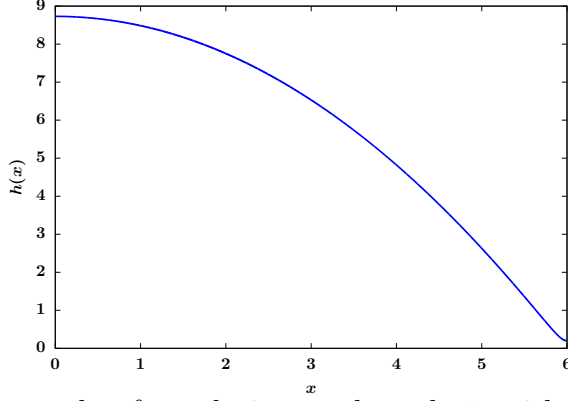


FIGURE 4.25: An example of a solution on branch 5, with parameters $A_1 = 1$, $A_2 = 50$, $L = 6$, $s = 3$, $\epsilon = 0.1$, and $\bar{p} = 0.488638$.

On branch 5, the droplets formed all have width $w \sim L$. For \bar{p} near $p_{4,5}^*$, the solution is still characterized by large mass and large h_{\max} so $h(s) \gg \epsilon$ still holds as in branch 4. However, branch 5 is distinct from branch 4 in that given the same mass, a solution on branch 5 has smaller amplitude $h_{\max} - h_{\min}$. Since the droplets occupy the whole domain $[0, L]$, there is no more ultra-thin film region. The minimum film thickness for branch 4 is $h_{\min} \sim \epsilon$, but for branch 5, we will get $h_{\min} \sim C\epsilon$ for some C that depends on p , L and A_2 . We study the solutions on branch 5 in two limits, in the limit $\epsilon \rightarrow 0$ with $A_1, A_2 = O(1)$ and $A_2 \rightarrow \infty$ with $A_1 = O(1)$.

We first investigate the solution in the limit $\epsilon \rightarrow 0$ for $A_1, A_2 = O(1)$. For $\bar{p} < p_{4,5}^*$ and near $p_{4,5}^*$, the solution is still characterized by a large droplet with $h(s) = O(1)$, like branch 4. Assume $h(s) = O(1)$. The profile of the droplet core can still be described by the parabola $h(x) \sim -\frac{1}{2}\bar{p}x^2 + h_{\max}$. Since the droplets now have width

$w \sim L$, to leading order, the maximum film thickness of the droplets on branch 5 is given in terms of L by

$$h_{\max} = \frac{1}{2}\bar{p}L^2 + O(\epsilon) \quad (4.108)$$

This implies $h(s) = -\frac{1}{2}\bar{p}s^2 + \frac{1}{2}\bar{p}L^2$, which validates our assumption that $h(s) = O(1)$. Since there is no longer an ultra-thin film region, the minimum film thickness of this branch of solutions is different from that of branch 4. To obtain an asymptotic estimate of the minimum film thickness h_{\min} of branch 5, we use (4.69), which holds for all branches and has been used to derive asymptotic predictions for previous branches. Following (4.69), we have

$$(A_1 - A_2)U(h(s)) + \bar{p}(h_{\max} - h_{\min}) = A_1U(h_{\max}) - A_2U(h_{\min})$$

Under our current assumptions, $A_1, A_2 = O(1)$, $\bar{p} = O(1)$, $h(s) \sim -\frac{1}{2}\bar{p}s^2 + \frac{1}{2}\bar{p}L^2 = O(1)$, and $h_{\max} = \frac{1}{2}\bar{p}L^2 = O(1)$. For now, we assume $h_{\min} = O(\epsilon)$. We will later show that our choice of dominant balance at $O(1)$ is consistent with this assumption. In the limit $\epsilon \rightarrow 0$, the dominant balance at $O(1)$ is then given by

$$-A_2U(h_{\min}) = \bar{p}h_{\max} \sim \frac{1}{2}\bar{p}^2L^2 \quad (4.109)$$

(4.109) reduces to a cubic polynomial. The positive real root h_{\min} , expressed in terms of \bar{p} , is given by

$$h_{\min} \sim \frac{1}{9} \frac{\left(3^{2/3} \left(-A_2 \left(3\bar{p}L - \sqrt{9L^2\bar{p}^2 - 3A_2}\right)\right)^{2/3} + 3A_2\right) \epsilon^{3/3}}{pL \sqrt[3]{-A_2 \left(3\bar{p}L - \sqrt{9L^2\bar{p}^2 - 3A_2}\right)}} \quad (4.110)$$

which is $O(\epsilon)$ for $A_2 = O(1)$ and thus consistent with our earlier assumption. Note that the potential function $U(h)$ has a global minimum at $h = \epsilon$ and $U(\epsilon) = -\frac{1}{6}$.

For (4.109) to have a solution, we need

$$\frac{1}{2A_2}\bar{p}^2L^2 \leq \frac{1}{6} \quad (4.111)$$

We know this is true for all solutions on branch 5 since $p < p_{4,5}^* \sim \frac{\sqrt{A_2}}{\sqrt{3}L}$ on branch 5. Figure 4.26 (a) and (b) show the diagram for p vs. h_{\max} and p vs. h_{\min} computed numerically and asymptotically in the limit of small ϵ for $A_1, A_2 = O(1)$. The solid blue curve represents the numerically computed curve. The dotted dashed red curve represents the asymptotic prediction of h_{\max} and h_{\min} computed using (4.108) and (4.109). In both Figure 4.26 (a) and (b), $A_1 = 1$, $A_2 = 1.5$, $\epsilon = 0.001$. The results suggest that the asymptotic approximation derived in the small ϵ limit agrees well with the numerical calculations.

Using a similar asymptotic matching argument presented for homoclinic droplets on homogeneous substrates in Section 3.1.1, specifically (3.27)-(3.29), we can derive the contact angle formed by the branch 5 droplets in the limit $\epsilon \rightarrow 0$. Since the droplets have $w \sim L$, in the contact line region, we rescale $h(x)$ by $h(x) = \epsilon H(Z)$ for $Z = \frac{L-x}{\epsilon}$. Then at leading order, the steady-state equation in this region is given by

$$\frac{1}{2}H'(Z)^2 = A_2U(\epsilon H) - A_2U(h_{\min}) = A_2U(\epsilon H) + \frac{1}{2}\bar{p}^2L^2 \quad (4.112)$$

As $Z \rightarrow -\infty$, $h = \epsilon H \rightarrow h_{\min}$ so $H'(Z) \rightarrow 0$. As $Z \rightarrow \infty$, $h = \epsilon H \rightarrow O(1)$, so $A_2U(\epsilon H) \ll 1$ for $A_2 = O(1)$. It follows that as $Z \rightarrow \infty$,

$$H'(Z) = \bar{p}L \quad (4.113)$$

so the contact angle of the droplets on branch 5 is given by $\theta \sim \bar{p}L$ to leading order.

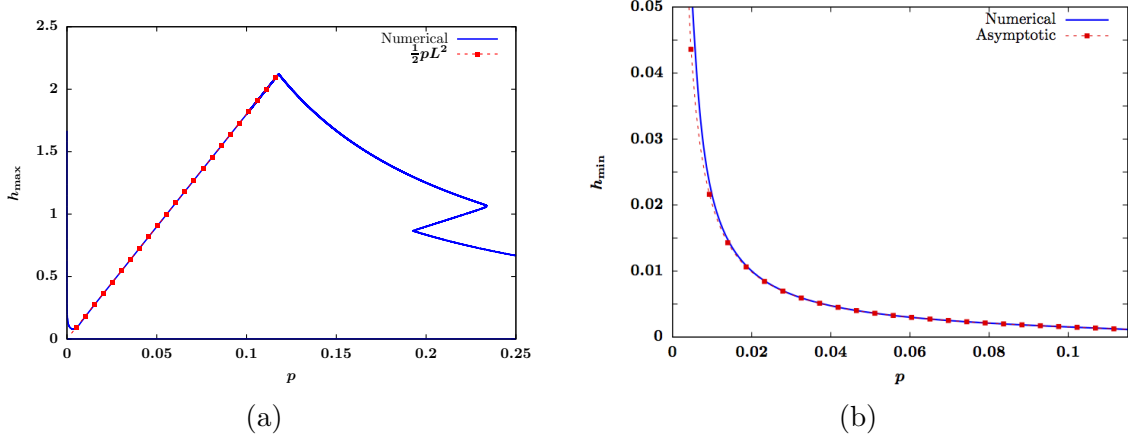


FIGURE 4.26: (a) Bifurcation diagram for p vs. h_{\max} computed numerically (blue solid curve) and asymptotically (red dotted curve) in the limit of small ϵ . The asymptotic prediction is given by $h_{\max} = \frac{1}{2}pL^2$. (b) p vs. h_{\min} computed numerically (blue solid curve) and asymptotically (red dotted curve) in the limit of small ϵ where the asymptotic prediction of h_{\min} is given by (4.110). In both (a) and (b), $A_1, A_2 = 1.5$, $L = 6$, $s = 3$, $\epsilon = 0.001$.

Next, we investigate the solutions on branch 5 in the limit $A_2 \rightarrow \infty$ for $A_1 = O(1)$ fixed. We show that the leading order asymptotic prediction in this limit is the same as that in the limit $\epsilon \rightarrow 0$ with $A_2 = O(1)$, as discussed above. Let $\delta = \frac{1}{A_2}$ for $\delta \ll 1$. To study this limit, we employ (4.77), which is the same equation used to study branch 3 and branch 4 in the limit of large A_2 . Writing out (4.77), we have

$$(\delta A_1 - 1)U(h(s)) + \delta p(h_{\max} - h_{\min}) = \delta A_1 U(h_{\max}) - U(h_{\min}) \quad (4.114)$$

We know that the pressure $p_{4,5}^* \sim \frac{\sqrt{A_2}}{\sqrt{3}L}$ at which branch 5 intersects with branch 4 grows as A_2 grows. Hence, for \bar{p} near $p_{4,5}^*$ on branch 5, $\bar{p} = O(\sqrt{A_2}) = O\left(\frac{1}{\sqrt{\delta}}\right)$. As a result, we scale \bar{p} by writing $\bar{p} = \frac{1}{\sqrt{\delta}}\tilde{p}$ for some $\tilde{p} = O(1)$, as in the choice of dominant balance for branch 4 in Section 4.2.5. To determine the order of $\delta\bar{p}h_{\max}$, for now, we assume that $h_{\max} = O(1)$. We will come back to this assumption and show

that it is consistent with the dominant balance chosen in our asymptotic analysis.

Suppose $h_{\max} = O(1)$. Inside the droplet core, we have $A_1\Pi(h) \ll \bar{p}$ for $\bar{p} = O(\sqrt{A_2})$ in the limit $A_2 \rightarrow \infty$. It follows that inside the droplet core, we can approximate the steady-state by the parabola

$$h(x) \sim -\frac{1}{2}\bar{p}x^2 + h_{\max}$$

Since $w \sim L$, we have $h_{\max} = \frac{1}{2}\bar{p}L^2 = O(1)$, which is consistent with our earlier assumption. Since $\bar{p} = O(\sqrt{A_2}) = O\left(\frac{1}{\sqrt{\delta}}\right)$, using the estimate $h_{\max} \sim \frac{1}{2}\bar{p}L^2$, we have

$$\delta\bar{p}h_{\max} \sim \delta\frac{1}{2}\bar{p}^2L^2 = \frac{1}{2}\tilde{p}^2L^2 = O(1)$$

and

$$U(h(s)) \sim U\left(-\frac{1}{2}\bar{p}s^2 + \frac{1}{2}\bar{p}L^2\right) = U\left(\frac{1}{2}\sqrt{A_2}\tilde{p}(-s^2 + L^2)\right) = -\frac{2\epsilon^2}{\tilde{p}^2(L^2 - s^2)^2 A_2} + O\left(\frac{1}{A_2^{3/2}}\right)$$

It follows that the dominant balance of (4.114) at $O(1)$ is given by

$$\frac{1}{2}\tilde{p}^2L^2 = -U(h_{\min}) \tag{4.115}$$

Written in the original pressure \bar{p} , (4.115) is exactly the same asymptotic prediction for h_{\min} in the limit $\epsilon \rightarrow 0$ with $A_2 = O(1)$, as shown in (4.109). However, (4.115), written in the scaled variable $\tilde{p} = O(1)$ suggests that h_{\min} does not depend on A_2 at leading order and that $h_{\min} = O(\epsilon)$ in the limit $A_2 \rightarrow \infty$. Figure 4.27 (a) and (b) show the diagram for p vs. h_{\max} and p vs. h_{\min} computed numerically and asymptotically for branch 5 in the limit of large A_2 . The solid blue curve represents the numerically computed h_{\max} and h_{\min} for each \bar{p} . The dashed dotted red curve represents the asymptotic prediction. The asymptotic approximation for h_{\max} is

given by $h_{\max} \sim \frac{1}{2}\bar{p}L^2$. The asymptotic approximation for h_{\min} is given by (4.115).

In both Figure 4.27 (a) and (b), $A_1 = 1$ and $A_2 = 1000$. The results suggest that the asymptotic predictions derived for the large A_2 limit agree well the numerical calculations.

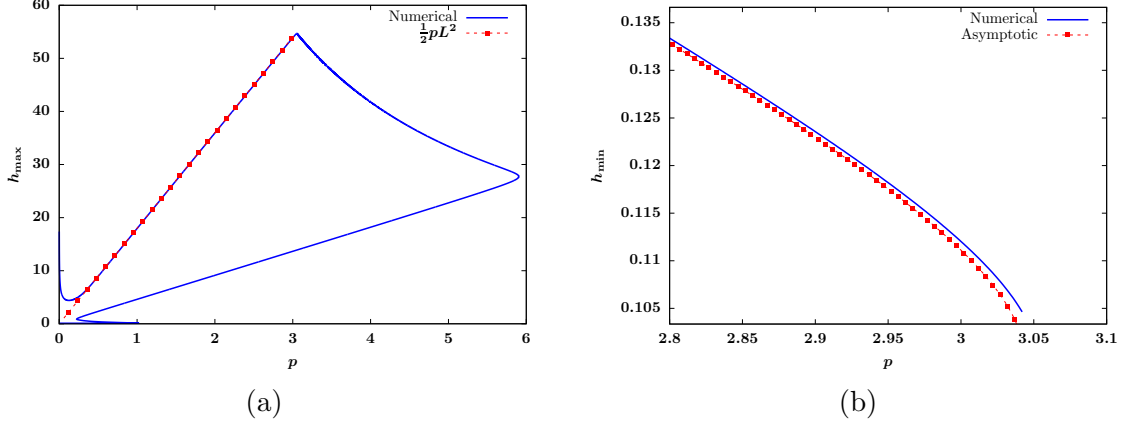


FIGURE 4.27: (a) Bifurcation diagram for p vs. h_{\max} computed numerically (blue solid curve) and asymptotically (red dotted curve) in the limit of large A_2 . The asymptotic prediction is given by $h_{\max} \sim \frac{1}{2}pL^2$. (b) p vs. h_{\min} computed numerically (blue solid curve) and asymptotically (red dotted curve) in the limit of large A_2 where the asymptotic prediction of h_{\min} is given by (4.115). In both (a) and (b), $A_1, A_2 = 1000$, $L = 6$, $s = 3$, $\epsilon = 0.1$.

4.3 Stability of steady-state solutions

We use linear stability analysis to determine the stability of the different steady-states on heterogeneous substrates. The evolution of thin films on heterogeneous substrates, subject to no-flux boundary conditions, is governed by

$$\frac{\partial h}{\partial t} = \frac{\partial}{\partial x} \left(h^3 \frac{\partial}{\partial x} \left(A(x) \Pi(h) - \frac{\partial^2 h}{\partial x^2} \right) \right) \quad (4.116a)$$

$$J(0) = J(L) = 0, \quad \frac{dh}{dx}(0) = \frac{dh}{dx}(L) = 0 \quad (4.116b)$$

To determine the stability of a given steady-state droplet $\bar{h}(x; \bar{p})$, we write the solution as $h(x, t) = \bar{h}(x; \bar{p}) + \delta h_1(x, t)$ for some $\delta \ll 1$. For simplicity of notation, we denote the steady-state solution $\bar{h}(x; \bar{p})$ with a given fixed pressure \bar{p} by $\bar{h}(x)$. Substituting $h(x, t) = \bar{h}(x) + \delta h_1(x, t)$ into the full evolution equation (4.116a) and linearizing, at $O(\delta)$, we obtain

$$\frac{\partial h_1}{\partial t} = \mathcal{L}h_1 \quad (4.117a)$$

$$\frac{\partial h_1}{\partial x}(0) = \frac{\partial h_1}{\partial x}(L) = 0, \quad \frac{\partial^3 h_1}{\partial x^3}(0) = \frac{\partial^3 h_1}{\partial x^3}(L) = 0 \quad (4.117b)$$

where \mathcal{L} is given by

$$\mathcal{L}g = (\bar{h}^3(A(x)\Pi'(\bar{h})g - g_{xx})_x)_x \quad (4.118)$$

By separation of variables, the solution $h_1(x, t)$ can be written as $h_1(x, t) = \sum_n c_n g_n(x) e^{\lambda_n t}$

where λ_n is the eigenvalue of \mathcal{L} whose corresponding eigenfunction is $g_n(x)$ and c_n is some constant determined by the initial condition. Determining the stability of the steady-state $\bar{h}(x)$ amounts to solving the eigenvalue problem for \mathcal{L} , i.e.

$$\mathcal{L}g = \lambda g \quad (4.119)$$

In this section, we investigate the stability of the six different branches of solutions on heterogeneous substrates discussed above by applying linear stability analysis to a chosen parameter set $A(x)$ and L . Specifically, we solve the eigenvalue problem (4.119) for the parameter choice $A_1 = 1$, $A_2 = 50$, $L = 6$, $s = 3$, $\epsilon = 0.1$ by using the eigenvalue solver in MATLAB. By continuation in pressure \bar{p} , we find that of all the six different branches discussed above, branch 5 is the only unstable branch, while other branches all characterize stable steady-state solutions.

We validate the results of our eigenvalue calculations in MATLAB by numerically solving the evolution equation (4.116a) with the initial condition $h(x, 0) = \bar{h}(x) + \delta g_1(x)$ where $g_1(x)$ is the normalized eigenfunction in L_2 norm corresponding to

the most unstable mode eigenmode of the steady-state $\bar{h}(x)$. Now we illustrate this process for a typical solution on branch 5. We pick the unstable branch 5 steady-state $\bar{h}(x)$ with uniform pressure $\bar{p} = 0.171423$ on the substrate $A_1 = 1$, $A_2 = 50$, $L = 6$, $s = 3$, $\epsilon = 0.1$. The largest eigenvalue is $\lambda_1 = 2.0875$. If we initialize the PDE by $h(x, 0) = \bar{h}(x) + \delta g_1(x)$, then for short time, we expect $\|h(x, t) - \bar{h}(x)\| \approx \delta e^{\lambda_1 t}$. Figure 4.28 (a) shows the plot of $g_1(x)$, which is the normalized eigenfunction corresponding to λ_1 . Figure 4.28 (b) shows the semi-log plot of $\|h(x, t) - \bar{h}(x)\|_2$ compared with $\delta e^{\lambda_1 t}$ for $\delta = 10^{-7}$ for short time. The numerical simulation results confirm that the solution evolves away from the unstable steady-state $\bar{h}(x)$ at rate λ_1 for short time, which validates the results of our eigenvalue computation.

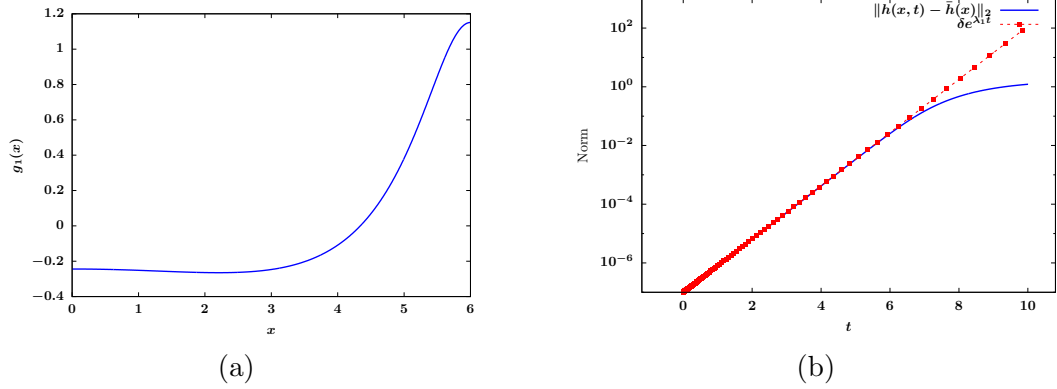


FIGURE 4.28: (a) Normalized eigenfunction $g_1(x)$ corresponding to the most unstable eigenmode with $\lambda_1 = 2.0875$ for $\bar{p} = 0.171423$. (b) Semi-log plot of the norm $\|h(x, t) - \bar{h}(x)\|_2$ computed by numerically solving the evolution PDE and by linearization $\delta e^{\lambda_1 t}$ where $\delta = 10^{-7}$.

Let m be the mass of the unstable branch 5 droplet chosen above. Then there exist three distinct steady-state solutions with the same mass m . The solution on branch 5 is the only unstable solution. If we initialize the PDE with $h(x, 0) = \bar{h}(x) + \delta \tilde{g}(x)$ for some $\tilde{g}(x)$ with $\|\tilde{g}(x)\|_2 = 1$, then the solution $h(x, t)$ moves away from $\bar{h}(x)$ and evolves towards the stable solution on branch 6 or the stable solution on branch 4 with the same mass, subject to no-flux boundary conditions. Figure 4.29 (a) and (b)

show the two different stable equilibria attained by the solution at large time with two different initial conditions. Figure 4.29 (a) shows when the initial condition is given by $h(x, 0) = \bar{h}(x) + \delta g_1(x)$, the stable equilibrium attained is a branch 6 solution with the same mass. Figure 4.29 (b) shows when the initial condition is given by $h(x, 0) = \bar{h}(x) - \delta g_1(x)$, the stable equilibrium attained is a branch 4 solution with the same mass. In both Figure 4.29 (a) and (b), the solid blue curve represents the stable solution attained. The dotted and dashed curve represents the unstable branch 5 solution with $\bar{p} = 0.171$ as described above.

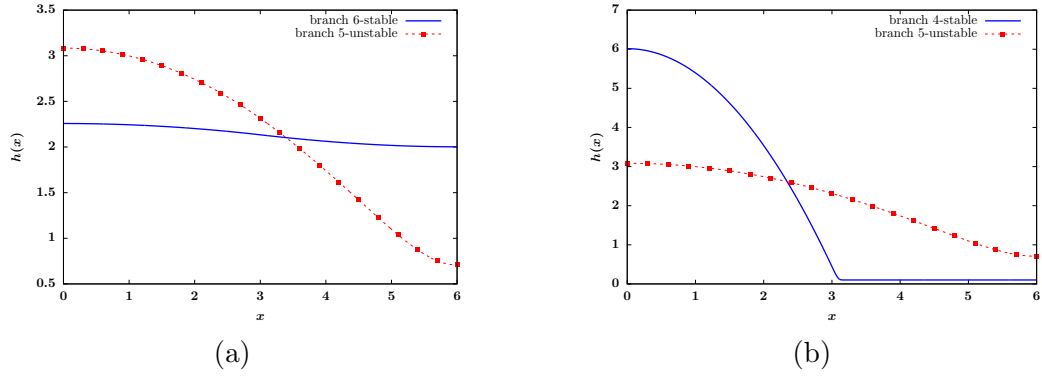


FIGURE 4.29: (a) The stable solution (branch 6) attained when $h(x, 0) = \bar{h}(x) + \delta g_1(x)$. (b) The stable solution (branch 4) attained when $h(x, 0) = \bar{h}(x) - \delta g_1(x)$.

In Section 4.1, we showed the structure of the inner loop of the bifurcation diagram for m vs. h_{\max} for a set of increasing A_2 values, as demonstrated in Figure 4.5 (a)-(i). Here, we illustrate the stability of solutions on these inner loops by computing the stability of some chosen solutions for the case $A_2 = 1.1$ and $A_2 = 7$. First, we determine the stability of four solutions, all with the same chosen mass $m = 0.6$ on the inner loop for the case of a relatively small wettability contrast $L = 3$, $s = 1.5$, $A_1 = 1$ and $A_2 = 1.1$, which is shown in Figure 4.5 (a). We compute the eigenvalues for these four solutions, all with mass $m = 0.6$, as labeled by asterisks in the bifurcation diagram shown in Figure 4.30 (a). Figure 4.30 (b) shows the corresponding profile of the four solutions. Linear stability analysis suggests that of

the four steady-states with the same mass, only solution 4 is a stable steady-state. Solution 1-3 are all unstable steady-states. Note that solution 4 is on a larger loop that is analogous to the outer loop. This loop arises due to the heterogeneity of the substrate, resulting in the asymmetry of the droplets centered at $x = 0$ and $x = L$.

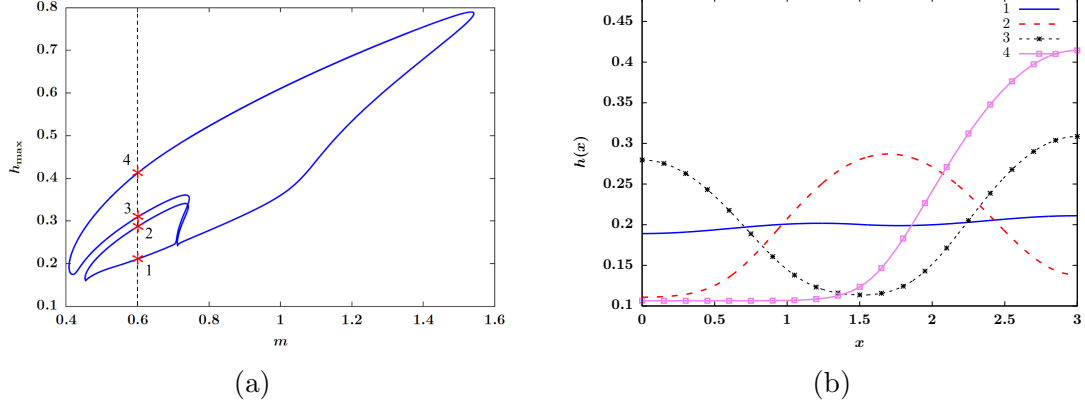


FIGURE 4.30: (a) Four distinct steady-states on the inner loop, all with mass $m = 0.6$ labeled in the bifurcation diagram. (b) Corresponding profile of the four solutions. In (a)-(b), $L = 3$, $s = 1.5$, $A_1 = 1$, $A_2 = 1.1$, $\epsilon = 0.1$.

Now we determine the stability of two solutions both with the same chosen mass $m = 1.13$ on the inner loop for the case of a relatively large wettability contrast $L = 3$, $s = 1.5$, $A_1 = 1$ and $A_2 = 7$, which is shown in Figure 4.5 (i). These two solutions are labeled by asterisks in the bifurcation diagram shown in Figure 4.31 (a). The corresponding profile of the two solutions is shown in Figure 4.31 (b). As can be observed from the figure, for $A_2 = 7$, the inner loop is already small in size and degenerates to a closed loop with no self-intersections. Computation results suggest that both of the two solutions are unstable. Our overall linear stability analysis results indicate that as A_2 increases and the inner loop degenerates, the solutions on the inner loop become increasingly unstable. Even for small A_2 , only the solution with the largest amplitude is stable. Compared to the inner loop, the outer loop is characterized by more stable steady-states, which is also one of the reasons why we

focused on the studies of outer loop in this chapter.

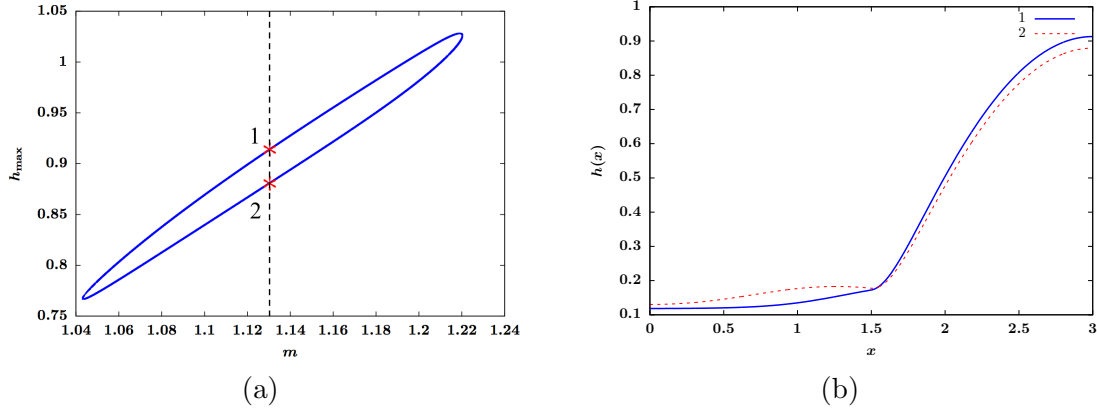


FIGURE 4.31: (a) Two distinct steady-states on the inner loop, both with mass $m = 1.13$ labeled in the bifurcation diagram. (b) Corresponding profile of the two solutions. In (a)-(b), $L = 3$, $s = 1.5$, $A_1 = 1$, $A_2 = 7$, $\epsilon = 0.1$.

4.4 Leak and spillover in the limit of large A_2

By studying the six different types of solutions which correspond to the six different branches in Section 4.2.1-4.2.6, we find that branch 2 through branch 5 are all characterized by droplet-type solutions. Of these four branches, branch 2 and branch 3 are two branches, for which the droplet core completely resides inside of the A_1 region. As the A_2 region becomes increasingly hydrophobic, i.e. in the limit of large A_2 , the fluid mass becomes increasingly concentrated on the A_1 region. In other words, in the limit of large A_2 , the A_2 region has an increasingly confining effect on the fluid droplets formed on the A_1 region. In applications where accurate dispensing and distribution of fluid on solid surfaces are required, it is important to develop a quantitative understanding of the degree of leaking and spillover of the fluid from the A_1 region into the A_2 region. In this subsection, we present a measure for the degree of this leakage for branch 2 and branch 3 and show by using the results derived in Section 4.2.3 and Section 4.2.4 that in accordance with this measure, the leakage is

inversely proportional to A_2 in the large A_2 limit.

In both Section 4.2.3 and Section 4.2.4, we showed that the film thickness at the interface $h(s) \rightarrow \epsilon$ as $A_2 \rightarrow \infty$. We also showed that in the outer A_2 region, as $x \rightarrow L$, $h(x) \sim \epsilon$ in the limit $A_2 \rightarrow \infty$. To measure the fluid leakage, we use the fluid mass above $h(x) = \epsilon$ on $x \in [s, L]$, as illustrated by the colored region in Figure 4.32.

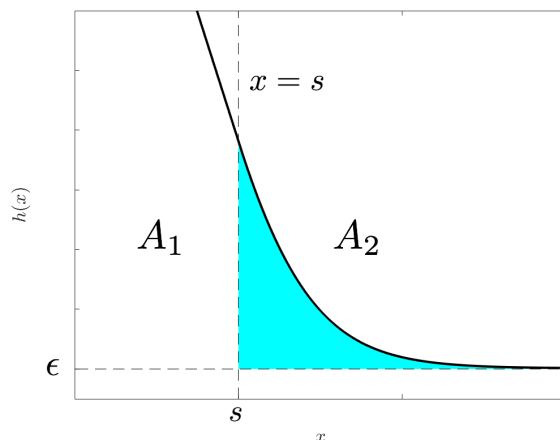


FIGURE 4.32: Illustration of the measure of fluid leakage

We define the mass of leakage as

$$\text{Leakage} = \int_s^L \left[h(x) - \epsilon \right] dx \quad (4.120)$$

As discussed in Section 4.2.3, there is a boundary layer in the solutions on branch 2 near the interface of the A_1 and A_2 region. In Section 4.2.3, we concluded that this boundary layer can be described by in a similar way as the way in which the boundary layer of branch 1 solutions are constructed. The asymptotic expansion of $h(x)$ for $s \leq x \leq L$ is given by (4.20) in Section 4.2.1, which is restated below.

$$h(x) \sim h_{\min 2} + C_2 e^{-\sqrt{A_2 \Pi'(h_{\min 2})}(x-s)}, \quad s \leq x \leq L \quad (4.121)$$

The coefficient C_2 is also given previously by (4.22b), i.e.

$$C_2 = \frac{(h_{\min 1} - h_{\min 2})\sqrt{A_1\Pi'(h_{\min 1})}}{\sqrt{A_1\Pi'(h_{\min 1})} + \sqrt{A_2\Pi'(h_{\min 2})}} \quad (4.122)$$

In Section 4.2.3, we showed that in the limit of large A_2 ,

$$C_2 \sim \epsilon^2 \frac{\bar{p}}{\sqrt{A_1 A_2}} \quad (4.123)$$

and

$$h_{\min 2} \sim \epsilon + \frac{\epsilon^2 \bar{p}}{A_2} \quad (4.124)$$

Using (4.121) and (4.122), we calculate the mass of the fluid leakage of solutions given by (4.120). This yields

$$\text{Leakage} \sim \int_s^L h_{\min 2} - \epsilon + C_2 e^{-\sqrt{A_2\Pi'(h_{\min 2})}(x-s)} dx \quad (4.125)$$

In the limit $A_2 \rightarrow \infty$, we use the asymptotic results (4.123)-(4.124) to derive a leading order asymptotic prediction of the leakage given by (4.125). This gives

$$\text{Leakage} \sim \left[\frac{\epsilon^3 \bar{p}}{\sqrt{A_1}} + \epsilon^2 \bar{p}(L-s) \right] \frac{1}{A_2} \quad (4.126)$$

in the limit $A_2 \rightarrow \infty$, which suggests that at leading order, the fluid leakage of solutions on branch 2 is inversely proportional to A_2 for large A_2 . Figure 4.33 shows the fluid leakage computed numerically and asymptotically for a solution on branch 2 plotted in log scale. We fix the droplet pressure p and increase A_2 . The numerical result is obtained by first numerically solving for $h(x)$ and then numerically integrating (4.120) using the trapezoid rule. The asymptotic approximation is calculated by (4.126). The results in Figure 4.33 suggest that the asymptotic description given by (4.126) produces a good prediction of fluid leakage defined by (4.120).

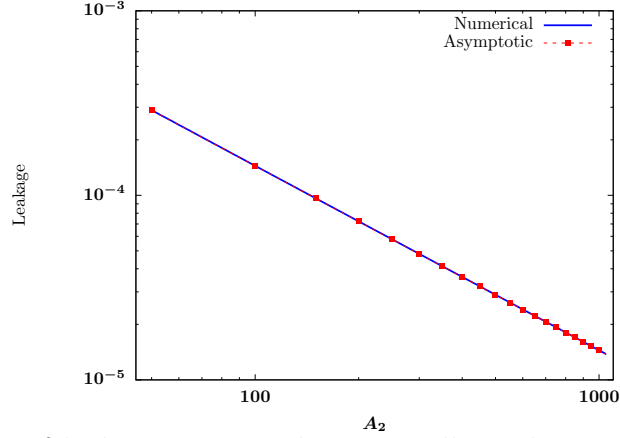


FIGURE 4.33: Mass of leakage computed numerically and asymptotically for a solution on branch 2 plotted in log scale. The asymptotic prediction is given by (4.126). The pressure \bar{p} is fixed as A_2 increases, for parameters $\bar{p} = 0.465737$, $L = 6$, $s = 3$, $A_1 = 1$, $\epsilon = 0.1$.

Similarly, we calculate the fluid leakage of solutions on branch 3, which is a class of droplets pinned at $x = s$. We have shown in Section 4.2.4 that in the limit $A_2 \rightarrow \infty$, the profile of a branch 3 solution on $[s, L]$ can be described asymptotically by (4.76), i.e.

$$h(x) \sim \epsilon + \frac{1}{\sqrt{A_2}} F e^{-\frac{\sqrt{A_2}(x-s)}{\epsilon}} + O\left(\frac{1}{A_2}\right) \quad (4.127)$$

where F is given by (4.83), i.e.

$$F = \epsilon \sqrt{-\frac{A_1}{3} + \bar{p}^2 s^2} \quad (4.128)$$

As is stated in Section 4.2.4, (4.130) is a result of the derivation shown by (4.42)-(4.53) in Section 4.2.3 where we constructed an asymptotic approximation of the boundary layer in the limit $A_2 \rightarrow \infty$ by matching the outer solution with the inner solution. In particular, up to $O\left(\frac{1}{A_2}\right)$, the outer solution describing the film profile away from the interface $x = s$ is given by (4.45), i.e.

$$h^{out}(x) \sim \epsilon + \frac{\epsilon^2}{A_2} \quad (4.129)$$

In the derivation of branch 3 solutions, specifically (4.82), we left out the term $\frac{\epsilon^2}{A_2}$ since it is a higher-order term in the expansion $h(s) = \epsilon + \frac{\epsilon F}{\sqrt{A_2}} + O\left(\frac{1}{A_2}\right)$. In the following calculations, we will show that the leakage of solutions on branch 3 at leading order scales like $\frac{1}{A_2}$. Therefore, it is necessary that we keep the higher-order term $\frac{\epsilon^2}{A_2}$ in our asymptotic expansion to obtain the full leading order approximation of the fluid leakage. To derive the asymptotic behavior of the leakage on branch 3, we use the expansion

$$h(x) \sim \epsilon + \sqrt{\delta} F e^{-\frac{(x-s)}{\epsilon\sqrt{\delta}}} + \frac{\epsilon^2 \bar{p}}{A_2} \quad (4.130)$$

for F given by (4.128). Now we evaluate (4.120) using (4.130) in the limit of large A_2 , which yields

$$\begin{aligned} \text{Leakage} &\sim \int_s^L \left[\frac{\epsilon^2 \bar{p}}{A_2} + F \frac{1}{\sqrt{A_2}} e^{-\frac{\sqrt{A_2}(x-s)}{\epsilon}} \right] dx \\ &\sim \left[\epsilon^2 \sqrt{-\frac{A_1}{3} + \bar{p}^2 s^2} + \epsilon^2 \bar{p}(L-s) \right] \frac{1}{A_2} \end{aligned} \quad (4.131)$$

This suggests that the leakage of branch 3 solutions is also inversely proportional to A_2 in the limit of large A_2 , like branch 2. Figure 4.34 shows the mass of leakage computed numerically and asymptotically for a steady-state on branch 3 plotted in log scale. Similar to the calculations shown in Figure 4.33, we consider a pinned droplet with fixed pressure and increasing A_2 . The numerical result is obtained in a way similar to that described for Figure 4.33 above. The asymptotic approximation is calculated by (4.131). From Figure 4.34, we observe that the formulation given by (4.131) provides a good analytical description of the numerical results.

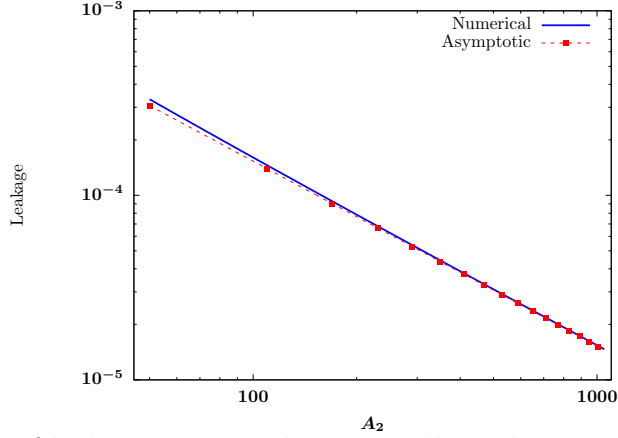


FIGURE 4.34: Mass of leakage computed numerically and asymptotically for a solution on branch 3 plotted in log scale. The asymptotic prediction is given by (4.131). The pressure \bar{p} is fixed as A_2 increases, with parameters $\bar{p} = 0.29159$, $L = 6$, $s = 3$, $A_1 = 1$, $\epsilon = 0.1$.

4.5 Axisymmetric solution

We can easily extend our results for thin films on 1-D heterogeneous substrates presented in Section 4.2 to axisymmetric solutions on a 2-D heterogeneous substrates. In this section, we study the steady-state axisymmetric solutions on a chemically patterned substrate where the disjoining pressure is given by $\tilde{\Pi}(h, r) = A(r)\Pi(h)$ with

$$A(r) = \begin{cases} A_1 & 0 \leq r \leq s \\ A_2 & s < r \leq L \end{cases} \quad (4.132)$$

If we assume the thin film is axisymmetric, then the evolution of such films on chemically homogeneous substrates with $A(r) \equiv 1$, subject to no-flux boundary condition is governed by (3.42a), as stated in Section 3.2. Here, we consider the steady-states of axisymmetric thin films on substrates with patterning of the form (4.132). Subject to no-flux boundary conditions given by (3.42b), for each \bar{p} , the steady-state equation for $h(r; \bar{p})$ is given by

$$\frac{1}{r} \frac{d}{dr} \left(r \frac{dh}{dr} \right) - A(r)\Pi(h) + \bar{p} = 0 \quad (4.133)$$

Using product rule to expand (4.133) and multiplying both sides of the equation by r , we obtain

$$rh'' + h' - rA(r)\Pi(h) + \bar{p}r = 0 \quad (4.134a)$$

$$h'(0) = h'(L) = 0 \quad (4.134b)$$

For simplicity of notation, we use $h(r)$ to denote $h(r; \bar{p})$ for a given pressure \bar{p} . The mass of the axisymmetric solutions $h(r)$ is previously given in Section 3.2 by

$$m = \int_0^L h(r)rdr \quad (4.135)$$

In this section, we show that we can classify the solutions to (4.134a)-(4.134b) into six different branches (branch 1-branch 6), which are similar to the six types of 1-D solutions described in Section 4.2. For each of the six branches, we present results of asymptotic analysis, which are qualitatively the same as those derived for the 1-D steady-states on heterogeneous substrates discussed in Section 4.2.

4.5.1 *Small-thickness films*

Like in 1-D, branch 1 consists of steady-state solutions with small mass m for $m = O(\epsilon L)$. We consider branch 1 of axisymmetric solutions in the limit $\epsilon \rightarrow 0$ and show that the results of asymptotic analysis are the same as those of branch 1 solutions derived in Section 4.2.1. Since the disjoining pressure $\Pi(h)$ changes rapidly for h near $h = \epsilon$, to seek solution with thickness $h(x) = O(\epsilon)$, we still rescale h by writing $h = \epsilon^a H$ for some $a > 0$. We seek solution of the form $H = H_0 + \epsilon H_1 + O(\epsilon^2)$. Substituting $h = \epsilon^a H$ into (4.134a), we obtain

$$\epsilon^a r H'' + \epsilon^a H' - r A(r) \Pi(\epsilon^a H) + \bar{p} r = 0 \quad (4.136)$$

At leading order, we obtain $A(r)\Pi(\epsilon^a H_0) = \bar{p}$, which is exactly the same leading order equation as (4.12a)-(4.12b) for branch 1 solutions in 1-D. It follows that to

leading order, away from the interface of the A_1 and A_2 region, $h(r) = h_{\min 1}$ for $0 \leq r \ll s$ and $h(r) = h_{\min 2}$ for $s \ll r \leq s$. At order $O(\epsilon^a)$, by applying a Taylor expansion of (4.136) near $H = H_0$, we get

$$rH_1'' + H_1' - rA(r)\Pi'(h_{\min i})H_1 = 0 \quad (4.137)$$

Since $\Pi(h)$ changes rapidly on $\left(0, \frac{4\epsilon}{3}\right)$, $\Pi'(h_{\min i}) = O\left(\frac{1}{\epsilon^2}\right) \gg 1$ in the limit $\epsilon \rightarrow 0$.

We introduce a small positive parameter σ_i for $\sigma_i = \frac{1}{\Pi'(h_{\min i})} \ll 1$. It follows that (4.137) becomes a boundary layer equation. On the A_i region, (4.137) is given by

$$\sigma_i r H_1'' + \sigma_i H_1' - r A_i H_1 = 0 \quad (4.138)$$

At $O(1)$, the outer solution of the problem is given by $H_1 \equiv 0$. To obtain the inner solution which characterizes a boundary layer near $x = s$, we rescale the variable r by letting $R = \frac{r-s}{\sigma_i^b}$ for some $b > 0$. Then (4.138) can be written in terms of R as

$$\sigma_i^{1-2b}(s + R\sigma_i^b)H_1'' + \sigma_i^{1-b}H_1' - (s + R\sigma_i^b)A_i H_1 = 0 \quad (4.139)$$

This suggests $b = \frac{1}{2}$. For the A_i region, we arrive at the same leading order equation for H_1 as in the 1-D scenario.

$$H_1'' - A_i H_1 = 0 \quad (4.140)$$

As a result, the asymptotic analysis results derived for branch 1, specifically (4.18), (4.20), and (4.22a)-(4.22b) in 1-D all follow. To leading order, $h(0) \sim h_{\min 1}$ and $h(L) \sim h_{\min 2}$. For axisymmetric solution, the mass of solution on branch 1 is asymptotically given by

$$\begin{aligned} m &= \int_0^L h(r) r dr \\ &= \frac{1}{2} h_{\min 1} s^2 + \frac{1}{2} h_{\min 2} (L^2 - s^2) + O(\epsilon^2) \end{aligned} \quad (4.141)$$

Figure 4.35 (a) and (b) show the film mass and $h(0)$, $h(L)$ plotted as a function of pressure for branch 1 of axisymmetric solutions. In both figures, the solid curves represent the numerically computed solution. The dashed and dotted curves represent the asymptotically computed solutions. Specifically, in Figure 4.35 (a), the asymptotic prediction of mass is calculated using (4.141). In Figure 4.35 (b), the asymptotic predictions for $h(0)$ and $h(L)$ are calculated using the outer solution $h(0) \sim h_{\min 1}$ and $h(L) \sim h_{\min 2}$. The numerical results show that the asymptotic predictions give good approximations of the true branch 1 solutions.

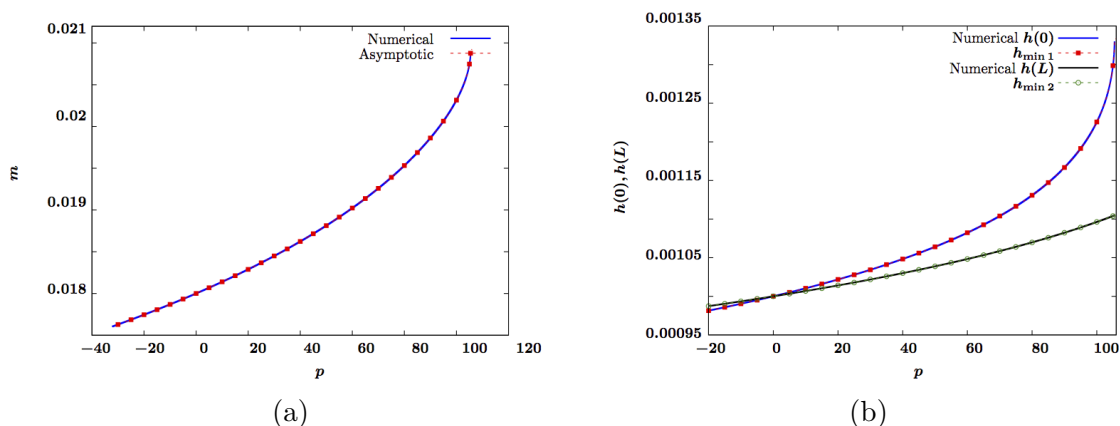


FIGURE 4.35: (a) Bifurcation diagram for m vs. p computed numerically and asymptotically for branch 1 of axisymmetric solutions in the limit of small ϵ . The asymptotic prediction of mass m for each given p is computed using (4.141). (b) Bifurcation diagram for $h(0), h(L)$ vs. p computed numerically and asymptotically for branch 1 of axisymmetric solutions in the limit of small ϵ . The asymptotic predictions are given by $h(0) \sim h_{\min 1}$ and $h(L) \sim h_{\min 2}$ respectively. In both (a) and (b), $L = 6$, $s = 3$, $A_1 = 1$, $A_2 = 1.5$, $\epsilon = 0.001$.

4.5.2 Large-thickness films

Similar to 1-D solutions, the steady-state axisymmetric solutions also have a branch of solutions analogous to branch 6 in 1-D as described in Section 4.2.2. This branch of solutions is characterized by large mean film thickness, large mass and small amplitude. As the film mass increases on this branch, the profile of the solution

can be described as an increasingly small-amplitude perturbation from flat film. To derive an asymptotic prediction for the steady-state profiles of this branch, we seek solution of the form $h(r) = \bar{h} + \delta h_1(r)$ for $\bar{h} = \frac{2m}{L^2}$, $\delta = \Pi\left(\frac{2m}{L^2}\right) \ll 1$ in the limit $m \rightarrow \infty$. Substituting the expansion $h(r) = \bar{h} + \delta h_1(r)$ into (4.134a), at $O(\delta)$, for each A_i region, we obtain

$$\delta r h_1'' + \delta h_1' - \delta r A_i - \delta r A_i \Pi'(\bar{h}) h_1 + \bar{p} r = 0 \quad (4.142)$$

To balance the equation at $O(\delta)$, we assume $p = O(\delta)$ and show that this is consistent with the asymptotic analysis as a result of this dominance balance. We scale \bar{p} by writing $\bar{p} = \delta p_0$ for some $p_0 = O(1)$. At $O(\delta)$, (4.142) can be written as

$$r h_1'' + h_1' - r A_i - r A_i \Pi'(\bar{h}) h_1 + p_0 r = 0 \quad (4.143)$$

Solving (4.143) on the A_1 region $[0, s)$, we get

$$h_1(r) = B_1 J_0(\sqrt{-A_1 \Pi'(\bar{h})} r) + B_2 Y_0(\sqrt{-A_1 \Pi'(\bar{h})} r) + \frac{-A_1 + p_0}{A_1 \Pi'(\bar{h})} \quad (4.144)$$

where $J_0(r)$ and $Y_0(r)$ are Bessel function of the first and second kind of order 0 and B_1, B_2 are constants. Due to the boundary condition $h'(0) = 0$ which is required to ensure regularity of the solution, we need $h_1'(0) = 0$ so $B_2 = 0$.

Solving (4.143) on the A_2 region $(s, L]$, we get

$$h_1(r) = B_3 J_0(\sqrt{-A_2 \Pi'(\bar{h})} r) + B_4 Y_0(\sqrt{-A_2 \Pi'(\bar{h})} r) + \frac{-A_2 + p_0}{A_2 \Pi'(\bar{h})} \quad (4.145)$$

for some constant B_3 and B_4 . Together, this suggests $h(r) = \bar{h} + \delta h_1(r)$, which written in terms of \bar{p} is given by

$$h(r) \sim \begin{cases} \bar{h} + C_1 J_0(\sqrt{-A_1 \Pi'(\bar{h})} r) - \frac{A_1 \Pi(\bar{h}) - \bar{p}}{A_1 \Pi'(\bar{h})} & 0 \leq x \leq s \\ \bar{h} + C_2 J_0(\sqrt{-A_2 \Pi'(\bar{h})} r) + C_3 Y_0(\sqrt{-A_2 \Pi'(\bar{h})} r) - \frac{A_2 \Pi(\bar{h}) - \bar{p}}{A_2 \Pi'(\bar{h})} & s < x \leq L \end{cases} \quad (4.146)$$

for some constant C_1, C_2 , and C_3 . To determine these three constants, we use the continuity and differentiability condition given by (4.8a) and (4.8b). In addition, we also require $h'_1(L) = 0$. These three conditions allow us to solve C_1, C_2 and C_3 in terms of pressure \bar{p} . To determine \bar{p} , we use the mass condition

$$\int_0^L h(r) r dr = \int_0^L (\bar{h} + \delta h_1) r dr = m = \frac{1}{2} \bar{h} L^2 \quad (4.147)$$

which, at $O(\delta)$, reduces to

$$\int_0^L h_1(r) r = 0 \quad (4.148)$$

In the limit of large mass, we obtain

$$\begin{aligned} \bar{p} &\sim \frac{\epsilon^2 (A_1 s^2 + A_2 L^2 - A_2 s^2)}{L^2 \bar{h}^3} + O\left(\frac{\epsilon^3}{L^2 \bar{h}^4}\right) \\ &\sim \frac{\epsilon^2 (A_1 s^2 + A_2 L^2 - A_2 s^2) L^4}{8m^3} + O\left(\frac{\epsilon^3 L^6}{m^4}\right) \end{aligned} \quad (4.149)$$

Note that (4.149) suggests that $\bar{p} = O\left(\frac{1}{m^3}\right) = O(\delta)$ in the limit of large m , which is consistent with our earlier assumption that $\bar{p} = O(\delta)$. Plugging the asymptotic prediction (4.149) into (4.146), we obtain an asymptotic estimate for $h_{\max} = h(0)$ and $h_{\min} = h(L)$. We have

$$h(0) - \bar{h} \sim -\frac{1}{8} \frac{(4L^2 \ln(\frac{L}{s}) - L^2 + s^2)(A_1 - A_2)\epsilon^2 s^2}{L^2 \bar{h}^3} \quad (4.150a)$$

$$h(L) - \bar{h} \sim \frac{1}{8} \frac{\epsilon^2 s^2 (L^2 - s^2)(A_1 - A_2)}{L^2 \bar{h}^3} \quad (4.150b)$$

Figure 4.36 shows mass vs. pressure computed numerically and asymptotically for branch 6 plotted in log scale in the limit of large mass. The solid blue curve represents the numerically computed solution. The dashed dotted red curve represents the asymptotic prediction given by (4.149). The numerical simulation results suggest

that the asymptotic analysis in the limit of large m produces predictions that agree well with the numerical results.

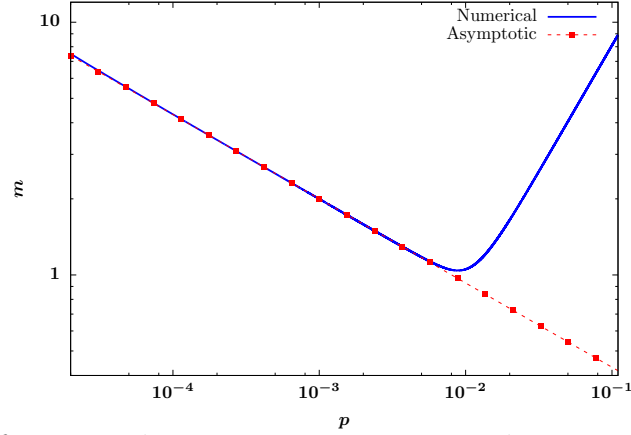


FIGURE 4.36: Bifurcation diagram m vs. p computed numerically and asymptotically for branch 6 for large m in log scale, with parameters $L = 6$, $s = 3$, $A_1 = 1$, $A_2 = 1.5$, $\epsilon = 0.001$

4.5.3 Small-radii droplets

Similar to branch 2 of the 1-D steady-state solutions, branch 2 of axisymmetric solutions is also a class of droplet-type solutions with width $w \leq s$. To study the steady-state solutions on branch 2, we first multiply both sides of the steady-state equation (4.134a) by $h'(r)$. After multiplication, we can rewrite (4.134a) as

$$\frac{d}{dr} \left[\frac{1}{2} h'^2 - A_i U(h) + ph \right] = -\frac{h'^2}{r} \quad (4.151)$$

Now we integrate (4.151) on $[0, s]$ and $[s, L]$ respectively. We have

$$\frac{1}{2} h'(s)^2 - A_1 U(h(s)) + \bar{p}h(s) + A_1 U(h_{\max}) - \bar{p}h_{\max} = \int_0^s -\frac{h'(r)^2}{r} dr \quad (4.152a)$$

$$-\frac{1}{2} h'(s)^2 + A_2 U(h(s)) - \bar{p}h(s) - A_2 U(h_{\min}) + \bar{p}h_{\min} = \int_s^L -\frac{h'(r)^2}{r} dr \quad (4.152b)$$

Combining (4.152a)-(4.152b) and rearranging terms, we obtain

$$(A_2 - A_1)U(h(s)) = A_2 U(h_{\min}) - A_1 U(h_{\max}) + \bar{p}(h_{\max} - h_{\min}) + \int_0^L -\frac{h'^2}{r} dr \quad (4.153)$$

(4.153) is analogous to (4.69) in Section 4.2.3 and exact for all steady-state axisymmetric solutions. Now we present asymptotic analysis for this branch of solutions in the limit $\epsilon \rightarrow 0$. For a droplet-type solutions with $A_1 = O(1)$, $h(0) = h_{\max} = O(1)$. In the limit $\epsilon \rightarrow 0$, we have $\Pi(h) \ll 1$. At $O(1)$, for $0 \leq r \ll w$, (4.134a) can be described by

$$rh'' + h' + \bar{p}r \sim 0 \quad (4.154)$$

Note that this is the same equation obtained for steady-state axisymmetric droplets on homogeneous substrates discussed in Section 3.2. The solution to (4.154) is given by

$$h(r) \sim C_1 \ln(r) + C_2 - \frac{1}{4}\bar{p}r^2 \quad (4.155)$$

for some constant C_1 and C_2 . For $0 \leq r \ll w$, apply the boundary condition $h'(0) = 0$ and $h(0) = h_{\max}$, we have $C_1 = 0$ and $C_2 = h_{\max}$. This shows in the limit $\epsilon \rightarrow 0$, the droplet core of a branch 2 solution can be described by

$$h(r) = -\frac{1}{4}\bar{p}r^2 + h_{\max} + O(\epsilon) \quad (4.156)$$

which is still a parabola as in the 1-D scenario, but with a modified coefficient. In particular, this suggests that $\frac{h'(r)^2}{r} \sim \frac{1}{4}\bar{p}^2r$ near $r = 0$ and that $\int_0^s -\frac{h'(r)^2}{r}dr$ is not a singular integral. We estimate the width of the droplet w from (4.156) by solving $h(w) \sim 0$, which means

$$h_{\max} \sim \frac{1}{4}\bar{p}w^2 \quad (4.157)$$

If the droplet width $w \leq s$, then $h(x)$ decays to $h(x) \sim \epsilon$ for $w \ll x \leq L$, an ultra-thin film region. This suggests for $w \ll x \leq L$, $h(s) \sim \epsilon$, $h_{\min} \sim \epsilon$, $h'(r) \sim 0$ and as a consequence,

$$\int_0^L \frac{h'^2}{r}dr \sim \int_0^w \frac{h'^2}{r}dr \quad (4.158)$$

It follows that at $O(1)$, (4.153) is given by

$$-A_1 U(\epsilon) = -A_1 U(h_{\max}) + \bar{p} h_{\max} + \int_0^w -\frac{h'(r)^2}{r} dr \quad (4.159)$$

Substituting the leading order prediction of the droplet profile $h(r)$ given by (4.156) into the right hand side of (4.159), we have

$$h_{\max} \sim \frac{A_1}{6\bar{p}} + \frac{1}{8}\bar{p}w^2 \quad (4.160)$$

Combining (4.157) with (4.160), we obtain a width estimate for the droplet in terms of \bar{p} , given by

$$w \sim \frac{2\sqrt{A_1}}{\sqrt{3\bar{p}}} \quad (4.161)$$

Accordingly, the maximum film thickness of branch 2 is given by

$$h_{\max} \sim \frac{A_1}{3\bar{p}} \quad (4.162)$$

At leading order, the steady-state solutions depend on A_1 just like branch 2 solutions in 1-D. Note that in 1-D, in the limit $\epsilon \rightarrow 0$, we showed the maximum film thickness of branch 2 solutions is given by $h_{\max} = \frac{A_1}{6\bar{p}}$. Branch 2 of the axisymmetric solutions are characterized by qualitatively the same features as branch 2 of the 1-D solutions.

4.5.4 Pinned droplets

Branch 3 of axisymmetric solutions is a branch of solutions characterized by droplets “pinned” at $x = s$. This class of droplets has width $w \sim s$. We first study this class of solutions in the limit $\epsilon \rightarrow 0$ for $A_1, A_2 = O(1)$. For a droplet-type solution, $h_{\max} = O(1) \gg \epsilon$. In the droplet core, $A_1 \Pi(h) = O(\epsilon^2) \rightarrow 0$. At $O(1)$, the steady-state equation for droplet core is described by (4.154). It follows that the droplet

profile can still be described by (4.156). For this class of “pinned” droplets, droplet width is given by $w \sim s$. Hence, at leading order,

$$h_{\max} \sim \frac{1}{4}\bar{p}s^2 \quad (4.163)$$

In the droplet core, the droplet profile is described by

$$h(r) \sim \frac{1}{4}\bar{p}(s^2 - r^2) \quad (4.164)$$

To compute an estimate of $h(s)$ for this branch of solutions for $A_1, A_2 = O(1)$ as $\epsilon \rightarrow 0$, we use (4.153). Since for $s \leq r \leq L$, the droplet has width $w \sim s$, $h(r) \sim \epsilon$ and $h'(r) \sim 0$, it follows that $\int_0^L -\frac{h'^2}{r} dr \sim \int_0^s -\frac{h'^2}{r} dr$. For $0 \leq r \ll s$, we use the leading order prediction given by $h(r) = \frac{1}{4}\bar{p}(s^2 - r^2)$, so $h'(r) \sim -\frac{1}{2}\bar{p}r$. At $O(1)$, (4.153) for branch 3 is given by

$$(A_2 - A_1)U(h(s)) = A_2U(\epsilon) + \frac{1}{8}\bar{p}^2s^2 \quad (4.165)$$

Hence, an estimate of $h(s)$ can be computed by solving

$$U(h(s)) \sim \frac{-\frac{A_2}{6} + \frac{1}{8}\bar{p}^2s^2}{A_2 - A_1} \quad (4.166)$$

Since on branch 2, the droplets have width $w \leq s$ and on branch 3, the droplets have width $w \sim s$, branch 2 terminates at $p_{2,3}^*$ when $w(p_{2,3}^*) \sim s$, which indicates branch 2 ends at

$$p_{2,3}^* \sim \frac{2\sqrt{A_1}}{\sqrt{3}s} \quad (4.167)$$

It follows that branch 2 intersects with branch 3 when $w \sim \frac{2\sqrt{A_1}}{\sqrt{3}\bar{p}} \sim s$, i.e. at $\bar{p} \sim \frac{2\sqrt{A_1}}{\sqrt{3}s}$. Branch 4 intersects with branch 3 when $w \sim \frac{2\sqrt{A_2}}{\sqrt{3}\bar{p}} \sim s$, i.e. at

$$\bar{p} \sim \frac{2\sqrt{A_2}}{\sqrt{3}s}.$$

If we investigate the axisymmetric steady-state solutions in the limit $A_2 \rightarrow \infty$ as we did in Section 4.2.3, we divide both sides of (4.153) by A_2 and write $\delta = \frac{1}{A_2}$ for $\delta \ll 1$. (4.153) can be written as

$$(1 - \delta A_1)U(h(s)) = U(h_{\min}) - \bar{p}h_{\min} - \delta A_1 U(h_{\max}) + \delta \bar{p}h_{\max} + \delta \int_0^L -\frac{h'(r)^2}{r} dr \quad (4.168)$$

(4.168) is analogous to (4.77) in 1-D. Following the derivation similar to (4.77)-(4.87) in Section 4.2.4, in the limit of large A_2 , we obtain

$$h(s) \sim \epsilon + \epsilon \sqrt{\delta} \sqrt{-\frac{A_1}{3} + \frac{1}{4}\bar{p}^2 s^2} \quad (4.169)$$

Substituting (4.169) into (4.152a) and following a similar process as illustrated in (4.84)-(4.87), we obtain

$$h'(s) = -\sqrt{-\frac{A_1}{3} + \frac{1}{2}\bar{p}^2 s^2} + O(\delta) \quad (4.170)$$

This shows the pinned droplet on branch 3 of axisymmetric films for each given pressure \bar{p} has a contact angle that approaches $\theta = \sqrt{-\frac{A_1}{3} + \frac{1}{2}\bar{p}^2 s^2}$ in the limit of large A_2 . Note that in 1-D, the leading order prediction of the contact angle for branch 3 is $\theta = \sqrt{-\frac{A_1}{3} + \bar{p}^2 s^2}$. The results of asymptotic analysis for branch 3 of axisymmetric solutions are qualitatively the same as those of the 1-D solutions.

4.5.5 Large-radii droplets

Branch 4 of axisymmetric solutions is a class of droplet-type solutions with large droplet width $s \leq w \leq L$. First, we study the solutions in the limit $\epsilon \rightarrow 0$ for $A_1, A_2 = O(1)$. For this class of large-width droplets, since $w \leq s$, $h(s) = O(1)$. In

the limit $\epsilon \rightarrow 0$, in the droplet core, $h = O(1)$ and thus $\Pi(h) = O(\epsilon^2) \ll 1$. Hence, at $O(1)$, the steady-state axisymmetric equation (4.134a) is given by

$$rh'' + h' + \bar{p}r \sim 0 \quad (4.171)$$

which is the same leading order steady-state equation as (4.154). It follows that the profile of the droplet core is described by (4.156), i.e.

$$h(r) \sim -\frac{1}{4}pr^2 + h_{\max} \quad (4.172)$$

Similarly, a width estimate of the droplet can be computed by setting $h(w) \sim 0$, which yields

$$h_{\max} \sim \frac{1}{4}\bar{p}w^2 \quad (4.173)$$

To compute h_{\max} for branch 4, we use (4.153), derived previously in Section 4.5.1, i.e.

$$(A_2 - A_1)U(h(s)) = A_2U(h_{\min}) - A_1U(h_{\max}) + \bar{p}(h_{\max} - h_{\min}) - \int_0^L \frac{h'^2}{r} dr \quad (4.174)$$

Since the droplets have width $s \leq w \leq L$, the solutions $h(r)$ decay to $h \sim \epsilon$ for $w \leq r \leq L$ so $h_{\min} \sim \epsilon$. Under the additional assumption that $A_1, A_2 = O(1)$, $h(s), h_{\max} = O(1)$, at leading order, (4.174) is given by

$$A_2U(\epsilon) + \bar{p}h_{\max} - \int_0^L \frac{h'^2}{r} dr = 0 \quad (4.175)$$

Using the leading order profile (4.172) and (4.173) derived in the limit $\epsilon \rightarrow 0$ and

$\int_0^L -\frac{h'^2}{r} dr \sim \int_0^w -\frac{h'^2}{r} dr$, we can further reduce (4.175) to

$$h_{\max} \sim \frac{A_2}{3\bar{p}} \quad (4.176)$$

It follows that the width of the droplet is given by

$$w \sim 2\sqrt{\frac{h_{\max}}{\bar{p}}} \sim \frac{2\sqrt{A_2}}{\sqrt{3\bar{p}}} \quad (4.177)$$

To study the steady-states in the limit $A_2 \rightarrow \infty$ for fixed $A_1 = O(1)$, we use the same equation (4.168). Using a similar argument as presented by (4.101)-(4.106) for branch 4 in the 1-D case, we obtain qualitatively the same results for axisymmetric solutions. At leading order, the maximum film thickness h_{\max} and the droplet profile are still described by (4.176) and (4.172) respectively in the large A_2 limit.

4.5.6 Large confined droplets

Similar to branch 5 of the 1-D solutions, branch 5 of axisymmetric solutions is also characterized by large confined droplets where all of the droplets on this branch have width $w \sim L$ regardless of pressure and mass to leading order. Now we study the properties of this class of axisymmetric solutions in the limit $\epsilon \rightarrow 0$ for $A_1, A_2 = O(1)$. In the droplet core, $h = O(1)$ so $\Pi(h) = O(\epsilon^2) \ll 1$. At leading order, the steady-state equation (4.134a) is given by

$$rh'' + h' + \bar{p}r \sim 0 \quad (4.178)$$

It follows that the profile of the droplet core is given by the parabola

$$h(r) \sim -\frac{1}{4}\bar{p}r^2 + h_{\max} \quad (4.179)$$

Since all of the droplets on branch 5 have width $w \sim L$, at leading order, the maximum film thickness h_{\max} is described in terms of L by

$$h_{\max} \sim \frac{1}{4}\bar{p}L^2 \quad (4.180)$$

To compute h_{\min} , we use (4.153). For branch 5, $h(s) = O(1)$ and $h_{\min} = O(\epsilon)$. At leading order, (4.153) is given by

$$A_2 U(h_{\min}) + \bar{p} h_{\max} + \int_0^L -\frac{h'(r)^2}{r} dr = 0 \quad (4.181)$$

Substituting (4.179) and (4.180) into (4.181), we have

$$A_2 U(h_{\min}) = \frac{1}{8} \bar{p}^2 L^2 \quad (4.182)$$

Note this is extremely similar to branch 5 of 1-D solutions discussed in Section 4.2.6, only with the coefficient modified. By using a similar argument presented by (4.114)-(4.115) for 1-D solutions, we can show that in the limit of large A_2 , h_{\max} and h_{\min} are still described by (4.180) and (4.182).

4.5.7 Numerical simulation results

To validate the results of the asymptotic analysis derived in Section 4.5.1-4.5.6, we compare the asymptotic prediction with the numerical solution of the bifurcation diagram for p vs. h_{\max} . Figure 4.37 (a) and (b) show the bifurcation diagram $h(0) = h_{\max}$ vs. \bar{p} computed for small and large \bar{p} respectively. The solid curve represents the numerically computed bifurcation curve. The dashed and dotted curve represents the asymptotic prediction of h_{\max} derived for each branch in the limit of small ϵ . The simulation results show that our asymptotic predictions agree well with the numerical solutions.

4.6 Summary

In this chapter, we first presented the formulation of the steady-state equation for thin films on a finite chemically heterogeneous substrate with stepwise patterning. In Section 4.1, through numerical simulations, we compared the bifurcation diagrams

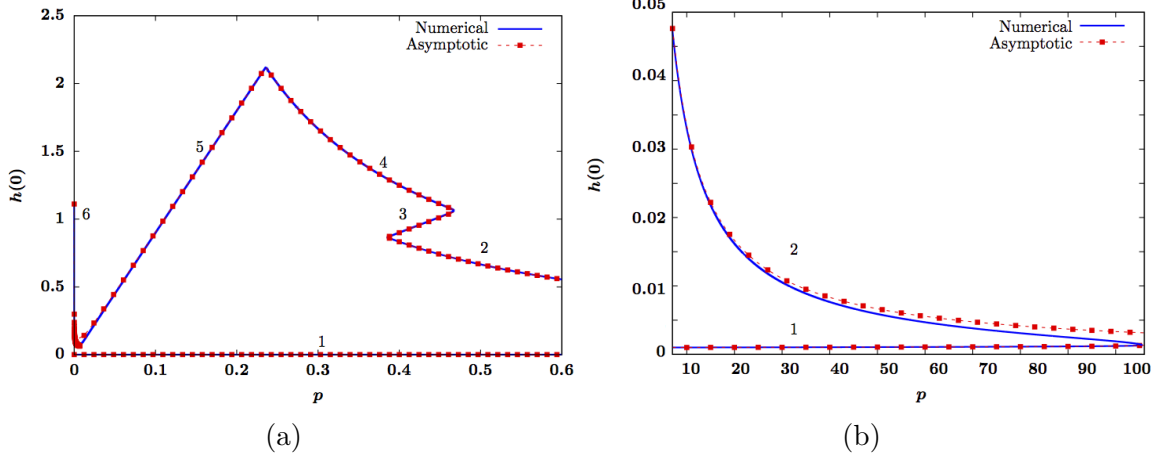


FIGURE 4.37: Bifurcation diagram for $h(0) = h_{\max}$ vs. p for (a) small p (b) large p . In both (a) and (b), $A_1 = 1$, $A_2 = 1.5$, $L = 6$, $s = 3$, $\epsilon = 0.001$.

for m vs. h_{\max}, h_{\min} for the heterogeneous substrate and the homogeneous substrate in 1-D. We identified the existence of two loops, namely an outer loop and an inner loop, in the bifurcation diagram. We showed through numerical simulations that the inner loop degenerates and vanishes in the limit of large A_2 .

In Section 4.2, we classified the 1-D steady-state solutions that could exist on a finite stepwise-patterned substrate subject to no-flux boundary conditions into six different branches, which correspond to the six different segments in the bifurcation diagram for p vs. h_{\max} . For each branch, we presented asymptotic analysis for the droplet profile in two limits, i.e. small ϵ limit in the presence of small fixed wettability contrast and large A_2 limit describing a large wettability contrast. In particular, we discussed an entirely new branch of solutions that arises from the heterogeneity of the substrate. We showed that depending on the branch, the leading order droplet profile depends on the different parameters of the model.

In Section 4.3, we presented the linear stability analysis for 1-D steady-state solutions on heterogeneous substrates discussed in Section 4.2. By computing the stability for one chosen set of parameters, we demonstrated that branch 5 is the only

unstable branch. Through time-dependent PDE simulations, we also showed that depending on the initial perturbation, a branch 5 solution with small perturbation could either converge to a branch 6 or branch 4 solution with the same mass, as illustrated in Figure 4.29 (a) and (b). In Section 4.4, we discussed the confining effect of large A_2 on some steady-state branches. To quantify the leakage of fluid film from the A_1 into the A_2 region, we present a measure for the leakage and show that the leakage is inversely proportional to A_2 in the limit of large A_2 .

Finally, in Section 4.5, we investigated the axisymmetric solutions on a heterogeneous substrate with a stepwise axisymmetric patterning. We showed that the results of the asymptotic analysis derived for 1-D solutions can be easily extended to the axisymmetric solutions and that the profiles of the axisymmetric solutions are qualitatively the same as those of 1-D solutions studied in Section 4.2.

Dynamics of thin film droplets

A layer of thin liquid film on a solid substrate can become unstable due to the presence of intermolecular forces [25, 29, 56]. The instabilities lead to the dewetting of thin film and formation of droplets [5, 7]. These droplets evolve by two means, namely spatial translation and mass exchange between droplets. The spatial translation of droplets leads to collision followed by merging of droplets. Mass exchange between neighboring droplets leads to mass loss and collapse of individual droplets. As a result of these mechanisms, the number of droplets decreases over time [25]. This process is known as coarsening. Glasner and Witelski first showed how the lubrication equation modeling the evolution of thin liquid film could be reduced to a finite-dimensional ODE system, which describes the dynamics of droplets through the droplet pressure and position [26, 40]. The reduced ODE model gives rise to a further simplified model for the coarsening dynamical system, which allows for the statistical analysis of the dynamics of a large array of droplets. The accuracy of the reduced model for a single droplet is important for providing an accurate basis for the description of the dynamics of a large system of droplets.

In this chapter, we first review the reduced ODE approximation proposed by Glasner and Witelski. We show that the original ODE model, which was derived by introducing a slow time scale and using an asymptotic expansion in terms of fluxes, becomes less accurate as the imposed fluxes increase. We then present a refined model by making a modification to the original asymptotic expansion proposed by Glasner and Witelski. Through analysis and numerical simulations, we compare the refined model with both the full PDE and the original ODE model. We illustrate the improvement in the prediction accuracy of a single-droplet dynamics given by the refined model compared to the original ODE model subject to the same fluxes at the boundary.

5.1 Review of the finite-dimensional ODE approximation

In the long-time evolution of thin films, the droplets formed will move and change mass in response to the fluxes imposed at the boundary. Glasner and Witelski have previously studied the thin film evolution on a finite domain $[-L, L]$ for some large L with small fluxes imposed at the boundary [26]. Let $\sigma > 0$ be a small parameter representing the order of magnitude of flux. They considered the thin film equation (3.1) on $[-L, L]$, i.e.

$$\frac{\partial h}{\partial t} = \frac{\partial}{\partial x} \left(h^3 \frac{\partial p}{\partial x} \right) \quad (5.1)$$

subject to small flux at the boundary described by (5.2) and (5.3).

$$J(-L) = \sigma J_-, \quad J(L) = \sigma J_+ \quad (5.2)$$

$$\frac{\partial^3 h}{\partial x^3}(\pm L) = 0 \quad (5.3)$$

Note that this is a different choice of boundary conditions from that presented in Chapter 3 where $\frac{\partial h}{\partial x}(\pm L) = 0$. They considered initial conditions given by a homo-

clinic steady-state droplet $\bar{h}(x; \bar{p})$ truncated at $x = \pm L$, i.e.

$$h(x, 0) = \bar{h}(x; \bar{p}) \quad (5.4)$$

When flux is small, the thin film evolves slowly. Since the evolution is slow, they introduced a slow time scale $\tau = \sigma t$. In presence of small fluxes, the thin film profile $h(x, t)$ on $[-L, L]$ describing the evolution of a single droplet is close to the steady-state solution $\bar{h}(x - X(\tau), P(\tau))$ where $X(\tau)$ denotes the position of the droplet and $P(\tau)$ denotes the pressure of the droplet. The position of the droplet is defined as the maximum of the thin film thickness. Specifically, for each steady-state, they considered the homoclinic solution for each $\bar{p} = P(\tau)$, which connects the saddle point $(h, h_x) = (h_{\min}, 0)$ with the maximum film thickness $(h, h_x) = (h_{\max}, 0)$ in the phase plane. As described in Chapter 3, the homoclinic droplet exists on an infinite domain where in the ultra-thin film region, $\bar{h}(x; \bar{p}) - h_{\min}$ is exponentially small. For sufficiently large L , the influence of the approximation at the boundary is negligible. To fit the droplet on a finite domain $[-L, L]$, Glasner and Witelski used a homoclinic solution whose tail is cut off at $x = \pm L$. Assuming that the flux is $O(\sigma)$, they wrote the thin film profile $h(x, t)$ as a small perturbation from the steady-state droplet with position $X(\tau)$ and pressure $P(\tau)$, given by

$$h(x, t) = \bar{h}(x - X(\tau); P(\tau)) + \sigma h_1(x, \tau) + O(\sigma^2) \quad (5.5)$$

Substituting the asymptotic expansion (5.5) into the full PDE (5.1), at $O(\sigma)$, they obtained a linear equation of h_1 given by

$$-\frac{\partial \bar{h}}{\partial x} \frac{dX}{d\tau} + \frac{\partial \bar{h}}{\partial \bar{p}} \frac{dP}{d\tau} = \mathcal{L}h_1 \quad (5.6)$$

where \mathcal{L} is a linear operator defined by

$$\mathcal{L}g = (\bar{h}^3(\Pi'(\bar{h})g - g_{xx})_x)_x \quad (5.7)$$

Note that the adjoint operator of \mathcal{L} is given by

$$\mathcal{L}^*g = \left(\Pi'(\bar{h}) - \frac{\partial^2}{\partial x^2} \right) \left(\frac{\partial}{\partial x} \left(\bar{h}^3 \frac{\partial g}{\partial x} \right) \right) \quad (5.8)$$

They found that the null space of \mathcal{L}^* is spanned by two functions, $\psi_1(x)$ and $\psi_2(x)$, given by

$$\psi_1(x) = 1, \quad \psi_2(x) = \int_0^x \frac{\bar{h}(s) - h_{\min}}{\bar{h}(s)^3} ds \quad (5.9)$$

Applying the solvability condition given by the application of Fredholm alternative to (5.6), they arrived at a system of ODEs, which describes the rate of change of $P(\tau)$ and $X(\tau)$, given by (5.10a) and (5.10b) respectively.

$$\frac{dP}{d\tau} = C_P(X, P)(J_+ - J_-) \quad (5.10a)$$

$$\frac{dX}{d\tau} = -C_X(X, P)(J_+ + J_-) \quad (5.10b)$$

Here, C_P and C_X are two coefficients that depend on both X and P given by

$$C_P = \left(\int_{-L}^L \frac{\partial \bar{h}}{\partial \bar{p}}(x - X, P) dx \right)^{-1} \quad (5.11a)$$

$$C_X = \int_{-L}^L \frac{\bar{h} - h_{\min}}{\bar{h}^3} dx \Big/ 2 \int_{-L}^L \frac{(\bar{h} - h_{\min})^2}{\bar{h}^3} dx \quad (5.11b)$$

For each droplet, $\bar{h}(x, \bar{p})$ decays to h_{\min} exponentially for $|x| \gg w$ where w represents a measure of the droplet width. By truncating the integrals at droplet widths and using the odd and even symmetry of $\frac{\partial \bar{h}}{\partial x}$ and $\frac{\partial \bar{h}}{\partial p}$, at leading order, they obtained

$$C_P \sim \left(\int_{-w}^w \frac{\partial \bar{h}}{\partial \bar{p}}(x, P) dx \right)^{-1} \quad (5.12a)$$

$$C_X \sim \int_{-w}^w \frac{\bar{h} - h_{\min}}{\bar{h}^3} dx \Big/ 2 \int_{-w}^w \frac{(\bar{h} - h_{\min})^2}{\bar{h}^3} dx \quad (5.12b)$$

where $\bar{h} = \bar{h}(x, P)$ in the integrals denotes a droplet centered at $x = 0$. We observe from (5.12a)-(5.12b) that if $J_+ = J_-$, then $\frac{dP}{dt} = 0$. This is a pure translation mode where the mass of the droplet is constant at leading order. If $J_+ = -J_-$, then $\frac{dX}{dt} = 0$. This is a pure mass change mode where the position of the droplet remains fixed for all time. The governing equation for thin film is given by $\frac{\partial h}{\partial t} = \frac{\partial J}{\partial x}$. It follows that the total mass change is given by $\frac{dm}{dt} = J_+ - J_-$.

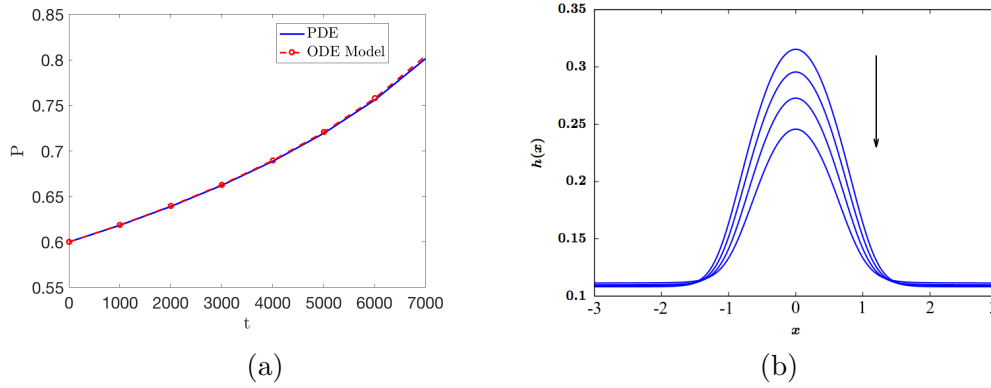


FIGURE 5.1: (a) Pressure evolution of a single droplet computed using the full lubrication PDE numerically and the reduced ODE model. (b) The corresponding profile of the droplet over time. The droplet is in a mass decrease mode with $P(0) = 0.6$, $J_+ = -J_- = -0.1$, $\sigma = 10^{-4}$ and $L = 3$.

When σ is small, the ODE model gives a good prediction of pressure and position of a single droplet. Figure 5.1 (a) shows the evolution of pressure of a single droplet in mass change mode predicted using the full PDE and the simplified ODE model on $[-L, L]$ with $J_+ = -J_- = -0.1$, $\sigma = 10^{-4}$, $L = 3$. Figure 5.1 (b) shows the evolution of the corresponding droplet profile over time. As the droplet loses mass, the droplet shrinks in size. The ODE is solved using forward Euler's method. The exact full PDE for $h(x, t)$ is solved with initial condition $h(x, 0) = \bar{h}(x - X(0), P(0))$ using backward Euler time-stepping scheme and a second order central finite difference

spatial discretization. For the PDE solution, the pressure $p(t)$ is calculated at the maximum of the droplet by

$$p(t) = \mathcal{P}(h(x, t)) \Big|_{x=\arg\max_x h(x, t)} = \Pi(h(x, t)) - h_{xx}(x, t) \Big|_{x=\arg\max_x h(x, t)} \quad (5.13)$$

where \mathcal{P} is an operator that calculates the pressure of a droplet with profile $h(x, t)$ when applied to $h(x, t)$. It is given by the definition of pressure in (2.15). The droplet position is determined by the maximum of the droplet height, which is numerically estimated by first interpolating the discretized PDE solution near its maximum using a parabola and then computing the maximum of the parabola.

Figure 5.2 shows the pressure and position of a droplet in translation mode predicted using both the full PDE and the simplified ODE model on $[-L, L]$ with $J_+ = J_- = 0.1$, $\sigma = 10^{-4}$, $L = 3$. Figure 5.2 (a) shows the pressure evolution of the droplet. According to (5.10a) in the simplified ODE model, the pressure given by the ODE model is constant in time. However, a slow decrease in pressure has been observed from the numerical solution to the PDE over time. When $J_+ = J_-$, the total fluid mass is conserved in time. Truncating the homoclinic solution at $x = \pm L$ has an influence on the droplet profile that can slowly accumulate, leading to inaccuracies of the ODE prediction. Despite the decrease in pressure observed in the PDE solution over time, the decrease occurs at an extremely slow time scale, which can still confirm the overall accuracy of the prediction given by the ODE model. Figure 5.2 (b) shows the position of the droplet calculated from the full PDE and the simplified ODE. In Figure 5.2 (b), the position of the droplet is well approximated by the simplified ODE model for small fluxes. Figure 5.2 (c) illustrates the droplet motion over time. As time increases, the droplet translates towards the right boundary of the domain.

However, as the magnitude of flux increases, the simplified ODE model becomes

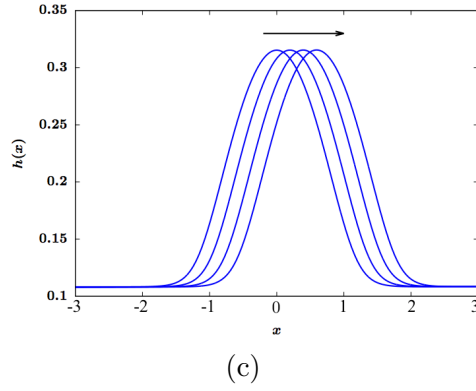
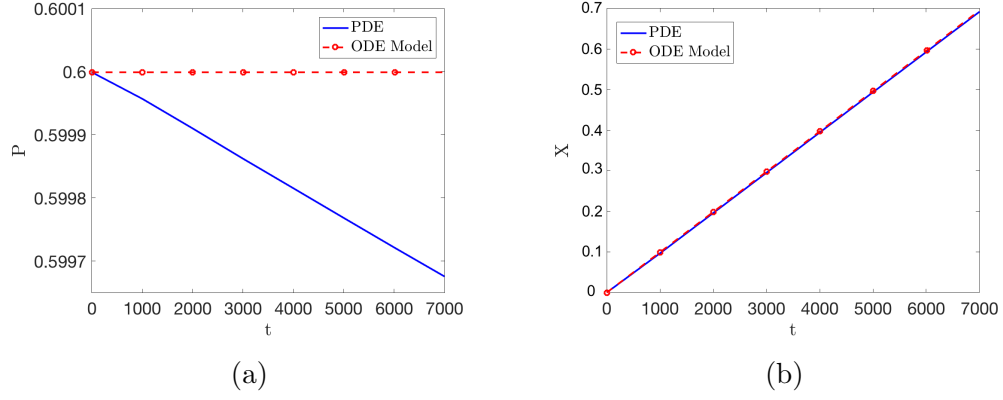


FIGURE 5.2: Pressure and position prediction of a single droplet in translation mode computed from the full lubrication PDE and reduced ODE system. (a) pressure evolution (b) position evolution. (c) droplet profile evolution. $P(0) = 0.6$, $X(0) = 0$, $J_+ = J_- = 0.1$, $\sigma = 10^{-4}$, $L = 3$.

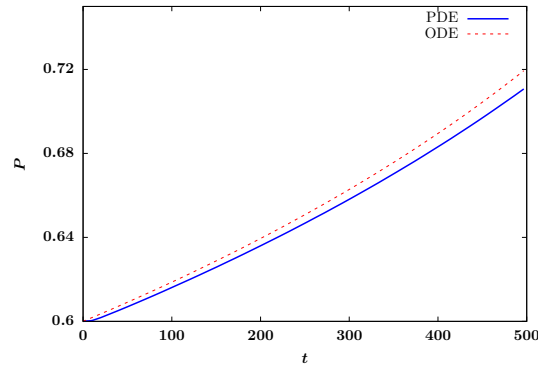


FIGURE 5.3: Pressure of a single droplet in a mass change mode computed from the lubrication PDE and the reduced ODE model, with increased fluxes compared to Figure (5.1). $P(0) = 0.6$, $J_+ = -J_- = -1$, $\sigma = 10^{-4}$, $L = 3$.

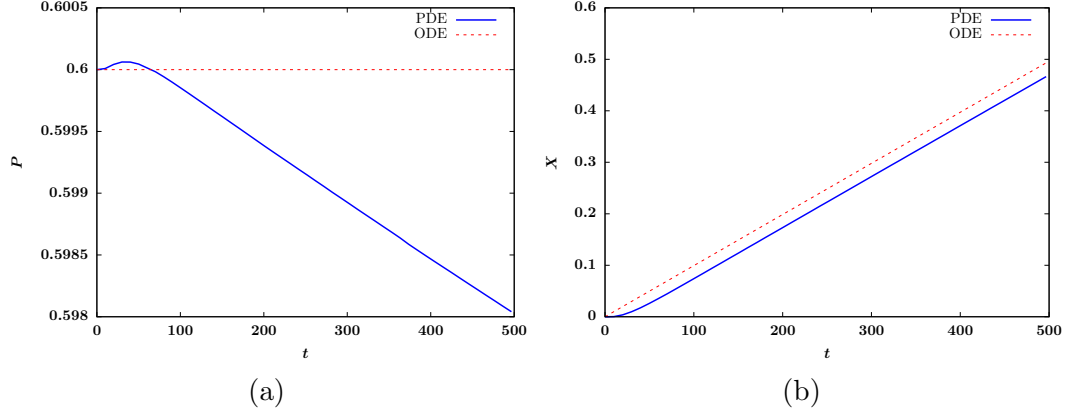


FIGURE 5.4: Pressure and position of a single droplet in translation mode computed from the lubrication PDE and the reduced ODE model, with increased flux compared to Figure (5.2). (a) pressure evolution (b) position evolution. $P(0) = 0.6$, $X(0) = 0$, $J_+ = J_- = 1$, $\sigma = 10^{-4}$, $L = 3$.

less accurate. Figure 5.3 shows the pressure of a droplet in mass decrease mode calculated using both the full PDE and the simplified ODE with the same parameters as in Figure 5.1 except that the magnitude of the flux has been increased to $J_+ = -J_- = -1$. In Figure 5.3, we observe a discrepancy between the pressure predicted by the ODE model and the pressure calculated from the full PDE. Specifically, the ODE model produces a pressure that slightly overestimates the real pressure. This discrepancy grows as time increases.

Similarly, we set the flux $J_+ = J_- = 1$ so that the droplet is now in a translation mode with increased fluxes compared to Figure 5.2. Figure 5.4 (a) shows the pressure of the translating drop predicted by the PDE and ODE model. The ODE model predicts the pressure to be constant. Like in Figure 5.2 (a), a decrease in pressure is also observed in Figure 5.4 (a). Compared to Figure 5.2 where fluxes are one order of magnitude smaller, the droplet pressure decreases more rapidly in presence of larger fluxes, making the ODE model a less accurate description. Figure 5.4 (b) shows the position evolution of the droplet. Compared to Figure 5.2 (b), thin film evolves faster in Figure 5.4 (b). The error of the simplified model increases as a consequence

of larger fluxes. Hence, when fluxes are large, a more accurate model is needed to capture the pressure and position change of a single droplet in response to imposed fluxes.

5.2 Refined model

To improve the pressure and position prediction given by the simplified ODE model, we propose a refined model by modifying the asymptotic expansion (5.5) given by Glasner and Witelski. We consider a solution of the form (5.14). By writing (5.14), we assume $h_1 = h_1(x, t)$ evolves at the fast time scale t , instead of $\tau = \sigma t$ as in (5.5).

$$h(x, t) = \bar{h}(x - X(\tau), P(\tau)) + \sigma h_1(x, t) + O(\sigma^2) \quad (5.14)$$

If we substitute the modified expansion (5.14) into the evolution equation and linearize, we obtain a linear PDE for $h_1(x, t)$ at $O(\sigma)$, given by

$$\frac{\partial h_1}{\partial t} - \mathcal{L}h_1 = q(x; X(\tau), P(\tau)) \quad (5.15)$$

where

$$q(x; X(\tau), P(\tau)) = \frac{\partial \bar{h}}{\partial x} \frac{dX}{d\tau} - \frac{\partial \bar{h}}{\partial \bar{p}} \frac{dP}{d\tau} \quad (5.16)$$

and \mathcal{L} is the same linear operator in (5.6), which is given by (5.7). The adjoint operator \mathcal{L}^* and its nullspace are given in Section 5.1. The solution to (5.15) depends on $\frac{dX}{d\tau}$ and $\frac{dP}{d\tau}$ on the right hand side of the equation. We have the freedom to choose $\frac{dX}{d\tau}$ and $\frac{dP}{d\tau}$. We choose $\frac{dX}{d\tau}$ and $\frac{dP}{d\tau}$ so that $-\mathcal{L}h_1 = q$ has a solution. This means that we choose $\frac{dX}{d\tau}$ and $\frac{dP}{d\tau}$ so that the pressure and position at leading order are still governed by (5.10a)-(5.10b) as in the original simplified ODE model. The corrections for X and P will be incorporated by the influences of $h_1(x, t)$.

To derive the boundary conditions for h_1 , we use the boundary condition of the exact PDE given by (5.2) and $\frac{\partial h}{\partial x}(\pm L) = 0$. Substituting $h = \bar{h} + \sigma h_1$ into (5.2) and (5.3), at $O(\sigma)$, we let $\frac{\partial h_1}{\partial x}(\pm L) = 0$ and thus have

$$\frac{\partial h_1}{\partial x}(\pm L) = 0 \quad (5.17)$$

$$\frac{\partial^3 h_1}{\partial x^3}(\pm L) = -\frac{J_{\pm}}{h_{\min}^3} \quad (5.18)$$

The PDE for h_1 is coupled with $P(\tau)$ and $X(\tau)$ through $\bar{h}(x - X(\tau), P(\tau))$ in (5.15). $P(\tau)$ and $X(\tau)$ given by the ODE system (5.10a)-(5.10b) are solved using forward Euler's method in τ . The PDE for h_1 , (5.15) is numerically solved using backward Euler time-stepping scheme in t . The outline of the numerical scheme used at a given time step is described below.

$$P^n = P^{n-1} + \sigma \Delta t C_P^{n-1}(J_+ - J_-) \quad (5.19a)$$

$$X^n = X^{n-1} + \sigma \Delta t C_X^{n-1}(J_+ + J_-) \quad (5.19b)$$

$$\frac{h_1^n - h_1^{n-1}}{\Delta t} - \mathcal{L}_{\delta}^n h_1^n = q(x, X^n, P^n) \quad (5.19c)$$

where \mathcal{L}_{δ}^n is \mathcal{L} discretized using a second order central finite difference method at $t = t^n$.

We determine the new position of the droplet by

$$x_1(t) = \underset{x}{\operatorname{argmax}}(\bar{h}(x - X(\tau), P(\tau)) + \sigma h_1(x, t)) \quad (5.20)$$

We calculate the new pressure of the droplet by

$$p_1(t) = \mathcal{P}(\bar{h}(x - X(\tau), P(\tau)) + \sigma h_1) \Big|_{x=x_1} \quad (5.21)$$

where \mathcal{P} is the pressure operator defined as in (5.13), i.e. $\mathcal{P}g = \Pi(g) - g_{xx}$.

To express $x_1(t)$ as a function of $X(\tau)$, we write $x_1(t) = X(\tau) + \delta X_1(t)$ for some $\delta \ll 1$. Since $x = x_1(t)$ is where $h(x, t) = \bar{h}(x - X(\tau), P(\tau)) + \sigma h_1(x, t)$ attains a maximum, we have

$$\frac{\partial h}{\partial x}(x_1(t), t) = \frac{\partial \bar{h}}{\partial x}(x_1(t) - X(\tau), P(\tau)) + \sigma \frac{\partial h_1}{\partial x}(x_1(t), t) = 0 \quad (5.22)$$

Substituting the expansion $x_1(t) = X(\tau) + \delta X_1(t)$ into (5.22), we have

$$\frac{\partial \bar{h}}{\partial x}(\delta X_1(t), P(\tau)) + \sigma \frac{\partial h_1}{\partial x}(X(\tau) + \delta X_1(t), t) = 0 \quad (5.23)$$

Writing out the Taylor expansion of (5.23) at $x = X(\tau)$ yields

$$\delta X_1(t) \frac{\partial^2 \bar{h}}{\partial x^2}(0, P(\tau)) + \sigma \frac{\partial h_1}{\partial x}(X(\tau), t) = 0 \quad (5.24)$$

This suggests $\delta = \sigma$ and

$$x_1(t) \sim \tilde{X}(t) = X(\tau) + \sigma X_1(t) \quad (5.25)$$

where

$$X_1(t) = -\frac{\frac{\partial h_1}{\partial x}(X(\tau), t)}{\frac{\partial^2 \bar{h}}{\partial x^2}(0, P(\tau))} \quad (5.26)$$

To express $p_1(t)$ as a function of $P(\tau)$, we first find the Taylor expansion of $\mathcal{P}(\bar{h}(x - X(\tau), P(\tau)) + \sigma h_1)$ at $h = \bar{h}$. To leading order,

$$\mathcal{P}\bar{h}(x - X(\tau), P(\tau)) = P(\tau)$$

so the pressure at leading order is $P(\tau)$. At next order, we obtain a linearization of $\mathcal{P}(\bar{h} + \sigma h_1)$ at \bar{h} . Hence, $p_1(t) = \tilde{P}(t) + O(\sigma^2)$ where $\tilde{P}(t)$ is given by

$$\tilde{P}(t) = P(\tau) + \sigma \mathcal{L}_0 h_1 \Big|_{x=X(\tau)} \quad (5.27)$$

for \mathcal{L}_0 defined as $\mathcal{L}_0 g = \Pi'(\bar{h})g - g_{xx}$.

We first solve (5.15) using the numerical scheme described above for a droplet in pure mass change mode with $J_+ = -J_- = -1$, $L = 3$. The full PDE for $h(x, t)$ is solved with initial condition $h(x, 0) = \bar{h}(x - X(0), P(0))$. Therefore, the initial condition of h_1 is given by $h_1(x, 0) \equiv 0$. In the case of pure mass change mode, $\frac{dx_1}{dt} = 0$ and $x_1(t) = X(0)$ for all time. Figure 5.5 shows the pressure calculated from the full PDE, the original ODE model and the refined model when the droplet is in a pure mass decrease mode with $x_1(t) = 0$. The pressure of the full PDE is calculated by (5.13). We observe that the refined pressure $p_1(t)$ calculated using h_1 and the new coupled ODE system agrees well with $p(t)$ calculated from the full PDE. This shows the improvement of $p_1(t)$ compared to the original ODE model. We also computed the pressure using \tilde{P} given by (5.27). The numerical simulations validate the analysis given by (5.27) and confirm $p_1(t)$ as an $O(\sigma)$ correction to $P(t)$. The numerical results suggest that keeping the first two terms of the Taylor expansion of $p_1(t)$ are sufficient to produce a good approximation of $p_1(t)$.

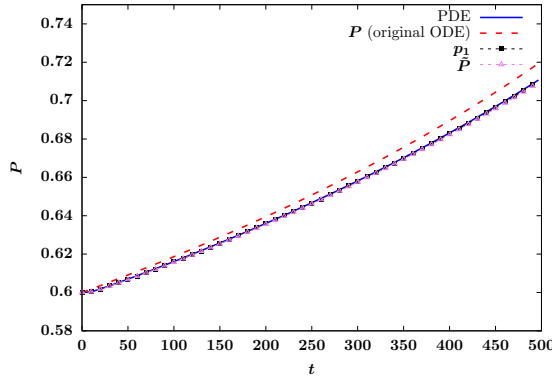


FIGURE 5.5: Pressure evolution a single droplet in a mass change mode, computed by the full lubrication PDE, the original ODE model, and the refined model. p_1 and \tilde{P} are both calculations from the refined model. p_1 is calculated using (5.21). \tilde{P} is calculated using (5.27). $P(0) = 0.6$, $J_+ = J_- = 1$, $\sigma = 10^{-4}$, $L = 3$.

Next, we solve (5.15) for a droplet in a pure translation mode with $J_+ = J_- =$

1, $L = 3$. Figure (5.6) (a) shows the pressure of the droplet computed from the full PDE, the original ODE model and the refined model. As mentioned in Section 5.1, when the droplet is in a translation mode on a finite domain, there is a slow decrease in pressure observed from the real PDE solution while the original ODE model predicts the pressure to be constant. We observe from Figure 5.6 (a) that the refined pressure $p_1(t)$ calculated using h_1 by (5.21) and \tilde{P} calculated using (5.27) both capture this feature of the real PDE solution. The pressure given by the refined model steadily decreases at approximately the same rate as the solution to the full PDE over time. The small difference between the refined model and the full PDE solution may be a consequence of some initial transients due to the truncation of homoclinic solution. Figure 5.6 (b) shows the position computed from the full PDE, the original ODE model and the refined model. The position $x_1(t)$ given by the new coupled system involving h_1 agrees well with the position calculated from the full PDE solution. Compared to the original ODE model, the refined model improves the accuracy of the position prediction. In addition, we also computed $\tilde{X} = X + \sigma X_1$, which is represented by the triangle-dotted curve in Figure 5.6 (b). This validates our previous analysis that $x_1 \sim \tilde{X}$ can be considered as an $O(\sigma)$ correction to the original ODE model.

5.3 Summary

In this chapter, we studied the dynamics of thin film evolution on homogeneous substrates in 1-D. In Section 5.1, we reviewed a simplified model first proposed by Glasner and Witelski, which predicts the pressure and position evolution of droplets subject to fluxes through a finite-dimensional ODE system. By testing the model on a single droplet, we showed that the accuracy of the simplified ODE model could be limited by the magnitude of imposed fluxes at the boundary. To improve the accuracy of the previous model, in Section 5.2, we proposed a refined linear PDE model by

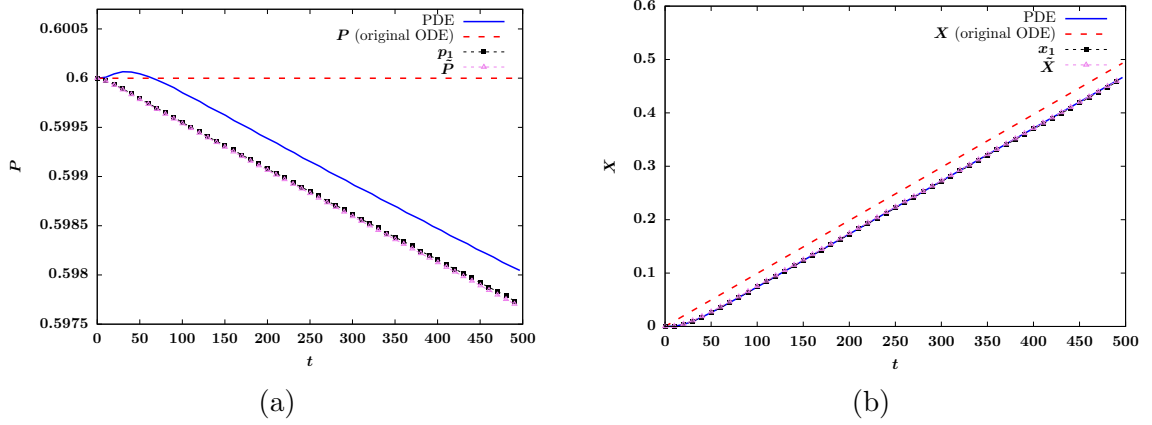


FIGURE 5.6: Pressure and position evolution of a single droplet in translation mode computed using the full lubrication PDE, the original ODE model and the refined model. Both x_1 and \tilde{X} are given by the refined model. x_1 is calculated using (5.20). \tilde{X} is calculated using (5.25)-(5.26). (a) pressure evolution (b) position evolution. $P(0) = 0.6$, $X(0) = 0.6$, $J_+ = J_- = 1$, $\sigma = 10^{-4}$, $L = 3$.

modifying the asymptotic expansion used in the previous model and solving for a higher-order approximation. The improvement in the pressure and position accuracy of the modified model was demonstrated through numerical simulations of droplets in both mass change and translation mode. It was shown through analysis that the refined model provides an $O(\sigma)$ correction to the original model for fluxes of $O(\sigma)$. A future direction of this work is to extend the refined model to multiple interacting droplets.

6

Conclusions

In this dissertation, we have studied both the steady-states and dynamics of thin liquid films using lubrication equations. In the first part of the dissertation, we focused on the steady-state thin liquid films. We reviewed the asymptotic analysis and bifurcation results previously derived for steady-states on homogeneous substrates. With increasing applications of chemically patterned substrates in manufacturing and technology industry, we then identified the need for a comprehensive understanding of wetting properties of chemically heterogeneous substrates. To study such problems, thin liquid films on a finite-length substrate with two regions of different wettability properties were considered. The wettability contrast across regions was modeled and incorporated into the lubrication approximations by a stepwise Hamaker constant in disjoining pressure. Asymptotic analysis of equilibrium solutions on such substrates was presented and discussed.

The second part of our work concerns the dynamics of thin films on homogeneous substrates. The high computational cost of solving the full lubrication equation to understand the long time evolution of thin films motivates the development of simplified models that capture the same phenomenon. A previous model developed for this

purpose was reviewed and examined. Specifically, through numerical simulations, the accuracy limitations of the model were identified. To improve the prediction of the previous model, we proposed a refined model that captures the single-droplet behavior with a higher accuracy. Both the derivation and validation of the model were demonstrated.

6.1 Steady-states of thin films in 1-D

In Chapter 4, we found that the bifurcation diagram of 1-D steady-state solutions on a stepwise-patterned substrate consists of two loops, namely an outer loop and an inner loop. We divided the outer loop equilibrium solutions into six categories, each of which corresponds to a segment in the bifurcation curve for p vs. h_{\max} . For equilibrium solutions on the outer loop, except when the film mass $m < \epsilon L$, the maximum film thickness always occurs at $x = 0$, where the Hamaker constant is smaller. Of the six different classes of solutions, there exist three kinds of stable droplet-type solutions, i.e. small-width droplets with width $w \leq s$, pinned droplets with $w \sim s$ and large-width droplets with $s \leq w \leq L$.

At leading order, the core of the small-width droplets resembles those of the homoclinic droplets formed on a homogeneous substrate with the same Hamaker constant, i.e. $A(x) \equiv A_1$ on $[0, s]$. The core of the large-width droplets resembles those of the homoclinic droplets formed on a homogeneous substrate with $A(x) \equiv A_2$ on $[0, L]$. In this regard, the pinned droplets are the only new steady-state droplets that arise from the wettability gradient and are characterized by properties that cannot be obtained from thin films on homogeneous substrates. The motion of the contact line of these droplets is restrained by the heterogeneity imposed at the interface $x = s$. Our asymptotic analysis in Section 4.2.4 shows that the pinned droplets exist only in the mass range $\frac{\sqrt{A_1}}{3\sqrt{3}}s^2 < m < \frac{\sqrt{A_2}}{3\sqrt{3}}s^2$. In this parameter

regime, the droplet mass and maximum thickness both grow linearly with pressure at a rate that is solely determined by s , regardless of A_2 at leading order. Compared to the previous studies on heterogeneous substrates where only small wettability contrast was considered, we examined the profiles of droplets formed in the limit of large wettability contrast. As the A_2 region becomes more hydrophobic, the pinned droplet becomes increasingly confined in the A_1 region with width $w \rightarrow s$ and $h(s) \rightarrow \epsilon$. This suggests that a stepwise patterned substrate with jump at $x = s$ could be effectively used to obtain droplets with width $w \sim s$. The width of the droplets obtained by depositing films on such substrates can be made more precise by increasing A_2 . The desired droplet height can be obtained by tuning the fluid mass according to $h_{\max} \sim \frac{3m}{2s}$. In the limit of large A_2 , the contact angle of this class of droplets is given by $\theta \sim \sqrt{-\frac{A_1}{3} + p^2 s^2} \sim \sqrt{-\frac{A_1}{3} + \frac{9m^2}{s^4}}$. Therefore, the same substrate could also be used to obtain droplets of certain desired contact angle by tuning A_1 and the film mass accordingly. The analysis in 1-D can be easily extended to axisymmetric solutions to yield similar results.

6.2 Dynamics of thin films in 1-D

In Chapter 5, we presented a refined model based on a previous model that predicts the pressure and position evolution of a single droplet on a finite 1-D domain. Compared to the previous model, the refined model consists of two new features. First, we modified the time scale used in the asymptotic expansion of the previous model, which changed the nature of the model from a finite-dimensional ODE system to a system of ODEs coupled with a linear PDE. Second, we sought for a higher-order solution that improves the overall prediction accuracy of the model in presence of increasing fluxes and larger initial perturbations. Numerical simulation results show that the refined model is particularly important for capturing the pressure evolution

of a translating droplet. For a droplet in translation mode, the change in droplet pressure can only be reflected through the higher-order term given by the refined model. Despite the fact that the new system requires numerically solving a linear PDE, the model still has a much lower computational cost compared to the full nonlinear lubrication equation, which involves an iterative algorithm at each time step. In addition, our analysis of the improved pressure and position formulation also provides an understanding of the error propagation of the previous model.

6.3 Future directions

While the equilibrium and flow of thin films have been extensively investigated in the past, the steady-states and dynamics of thin films on solid substrates remain a complicated nonlinear problem with many open questions. In this section, we discuss two primary future research topics that arise from our current work. First, thin films exist on two-dimensional surfaces in the real world. In this dissertation, we have mainly focused on one-dimensional and axisymmetric steady-state solutions. Many interesting phenomena and properties of the general non-axisymmetric steady-state thin films on two-dimensional surfaces remain unexplored. Second, it has been found that on one-dimensional chemically heterogeneous substrates, pinning is favored over coarsening in certain parameter regimes [14]. In Chapter 4 of this dissertation, we showed that the stepwise-patterned heterogeneity of the solid substrate introduces a branch of pinned droplets. As a consequence, the dynamics of thin film evolution on such heterogeneous substrates is modified and remains to be studied systematically.

6.3.1 *Thin films on two-dimensional surfaces*

Understanding of the wetting of micro/nano-structured surfaces is important for the operation of many biomedical microdevices. Both theories and experiments have been used to study the behavior of small volumes of liquid on chemically heteroge-

neous surfaces [38]. Using both experimental and simulation approaches, Kaspar et al. explored the shape of confined water droplets on rectangular micro/nano-arrayed structures with chessboard-like alternating hydrophilic and hydrophobic rectangular areas. By using an energy minimization approach, they presented the dependence of contact angle on the droplet volume for different chessboard sizes. However, similar analysis for such droplets on a rectangular domain from the perspective of lubrication equation has not been fully studied. It would be interesting if we could derive asymptotic predictions that reproduce the experimental and simulation results presented in previous studies [38].

Figure 6.1 (a) shows the profile an equilibrium droplet on a square chemically heterogeneous substrate $[0, L] \times [0, L]$ where $A(x, y)$ is given by

$$A(x, y) = \begin{cases} A_1, & \text{if } \max(|x - \frac{1}{2}L|, |y - \frac{1}{2}L|) \leq s \\ A_2, & \text{otherwise} \end{cases} \quad (6.1)$$

for $A_2 = 5$, $L = 5$, $s = \frac{1}{2}L$ and $\epsilon = 0.1$. The corresponding level sets of the equilibrium solution is shown in Figure 6.1 (b). From the contour plot, we observe that as $h(x, y)$ decreases and approaches the ultra-thin film region, the level set of the droplet is characterized by a shape intermediate between a circle and a square. This is due to the competing effect between the prescribed heterogeneity and the tendency of the fluid film to form a spherical cap. Considering non-axisymmetric films on two-dimensional surfaces allows for the studies of more diverse chemical patterning that better describes real-world applications and phenomena not captured by 1-D or axisymmetric models.

Another related research topic that has been considered is the stability and morphology of thin films on chemically heterogeneous substrates with alternating hydrophilic and hydrophobic stripes [1, 12, 21, 36, 42, 45, 63, 66]. Periodic striped surfaces have been used extensively in manufacturing and engineering applications.

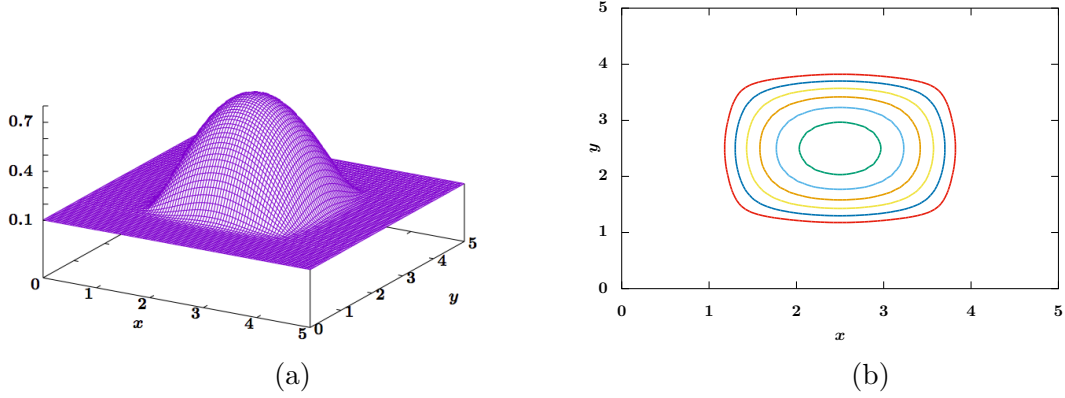


FIGURE 6.1: (a) Equilibrium of thin films on substrates with $A(x)$ described by (6.1). (b) Level sets of the equilibrium solution shown in (a).

Striped chemical patterning leads to more complex and interesting features such as formation of droplet arrays, confinement and droplet shape distortion [61]. In Chapter 4, we have mainly focused on the heterogeneous substrates consisting of only two regions of different wettability, subject to no-flux boundary conditions. As an extension of our current work, it would be interesting to consider disjoining pressure of the form $A(x)\Pi(h)$ where A_1 and A_2 are alternating periodically on $[0, L]$ and on rectangular domains to model periodically striped patterning. Periodic boundary conditions could also be considered to describe thin films on infinite domains.

Lubrication equations in two dimensions are numerically difficult to solve. The presence of nonlinearity and mixed derivatives makes studying the thin film problems on two-dimensional surfaces computationally challenging. The Alternating Direction Implicit (ADI) scheme has been used to solve nonlinear thin film equations and similar diffusion equations on two-dimensional domains [19, 24, 50, 60, 65, 72]. While ADI schemes for numerically solving parabolic equations have a long history, their use in higher-order problems is more recent and not all that well-studied [50]. Witelski and Bowen have developed an ADI scheme combined with Newton's method to solve nonlinear parabolic PDEs where approximate matrix factorization is used to

handle mixed derivative terms [72]. Specifically, at each Newton's iteration, they approximate the Jacobian matrix J by a matrix A which can be factored as $A = \mathcal{L}_x \mathcal{L}_y$ with $\|J - A\| = O(\Delta t^2)$ for some \mathcal{L}_x and \mathcal{L}_y that are linear operators in x and y direction respectively. The operator splitting simplifies the equation that needs to be solved at each Newton's iteration and allows for the use of banded matrix algorithms. The approximate Newton ADI scheme allows for an easy adaptation of the finite difference and Newton's method in one dimension to two dimensions and could be employed to study the thin film problems on two-dimensional domains described above. While the effectiveness of this ADI scheme has been demonstrated through simulations of thin film equations on rectangular domains, the error propagation introduced in approximating the Jacobian has not been fully understood. An efficient and reliable computational method is imperative for studying both the steady-states and dynamics of thin films on two-dimensional surfaces. It would be valuable to develop fast and effective computational methods, including but not limited to parallel computational approach, for large-scale thin film problems in two-dimensions [6, 43].

6.3.2 *Dynamics of thin films on heterogeneous substrates*

Thiele et al. studied the dynamics of thin film evolution on a chemically heterogeneous substrate with $A(x)$ described by small-amplitude sinusoidal modulation [66]. Specifically, they studied the dynamics of thin film evolution on such heterogeneous substrates and identified the parameter ranges where pinning is favored over coarsening. In their studies, they considered an infinite domain and varied the period of heterogeneity patterning. In Chapter 4, we focused on the steady-states of droplets on a finite stepwise-patterned heterogeneous substrate and analyzed the properties of the solution in the limit of large A_2 . In particular, we have shown that in the limit of large heterogeneity contrast $A_2 \rightarrow \infty$, the A_2 region has a confining effect on the fluid in the A_1 region and is capable of producing droplets that are pinned

at the interface. A question that arises from our studies on steady-state thin films is the effect of chemical heterogeneity on the evolution of thin films. In Chapter 5, we reviewed and proposed models that predict the dynamics of a single droplet on finite-length homogeneous substrates. An interesting extension of these current models would be a model that predicts the dynamics of droplets on finite-length chemically heterogeneous substrates.

Figure 6.2 (a) and (b) show the evolution of thin film profile and its corresponding energy on homogeneous substrates $A(x) \equiv A_1$, subject to no-flux boundary conditions. The initial condition of the thin film is given by $h(x, 0) = \frac{m}{L} \left[1 + \epsilon \cos \left(\frac{2\pi x}{L} \right) \right]$. The mass of the film is given by $m = 0.35$. As can be observed from the two figures, the thin film quickly breaks up to form two symmetric droplets centered at $x = 0$ and $x = L$. Figure 6.2 (c) shows the evolution of thin film with the same mass on a stepwise-patterned substrate for $L = 10$, $s = 5$, $A_1 = 1$, $A_2 = 2$, $\epsilon = 0.1$, subject to the same initial condition. Figure 6.2 (d) shows the corresponding energy evolution. In the heterogeneous case, while the film breaks up to form two asymmetric droplets at the two boundaries of the domain initially, as time increases, the droplet formed on the A_2 region loses mass while the droplet on the A_1 region gains mass, eventually leading to one single equilibrium droplet centered at $x = 0$. In this process, the energy of the thin film has an initial rapid decrease, followed by a relatively slow decrease for a long time until an equilibrium is approached, as shown in Figure 6.2 (d).

Figure 6.2 (e) shows the evolution of thin film profile on a similar stepwise-patterned substrate with $A_2 = 50$. We also initialize the thin film by the same initial condition. Figure 6.2 (f) shows the corresponding energy evolution. The evolution of the thin films goes through a similar dewetting process. However, the droplet formed at the right boundary has a smaller width compared to Figure 6.2 (c). Compared

to the case when $A_2 = 2$, the equilibrium is attained in a shorter time. The energy has a few more distinct decreasing stages compared to Figure 6.2 (d). This further illustrates the significant influence of heterogeneity on the overall dynamics of thin film evolution and leads to interesting questions on the analytical description of such phenomena.

While the dynamics of a single nanodroplet on wettability gradient surfaces has been previously investigated using lubrication approximation and microscopic analysis [13, 51], only sinusoidal wettability pattern was considered and the disjoining pressure used was different. Thorough analysis and description of droplet motion and pressure on heterogeneous substrate remain to be shown. It would be interesting to extend our work in Chapter 4 and Chapter 5 by developing an analogous ODE model that describes the position and pressure evolution of one or more droplets on a finite-length stepwise-patterned substrate. Quantifying the dependence of various parameters of the chemical heterogeneity such as s , A_2 , and L on the evolution of a single droplet is critical to understanding the dewetting and coarsening process of thin films on heterogeneous substrates.

To understand the scaling law and the long time statistics of a system of droplets, coarsening dynamical systems (CDS), which are dynamical systems reduced from the multi-scale nonlinear lubrication equations, have been used extensively [16, 25, 29]. For example, the simplified ODE model reviewed in Section 5.1 has been rescaled in the dilute limit to understand the coarsening law of a large system of droplets on homogeneous substrates [25]. However, the coarsening law and statistical properties of a large system of droplets on chemically heterogeneous substrates have not been well studied. Asgari and Moosavi have studied the coarsening dynamics of two interacting nanodroplets on chemically patterned substrates by using a modified version of boundary integral method [3]. The long time dynamics of a large array of droplets

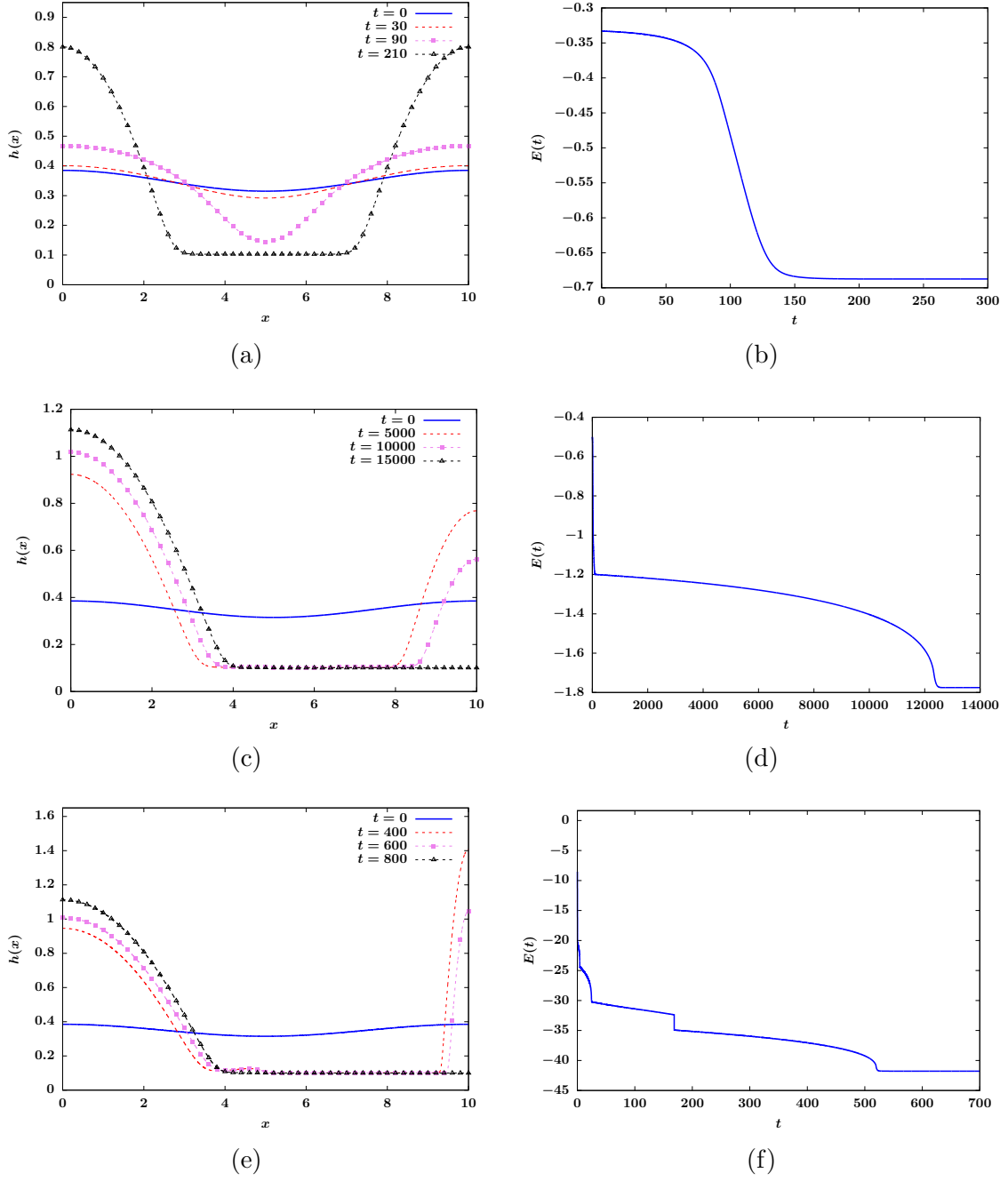


FIGURE 6.2: (a), (c) and (e) show the evolution of thin film profile over time on homogeneous and heterogeneous substrates for film mass $m = 0.35$, $\epsilon = 0.1$, $L = 10$. In (a), $A(x) \equiv A_1$. In (c) and (e), $s = 5$, $A_1 = 1$. In (c), $A_2 = 2$. In (d), $A_2 = 50$. (b), (d) and (f) show the evolution of energy corresponding to (a), (c) and (e).

on chemically patterned substrates modeled by lubrication theory has not been fully investigated. It is hoped that the analysis of the steady-state solutions presented in Chapter 4 could provide some insights into the development of a coarsening dynamical system that describes the coarsening on chemically heterogeneous substrates. In the future, it would be helpful to develop a reduced ODE model that is capable of predicting the underlying scaling laws of coarsening on chemically heterogeneous substrates.

Bibliography

- [1] V. S. Ajaev, E. Y. Gatapova, and O. A. Kabov. Stability and break-up of thin liquid films on patterned and structured surfaces. *Advances in Colloid and Interface Science*, 228:92–104, 2016.
- [2] M. Argentina, M. Clerc, R. Rojas, and E. Tirapegui. Coarsening dynamics of the one-dimensional cahn-hilliard model. *Physical Review E*, 71(4):046210, 2005.
- [3] M. Asgari and A. Moosavi. Coarsening dynamics of dewetting nanodroplets on chemically patterned substrates. *Physical Review E*, 86(1):016303, 2012.
- [4] P. W. Bates and J. P. Xun. Metastable patterns for the cahn-hilliard equation, part i. *Journal of Differential Equations*, 111(2):421–457, 1994.
- [5] J. Becker, G. Grün, R. Seemann, H. Mantz, K. Jacobs, K. R. Mecke, and R. Blossey. Complex dewetting scenarios captured by thin-film models. *Nature Materials*, 2(1):59, 2003.
- [6] P. Beltrame and U. Thiele. Time integration and steady-state continuation for 2d lubrication equations. *SIAM Journal on Applied Dynamical Systems*, 9(2):484–518, 2010.
- [7] A. L. Bertozzi, G. Grün, and T. P. Witelski. Dewetting films: bifurcations and concentrations. *Nonlinearity*, 14(6):1569, 2001.
- [8] B. Bhushan, Y. C. Jung, A. Niemietz, and K. Koch. Lotus-like biomimetic hierarchical structures developed by the self-assembly of tubular plant waxes. *Langmuir*, 25(3):1659–1666, 2009.
- [9] O. Bliznyuk. *Directional wetting on patterned surfaces*. PhD thesis, University of Twente, 7 2011.
- [10] L. B. Boinovich. Long-range surface forces and their role in the progress. *Russian Chemical Reviews*, 76(5):471, 2007.

- [11] B. J. Brasjen, H. Gu, and A. A. Darhuber. Dewetting of thin liquid films on chemically patterned substrates: front propagation along narrow lyophobic stripes and stripe arrays. *Microfluidics and Nanofluidics*, 14(3-4):669–682, 2013.
- [12] M. Brinkmann and R. Lipowsky. Wetting morphologies on substrates with striped surface domains. *Journal of Applied Physics*, 92(8):4296–4306, 2002.
- [13] F. Brochard. Motions of droplets on solid surfaces induced by chemical or thermal gradients. *Langmuir*, 5(2):432–438, 1989.
- [14] L. Bruschi, H. Kühne, U. Thiele, and M. Bär. Dewetting of thin films on heterogeneous substrates: Pinning versus coarsening. *Physical Review E*, 66(1):011602, 2002.
- [15] J. P. Burelbach, S. G. Bankoff, and S. H. Davis. Nonlinear stability of evaporating/condensing liquid films. *Journal of Fluid Mechanics*, 195:463–494, 1988.
- [16] C. K. Chapman. *Coarsening dynamical systems: dynamic scaling, universality and mean-field theories*. PhD thesis, University of Glasgow, 2012.
- [17] W. Ching-sung. *The Fundamentals of Aerosol Dynamics*. World Scientific, 1996.
- [18] J. Ching-Te Kao. *Mathematical modeling, simulation, and analysis of two problems in interfacial fluid dynamics*. PhD thesis, Northwestern University, 2008.
- [19] M. Ciesielski. Application of the alternating direction implicit method for numerical solution of the dual-phase lag equation. *Journal of Theoretical and Applied Mechanics*, 55(3):839–852, 2017.
- [20] A. A. Darhuber, S. M. Troian, S. M. Miller, and S. Wagner. Morphology of liquid microstructures on chemically patterned surfaces. *Journal of Applied Physics*, 87(11):7768–7775, 2000.
- [21] R. David and A. W. Neumann. Anisotropic drop shapes on chemically striped surfaces. *Colloids and Surfaces A: Physicochemical and Engineering Aspects*, 393:32–36, 2012.
- [22] P.-G. De Gennes. Wetting: statics and dynamics. *Reviews of Modern Physics*, 57(3):827, 1985.
- [23] H. Dong, W. W. Carr, and J. F. Morris. Visualization of drop-on-demand inkjet: Drop formation and deposition. *Review of Scientific Instruments*, 77(8):085101, 2006.

- [24] M. Eres, L. Schwartz, and R. Roy. Fingering phenomena for driven coating films. *Physics of Fluids*, 12(6):1278–1295, 2000.
- [25] K. Glasner and T. Witelski. Collision versus collapse of droplets in coarsening of dewetting thin films. *Physica D: Nonlinear Phenomena*, 209(1-4):80–104, 2005.
- [26] K. B. Glasner and T. P. Witelski. Coarsening dynamics of dewetting films. *Physical Review E*, 67(1):016302, 2003.
- [27] J. Gomba and G. Homsy. Analytical solutions for partially wetting two-dimensional droplets. *Langmuir*, 25(10):5684–5691, 2009.
- [28] A. G. González, J. A. Diez, and M. Sellier. Inertial and dimensional effects on the instability of a thin film. *Journal of Fluid Mechanics*, 787:449–473, 2016.
- [29] M. Gratton and T. Witelski. Coarsening of unstable thin films subject to gravity. *Physical Review E*, 77(1):016301, 2008.
- [30] R. Haberman. *Elementary Applied Partial Differential Equations*, volume 987. Prentice Hall Englewood Cliffs, NJ, 1983.
- [31] H. Hamaker. The london-van der waals attraction between spherical particles. *physica*, 4(10):1058–1072, 1937.
- [32] S. Herminghaus, K. Jacobs, K. Mecke, J. Bischof, A. Fery, M. Ibn-Elhaj, and S. Schlagowski. Spinodal dewetting in liquid crystal and liquid metal films. *Science*, 282(5390):916–919, 1998.
- [33] H. Hu, C. R. Weinberger, and Y. Sun. Model of meniscus shape and disjoining pressure of thin liquid films on nanostructured surfaces with electrostatic interactions. *The Journal of Physical Chemistry C*, 119(21):11777–11785, 2015.
- [34] J. C.-T. Kao, A. A. Golovin, and S. H. Davis. Rupture of thin films with resonant substrate patterning. *Journal of Colloid and Interface Science*, 303(2):532–545, 2006.
- [35] K. Kargupta, R. Konnur, and A. Sharma. Instability and pattern formation in thin liquid films on chemically heterogeneous substrates. *Langmuir*, 16(26):10243–10253, 2000.
- [36] K. Kargupta and A. Sharma. Templating of thin films induced by dewetting on patterned surfaces. *Physical Review Letters*, 86(20):4536, 2001.

- [37] K. Kargupta and A. Sharma. Morphological self-organization by dewetting in thin films on chemically patterned substrates. *The Journal of Chemical Physics*, 116(7):3042–3051, 2002.
- [38] O. Kašpar, H. Zhang, V. Tokárová, R. I. Boysen, G. R. Suñé, X. Borri, F. Perez-Murano, M. T. Hearn, and D. V. Nicolau. Confinement of water droplets on rectangular micro/nano-arrayed surfaces. *Lab on a Chip*, 16(13):2487–2493, 2016.
- [39] T. Kawase, T. Shimoda, C. Newsome, H. Sirringhaus, and R. H. Friend. Inkjet printing of polymer thin film transistors. *Thin Solid Films*, 438:279–287, 2003.
- [40] G. Kitavtsev, L. Recke, and B. Wagner. Centre manifold reduction approach for the lubrication equation. *Nonlinearity*, 24(8):2347, 2011.
- [41] L. Kondic and J. Diez. Instabilities in the flow of thin films on heterogeneous surfaces. *Physics of Fluids*, 16(9):3341–3360, 2004.
- [42] E. S. Kooij, H. Jansen, O. Bliznyuk, B. Poelsema, and H. J. Zandvliet. Directional wetting on chemically patterned substrates. *Colloids and Surfaces A: Physicochemical and Engineering Aspects*, 413:328–333, 2012.
- [43] M.-A. Y.-H. Lam, L. J. Cummings, and L. Kondic. Computing dynamics of thin films via large scale gpu-based simulations. *Journal of Computational Physics: X*, page 100001, 2019.
- [44] A. Leenaars. Particle removal from silicon substrates using surface tension forces. *Philips J Res*, 44:183–209, 1989.
- [45] P. Lenz and R. Lipowsky. Morphological transitions of wetting layers on structured surfaces. *Physical Review Letters*, 80(9):1920, 1998.
- [46] A. Leshansky and B. Rubinstein. Nonlinear rupture of thin liquid films on solid surfaces. *Physical Review E*, 71(4):040601, 2005.
- [47] R. C. Lo. Application of microfluidics in chemical engineering. *Chem Eng Process Technol*, 442:368–373, 2013.
- [48] V. A. Lubarda and K. A. Talke. Analysis of the equilibrium droplet shape based on an ellipsoidal droplet model. *Langmuir*, 27(17):10705–10713, 2011.

- [49] J. R. Mac Intyre, J. M. Gomba, and C. A. Perazzo. New analytical solutions for static two-dimensional droplets under the effects of long-and short-range molecular forces. *Journal of Engineering Mathematics*, 101(1):55–69, 2016.
- [50] M. R. Mata and A. L. Bertozzi. A numerical scheme for particle-laden thin film flow in 2-d. *Journal of Computational Physics*, 230(16):6334–6353, July 2007.
- [51] A. Moosavi and A. Mohammadi. Dynamics of nanodroplets on wettability gradient surfaces. *Journal of Physics: Condensed Matter*, 23(8):085004, 2011.
- [52] S. O’Brien and L. Schwartz. Theory and modeling of thin film flows. *Encyclopedia of Surface and Colloid Science*, pages 5283–5297, 2002.
- [53] A. Oron and S. G. Bankoff. Dewetting of a heated surface by an evaporating liquid film under conjoining/disjoining pressures. *Journal of Colloid and Interface Science*, 218(1):152–166, 1999.
- [54] A. Oron and S. G. Bankoff. Dynamics of a condensing liquid film under conjoining/disjoining pressures. *Physics of Fluids*, 13(5):1107–1117, 2001.
- [55] A. Oron, S. H. Davis, and S. G. Bankoff. Long-scale evolution of thin liquid films. *Reviews of Modern Physics*, 69(3):931, 1997.
- [56] A. A. Pahlavan, L. Cueto-Felgueroso, A. Hosoi, G. McKinley, and R. Juanes. Thin films in partial wetting: Stability, dewetting and coarsening. *Journal of Fluid Mechanics*, 845:642–681, 2018.
- [57] L. M. Pismen and Y. Pomeau. Mobility and interactions of weakly nonwetting droplets. *Physics of Fluids*, 16(7):2604–2612, 2004.
- [58] E. Ruckenstein and R. K. Jain. Spontaneous rupture of thin liquid films. *Journal of the Chemical Society, Faraday Transactions 2: Molecular and Chemical Physics*, 70:132–147, 1974.
- [59] M. Sakai, T. Yanagisawa, A. Nakajima, Y. Kameshima, and K. Okada. Effect of surface structure on the sustainability of an air layer on superhydrophobic coatings in a water- ethanol mixture. *Langmuir*, 25(1):13–16, 2008.
- [60] L. W. Schwartz, R. V. Roy, R. R. Eley, and S. Petrash. Dewetting patterns in a drying liquid film. *Journal of Colloid and Interface Science*, 234(2):363–374, 2001.

- [61] A. Sehgal, V. Ferreiro, J. F. Douglas, E. J. Amis, and A. Karim. Pattern-directed dewetting of ultrathin polymer films. *Langmuir*, 18(18):7041–7048, 2002.
- [62] A. Sharma and R. Khanna. Pattern formation in unstable thin liquid films under the influence of antagonistic short-and long-range forces. *The Journal of Chemical Physics*, 110(10):4929–4936, 1999.
- [63] A. Sharma, R. Konnur, and K. Kargupta. Thin liquid films on chemically heterogeneous substrates: self-organization, dynamics and patterns in systems displaying a secondary minimum. *Physica A: Statistical Mechanics and its Applications*, 318(1-2):262–278, 2003.
- [64] Y. Son, C. Kim, D. H. Yang, and D. J. Ahn. Spreading of an inkjet droplet on a solid surface with a controlled contact angle at low weber and reynolds numbers. *Langmuir*, 24(6):2900–2907, 2008.
- [65] N. Suzzi and G. Croce. Numerical simulation of thin film breakup on non-wettable surfaces. In *Journal of Physics: Conference Series*, volume 796, page 012038. IOP Publishing, 2017.
- [66] U. Thiele, L. Brusch, M. Bestehorn, and M. Bär. Modelling thin-film dewetting on structured substrates and templates: Bifurcation analysis and numerical simulations. *The European Physical Journal E*, 11(3):255–271, 2003.
- [67] J. Wang, Z. Zheng, H. Li, W. Huck, and H. Sirringhaus. Polymer field effect transistors fabricated by dewetting. *Synthetic Metals*, 146(3):287–290, 2004.
- [68] S. J. Watson, F. Otto, B. Y. Rubinstein, and S. H. Davis. Coarsening dynamics of the convective cahn-hilliard equation. *Physica D: Nonlinear Phenomena*, 178(3-4):127–148, 2003.
- [69] G. M. Whitesides. The origins and the future of microfluidics. *Nature*, 442(7101):368, 2006.
- [70] M. B. Williams and S. H. Davis. Nonlinear theory of film rupture. *Journal of Colloid and Interface Science*, 90(1):220–228, 1982.
- [71] T. P. Witelski and A. J. Bernoff. Dynamics of three-dimensional thin film rupture. *Physica D: Nonlinear Phenomena*, 147(1-2):155–176, 2000.
- [72] T. P. Witelski and M. Bowen. Adi schemes for higher-order nonlinear diffusion equations. *Applied Numerical Mathematics*, 45(2-3):331–351, May 2003.

- [73] Y. Yuan and T. R. Lee. Contact angle and wetting properties. In *Surface Science Techniques*, pages 3–34. Springer, 2013.
- [74] Q. Zhang and R. H. Austin. Applications of microfluidics in stem cell biology. *BioNanoScience*, 2(4):277–286, 2012.
- [75] X. Zhao, M. J. Blunt, and J. Yao. Pore-scale modeling: Effects of wettability on waterflood oil recovery. *Journal of Petroleum Science and Engineering*, 71(3-4):169–178, 2010.
- [76] M. Zope, K. Kargupta, and A. Sharma. Self-organized structures in thin liquid films on chemically heterogeneous substrates: Effect of antagonistic short and long range interactions. *The Journal of Chemical Physics*, 114(16):7211–7221, 2001.

Biography

Weifan Liu obtained her Bachelor's Degree in Mathematical Science from Worcester Polytechnic Institute in May, 2014 and her Ph.D in Mathematics from Duke University in May, 2019. She will begin as a Philip T. Church Postdoctoral Fellow at Syracuse University in Fall 2019.